



Montanuniversität Leoben - University of Leoben

Department Metallurgie - Department of Metallurgy

Nichteisenmetallurgie - Nonferrous Metallurgy



New concepts for understanding the effect of natural pre-aging on the artificial aging of Al-Mg-Si alloys

A dissertation presented by
Dipl.-Ing. Stefan Pogatscher



Examiner

Univ.-Prof. Dipl.-Ing. Dr. mont. Helmut Antrekowitsch

Co-Examiner

Univ.-Prof. Dipl.-Ing. Dr. mont. Peter J. Uggowitzer

Leoben, May 12

AFFIDAVIT

I declare in lieu of oath, that I wrote this thesis and performed the associated research myself, using only literature cited in this volume.

Stefan Pogatscher

Leoben, May 2012

ACKNOWLEDGEMENTS

First of all, I would like to thank Prof. Helmut Antrekowitsch for giving me the opportunity to carry out this thesis project at the Chair of Nonferrous Metallurgy. He has always guided me to find and pursue my own way. I particularly appreciate his confidence in my work and the freedom he gives me in accomplishing it.

Special thanks go to Prof. Peter J. Uggowitzer, who aroused my interest in vacancies, which was a real booster for my work. I strongly benefited from his fascination in science and his motivating, inspiring and supportive manner. I wish to express my sincere thanks for his great commitment as a co-referee of this thesis.

I would also like to thank the people at AMAG Rolling, especially Thomas Ebner, for the fruitful discussions and helping me with numerous industrial related issues.

Moreover, I would like to thank Helmut Kaufman, Anton Eberle, Carsten Melzer and Peter Schulz from AMAG for providing technical and financial support and for giving me the opportunity to publish my results.

Alla Sologubenko and Harald Leitner are sincerely thanked for their scientific support. I learned a lot from our discussions on transmission electron microscopy and atom probe tomography.

I would like to thank the entire staff at the Chair of Nonferrous Metallurgy - academic, technical and administrative - for making it an outstanding place to work. Thank you of course for all of your help and assistance.

I am deeply grateful to my family. Without them I would not be where I am today. Finally, I would like to thank my fiancée Ines for all her support, patience and love, and for giving me the strength to face the bad days and to appreciate the good ones.

Leoben, May 2012

Stefan Pogatscher

New concepts for understanding the effect of natural pre-aging on the artificial aging of Al-Mg-Si alloys

Al-Mg-Si alloys are the most frequently used group of age hardenable aluminum alloys. The adverse effect of natural pre-aging on the artificial aging, a problem of significant academic as well as industrial interest, has not been fully resolved since it was discovered in 1939. In this thesis a new concept for understanding this effect is presented.

Microstructural observations and an analysis of precipitation and dissolution kinetics revealed a dependence on the artificial aging temperature for the effect of natural pre-aging. This was explained by introducing the “vacancy-prison mechanism.” The model assumes that Mg,Si co-clusters, formed during natural pre-aging, reduce the mobility of quenched-in vacancies during artificial aging. The temperature dependent stability of these clusters induces the adverse effect of natural pre-aging at industrial common artificial aging temperatures but enhances artificial aging at high temperatures.

A comparative approach of atom probe tomography and transmission electron microscopy revealed that the important β'' phase contains Al and shows a Mg/Si ratio higher than expected from the previously reported Mg_5Si_6 stoichiometry in the alloy AA6061. Its size distribution was observed to strongly depend on the thermal history and its genesis was successfully explained by the “vacancy-prison mechanism.”

The nucleation of the β'' phase was studied via a multi-method approach using atom probe tomography, transmission electron microscopy, electrical resistivity and hardness measurements, and differential scanning calorimetry. It was shown that quenched-in vacancies are of particular importance for the nucleation of β'' , an important reason for the adverse effect of natural pre-aging.

The influence of the alloy composition was addressed by investigating the dissolution kinetics of Mg,Si co-clusters in different alloys. Theoretical considerations concerning the annihilation of quenched-in vacancies during artificial aging allowed extending the “vacancy-prison mechanism” to the whole group of Al-Mg-Si alloys. Moreover, it was shown that the dependence of precipitation kinetics on the solute super-saturation is a function of the thermal history in Al-Mg-Si alloys. This is an exception from common diffusion controlled precipitation kinetics, but can be well explained applying the “vacancy-prison mechanism.”

The presented new concept for understanding the effect of natural pre-aging on the artificial aging of Al-Mg-Si alloys describes the observed phenomenon quite well in a wide temperature and compositional range. It will significantly contribute to many industrial issues. Based on the fundamental results, a modified industrial quenching procedure was already presented as a new heat treatment strategy to avoid the negative effect of natural pre-aging without requiring an

additional pre-aging step. Furthermore, it was shown that the effect of natural pre-aging can be influenced by trace additions of “vacancy active” elements, making a 70 year old problem controllable.

Neue Konzepte zum Verständnis der Wirkung einer Kaltaushärtung auf die Warmaushärtung von Al-Mg-Si Legierungen

Al-Mg-Si-Legierungen sind die am häufigsten eingesetzte Gruppe aushärtbarer Aluminiumlegierungen. Dass sich eine Kaltaushärtung auf die darauffolgende Warmaushärtung negativ auswirken kann, wurde bereits im Jahre 1939 entdeckt. Eine zufriedenstellende Erklärung dieser wissenschaftlich, aber vor allem auch für die Industrie bedeutenden Fragestellung, konnte bis heute jedoch nicht erbracht werden. In dieser Arbeit wird ein neues Konzept zum metallphysikalischen Verständnis dieses Effekts vorgestellt.

Durch mikrostrukturelle Beobachtungen und eine kinetische Analyse von Ausscheidungsphänomenen konnte erstmals eine Temperaturabhängigkeit des Effektes einer Kaltaushärtung auf die Warmaushärtung festgestellt werden. Der daraus abgeleitete „Leerstellen-Gefängnis-Mechanismus“ geht davon aus, dass Mg₂Si Co-Cluster, welche durch eine Kaltaushärtung entstehen, die Mobilität von Leerstellen während einer darauffolgenden Warmaushärtung stark einschränken können. Die Stabilität dieser Cluster im industriell angewandten Temperaturbereich führt zum beobachteten negativen Effekt der Kaltaushärtung auf die Warmaushärtung. Höhere Warmaushärtungstemperaturen bewirken jedoch eine Auflösung von Mg₂Si Co-Clustern und damit eine Beschleunigung der Warmaushärtung.

Durch eine detaillierte Untersuchung des Ausscheidungsgefüges mittels Atomsondentomographie und Transmissionselektronenmikroskopie konnte nachgewiesen werden, dass die bei der Warmaushärtung von Al-Mg-Si-Legierungen wichtige β'' -Phase Al enthält. Weiters zeigt ein ungewöhnlich hohes Mg/Si-Verhältnis, dass die β'' -Phase in der Legierung AA6061 nicht der bisher bekannten Mg₅Si₆ Stöchiometrie entspricht. Die Größenverteilung der β'' -Phase hängt in hohem Maße von der thermischen Vorgeschichte ab, wobei sich dieser Effekt einfach mit dem „Leerstellen Gefängnis Mechanismus“ erklären lässt. Zur Untersuchung der Keimbildung von β'' kam eine Kombination aus Atomsondentomographie, Transmissionselektronenmikroskopie, Messung des elektrischen Widerstandes und der Härte sowie dynamische Wärmestromdifferenzkalorimetrie zum Einsatz. Die Ergebnisse belegen, dass Leerstellen eine besondere Bedeutung in der Unterstützung der Keimbildung von β'' einnehmen, wobei dies auch ein wesentlicher Grund für die Wirkung der Kaltaushärtung ist.

Der Legierungseinfluss wurde mittels einer Messung der Auflösungskinetik von Mg₂Si-Co-Clustern in verschiedenen Legierungssystemen untersucht. Gekoppelt mit theoretischen Überlegungen zur Annihilation von Ungleichgewichtsleerstellen während der Warmaushärtung gelang eine Verallgemeinerung des Leerstellen-Gefängnis-Modells auf die gesamte Gruppe der Al-Mg-Si-Legierungen. Weiters konnte gezeigt werden, dass die Abhängigkeit der

Warmaushärtungskinetik von der thermodynamischen Übersättigung eine Funktion der thermischen Vorgeschichte ist, wobei dies eine Abweichung von den gängigen Theorien zur Beschreibung diffusionskontrollierter Ausscheidungsreaktionen darstellt, jedoch bestens mit dem „Leerstellen-Gefängnis-Mechanismus“ in Einklang steht.

Das vorgestellte Modell zum Verständnis der Wirkung einer Kaltaushärtung auf die Warmaushärtung von Al-Mg-Si-Legierungen beschreibt die beobachteten Phänomene in einem weiten Temperatur- und Zusammensetzungsbereich und ist in der Lage, Antworten auf viele industrielle Fragestellungen zu liefern. Basierend auf den Erkenntnissen konnte daher eine modifizierte Abschreckung als neue industrielle Wärmebehandlungsstrategie zur Vermeidung des negativen Effekts der Kaltaushärtung, welche gänzlich ohne zusätzlichen Wärmebehandlungsschritt auskommt, vorgestellt werden. Darüber hinaus wurde gezeigt, dass die Wirkung der Kaltaushärtung durch die Zugabe von leerstellenaktiven Spurenelementen beinahe nach Belieben gesteuert werden kann, womit ein 70 Jahre lang unverstandener Effekt nun beherrschbar wird.

CONTENTS

1 INTRODUCTION	1
1.1 History of Al-Mg-Si alloys	2
1.2 Technological aspects of room temperature storage	4
1.2.1 Al-Mg-Si sheets	4
1.2.2 Al-Mg-Si plates	6
1.2.3 Other Al-Mg-Si wrought products	8
1.2.4 Cast products based on the Al-Mg-Si system	8
1.3 Physical aspects of room temperature storage	9
1.3.1 Natural aging	9
1.3.2 Artificial aging	10
1.4 Approach	13
2 TEMPERATUR DEPENDENCE OF AGING	17
2.1 Introduction	18
2.2 Experimental methods	20
2.2 Experimental results	22
2.3.1 Age hardening behavior	22
2.3.1.1 Natural aging	22
2.3.1.2 Artificial aging	22
2.3.2 Microstructural evolution	25
2.3.2.1 Electrical Resistivity	25
2.3.2.2 Atom probe tomography	26
2.4 Hardness data analysis	27
2.4.1 Temperature dependence of co-cluster dissolution	27
2.4.2 Temperature dependence of precipitation kinetics	29
2.5 Discussion	31
2.5.1 Role of vacancies	33
2.5.2 Mechanisms controlling artificial aging in dependence on heat treatment procedure and aging temperature	36
2.5.2.1 Artificial aging at common temperatures	36
2.5.2.2 Artificial aging at high temperatures	36
2.6 Conclusions	38

3 THE β'' PHASE	41
3.1 Introduction	42
3.2 Experimental methods	43
3.3 Results and discussion	44
3.3.1 Atom probe tomography	44
3.3.2 Transmission electron microscopy	47
3.4 Conclusions	51
4 NUCLEATION AND ITS USE	54
4.1 Introduction	55
4.2 Experimental methods	57
4.3 Results	59
4.3.1 Hardness evolution	59
4.3.2 Electrical resistivity evolution	61
4.3.3 Microstructure evolution	62
4.3.4 Differential scanning calorimetry	66
4.4 Discussion	68
4.4.1 Interrupted quenching in region 1	68
4.4.2 Interrupted quenching in region 2	72
4.5 Conclusions	73
5 COMPOSITION I	76
5.1 Introduction	77
5.2 Experimental methods	79
5.3 Experimental results	80
5.3.1 Natural aging	80
5.3.2 Artificial aging	81
5.3.3 Co-cluster dissolution natural aging	83
5.4 Discussion	86
5.4.1 AA6060	88
5.4.2 AA6061	88
5.5 Conclusions	89

6 COMPOSITION II	92
6.1 Introduction	93
6.2 Experimental methods	95
6.3 Results	96
6.3.1 Computational evaluation of the chemical composition	96
6.3.2 Artificial aging	100
6.4 Yield strength analysis	101
6.5 Discussion	106
6.6 Conclusions	108
7 SUMMARY & OUTLOOK	111
7.1 Summary	112
7.2 Outlook	114
APPENDIX	118

1 INTRODUCTION

1.1 History of Al-Mg-Si alloys

Since Charles Martin Hall und Paul Héroult invented fused-salt electrolysis in 1886 using an electrolyte of cryolite (Na_3AlF_6) and dissolved Al_2O_3 , and Carl Josef Bayer succeeded in producing pure aluminum oxide (Al_2O_3) from bauxite (1887-1892), aluminum became the most important non-ferrous metal in the 20th century [1-3]. The production of aluminum is still increasing strongly and nearly reached the 50 million ton per year limit in 2010. This trend is illustrated in figure 1.1, showing the annual world production of aluminum from bauxite (primary) and scrap (secondary) in million tons per year from 1900 to 2010.

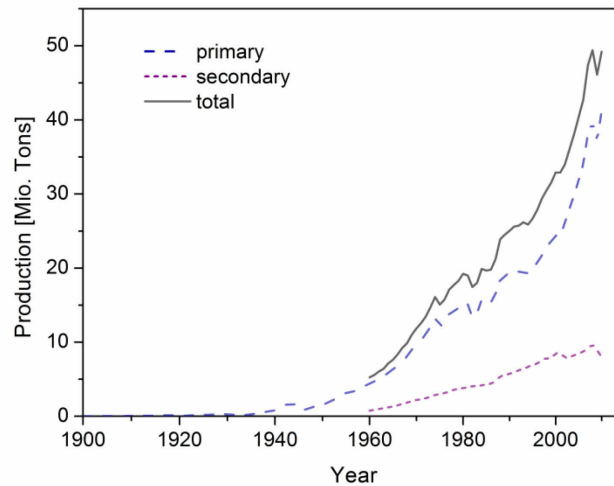


Figure 1.1: Annual world production of aluminum in m tons [4-8]

The triumphal procession of aluminum alloys for structural applications was initiated by Alfred Wilm, who wrote in 1911: “*Meine Untersuchungen über Aluminiumlegierungen, welche ich seit dem Jahre 1903 an der Zentralstelle für wiss.-techn. Untersuchungen Neubabelberg anstelle, haben ergeben, daß schon ein geringer Gehalt an Magnesium dem Aluminium zugesetzt, dasselbe durch einen Glühprozess härter macht.*” (My studies of aluminum alloys at the central office for scientific-technical investigations in Neubabelberg, which I have been conducting since 1903, have shown that even a small amount of magnesium added to aluminum enables hardening by a thermal treatment.) [9]. This technological highly important phenomenon, accidentally discovered in an Al-Cu-Mg alloy for the first time by Wilm, quickly revived much industrial and academic interest and in the year 1925, Robert S. Archer and Zay Jeffries presented a new type of “High-strength Aluminum Alloys;” the Al-Mg-Si alloys [10]. In those days when the Al-Mg-Si alloys were born, it was not even clear how age hardening works and it took another 13 years till Guinier [11] and Preston [12] could resolve the phenomenon in an Al-Cu alloy. They came up with the first experimental observations of the formation of small

precipitates in the aluminum matrix and claimed them to be responsible for the observed strengthening effect.

The inventors of the Al-Mg-Si alloys already recommended artificial aging (baking the alloy at about 150 to 180 °C after quenching from ~500 °C) as a preferential heat treatment [10]. As the development of Al-Mg-Si alloys proceeded, in 1939 a systematic study of the heat treatment strategy and alloy composition by Brenner and Kostron [13] revealed a significant influence of storing the alloy at room temperature (RT) after quenching on the success of subsequent artificial aging. They showed that room temperature storage after quenching induces a strong adverse effect on kinetics and the achievable strength in rich Al-Mg-Si alloys (figure 1.2) but can even have a positive effect on lean Al-Mg-Si alloys.

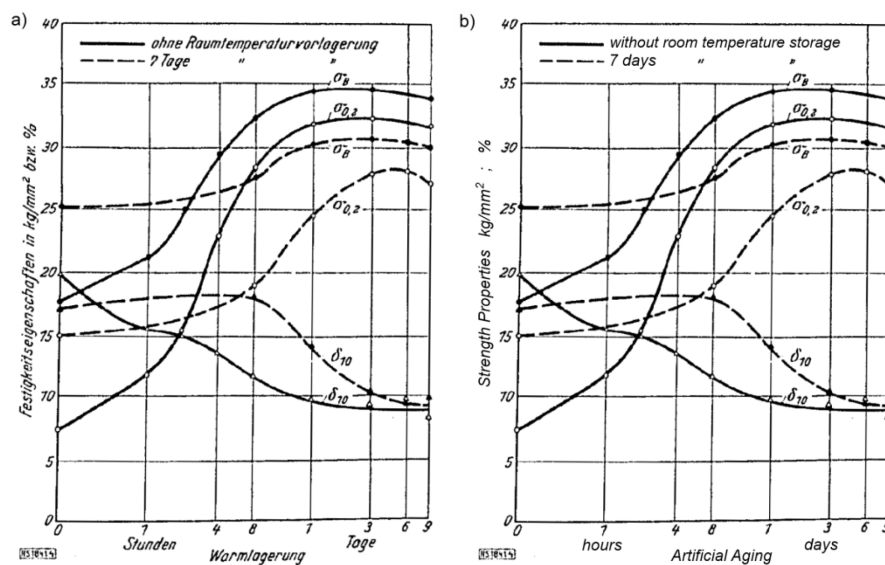


Figure 1.2: Adverse effect of storing a rich Al-Mg-Si alloy at room temperature before artificial aging is performed. (a) original drawing [10] (b) labeling translated

Although it was impossible at that time to uncover the full mechanisms - experimental methods to observe processes happening on the atomic length scale were not available at that time - their paper already contains an extraordinary hint contributed by the Austrian physicist E. Schmidt: *“Es könnte sein, daß während der Raumtemperlagerung die Magnesium- oder Siliziumatome (oder auch beide) in Zustände kommen, in denen diese Diffusion erschwert ist”* (It could be that during storage at room temperature the magnesium and silicon atoms (or both) reach a state where the diffusion is more difficult.) [13]. This statement is even more outstanding considering the fact that the principle which diffusion in metals is based on (the vacancy mechanism) was not published until several years later by Kirkendall [14].

In the last century many researchers contributed to aging in Al-Mg-Si alloys, but even the precipitation sequence is rather controversial discussed, and such important questions as the nature of the major hardening phase formed during artificial aging [15-17] or the processes occurring during natural aging [18,19] are still open. Therefore it is not surprising that the influence of room temperature storage on artificial aging discovered in 1939 [13] has also not been fully resolved and the first sentence of the introduction of Brenner's and Kostron's paper seems to be still valid in parts: *“Trotzdem die Entdeckung der ersten vergütbaren Aluminiumlegierungen nun schon Jahrzehnte zurückliegt, ist unsere Kenntnis über den Mechanismus, auf dem die Verfügbarkeit beruht doch recht lückenhaft.”* (In spite of the fact that the discovery of the first age hardenable aluminum alloys was decades ago already, our knowledge of the mechanism on which aging is based is far from complete.)

1.2 Technological aspects of room temperature storage

Nowadays the Al-Mg-Si alloys are the most important group of age hardenable aluminum alloys commercially [1,19]. They are widely used in cast, wrought and extruded form for construction, automotive engineering, shipbuilding, and the aircraft industry [2,20]. A high ratio of strength to density, very good corrosion resistance, excellent surface properties and weldability together with relatively low price are the reasons for their success [21]. A further advantage in terms of sustainability is the possibility to use a high fraction of secondary raw material for their production.

High strength Al-Mg-Si alloys rich in Mg and Si represent the lion's share of all commercially produced Al-Mg-Si alloys and exhibit a strong adverse influence of room temperature storage longer than a few minutes after quenching on the artificial aging procedure. Such room temperature storage is not avoidable in most industrial cases for logistical or technological reasons [22-26]. It extends the duration of the artificial aging procedure up to a factor of 10 and reduces the energy efficiency, production capacity, and profitability of the Al-Mg-Si alloys processing accordingly. Furthermore, the achievable strength is significantly reduced [2]. In the following section, the impact of the negative effect on the processing of various products based on the Al-Mg-Si system is discussed. A special focus is set on sheets and plates, which are products delivered by AMAG Rolling, the industrial partner of this thesis.

1.2.1 Al-Mg-Si sheets

The increasing use of Al-Mg-Si alloys (e.g. AA6016) as hardenable auto body sheets has revived the interest in investigating the negative influence of room temperature storage in the last few years. 45,000 tons of Al-Mg-Si sheets are produced annually, resulting in a turnover of

approximately 150 m € worldwide [27]. Figure 1.3 illustrates the processing of Al-Mg-Si alloys for automotive outer panel applications [28]. The critical steps in the process chain concerning the effect of room temperature storage are framed in figure 1.3 and include pre-aging and the supply of the material to the customer, where the sheets are formed and finally aged during a paint bake process.

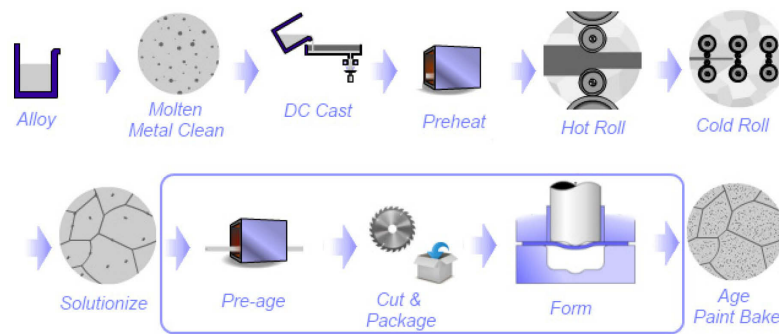


Figure 1.3: Processing of Al-Mg-Si alloys for auto body sheet purposes [28]

For a material which has undergone room temperature storage after quenching, a typical paint bake cycle of 30 min at 175 °C is much too short to reach so-called “T6 strength” (peak aged condition), which would require 10 to 20 h [2]. To optimize the artificial aging behavior during paint baking, various pre-aging treatments, mostly additional long-term heat treatments performed immediately after quenching for several hours at temperatures around 100 °C were investigated [29-32] and patented (e.g. [33-39]). Figure 1.4 schematically shows the effect of such a pre-aging treatment on artificial aging after room temperature storage.

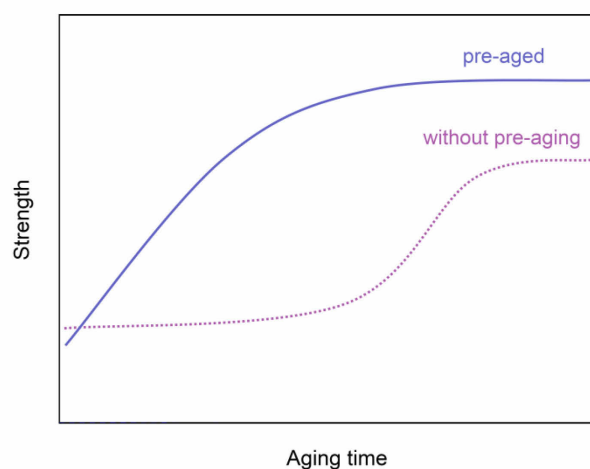


Figure 1.4: Schematic drawing of the effect of pre-aging on artificial aging after room temperature storage

Unfortunately, this further process step inevitably increases the effort in production, and is additionally not able to preserve the desired formability, as it is favored over a long period of room temperature storage. Moreover, it is often not possible to achieve kinetics as fast as reached by aging directly after quenching, which would be readily fast enough to guarantee T6 strength after a paint bake cycle. To conclude, room temperature storage cannot be avoided for logistical and technological reasons in the production of Al-Mg-Si sheets for automotive outer panel applications at present. Therefore significant effort is necessary to minimize the adverse effect on artificial aging while keeping a good formability.

1.2.2 Al-Mg-Si plates

Al-Mg-Si plates are mainly used as semi-finished products for milling operations in the engineering and transportation industry as well as for many applications in electronics and the semiconductor industry. Frequently used alloys are AA6061 and AA6082. The annual world production of plates is around 120,000 tons, with a turnover of 500 m € per year [27]. Due to the fact that the majority of experimental investigations of the present study are based on such material, the processing of Al-Mg-Si plates is discussed in a bit more detail below. Figure 1.5 illustrates the process chain schematically [28] starting with the production of Al-Mg-Si ingots in the foundry, which are subsequently prepared for hot rolling by milling the lower and upper surfaces. The pre-heating process for hot rolling includes a homogenization treatment of the cast microstructure which is carried out at 540 to 580 ° C for 14 to 18 h. After hot rolling the plates were cut and cooled to room temperature. The solution heat treatment is commonly performed at 540 to 580 ° C for a period of 15 to 40 min to create a homogeneous solid solution. To conserve a high super saturation of substitutional elements prone to precipitation hardening, the plates are quenched to room temperature using water spraying immediately after the solution annealing. Any delay in the quenching procedure affects the strength and corrosion resistance, which is why a quick transfer from the furnace to the quenching facility is necessary. In order to reduce internal stresses induced by quenching due to geometrically non-uniform cooling conditions, a plastic deformation of 1.5 to 3 % is applied to the plates by stretching. Because of the adverse effect of RT storage the artificial aging regime often requires more than 24 h at 160 to 180 °C to reach T6 strength. Finally, the Al-Mg-Si plates were cut to the appointed dimensions, labeled and packed [1,2].

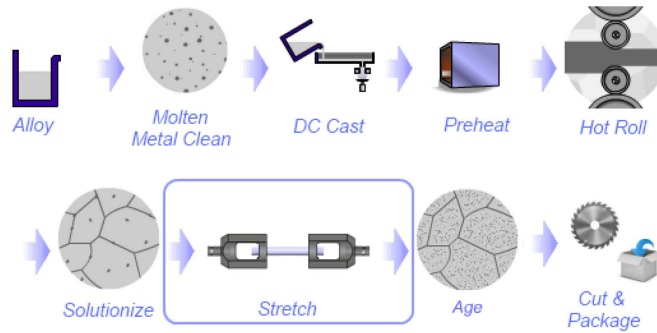


Figure 1.5: Processing of Al-Mg-Si alloy plates [28]

The majority of Al-Mg-Si plates are delivered in so-called “T651 condition” (solution heat treated, stretched and artificially aged). Hence, the in-house processing covers quenching and artificial aging. The critical period concerning the effect of room temperature storage is framed in figure 1.5. One would assume that the controllability of the room temperature storage between quenching and artificial aging might be better for Al-Mg-Si plates than for sheets where quenching is done by the producer of semi-finished products and artificial aging is performed at the customer of these products. Nevertheless, there are some issues that complicate an easy handling of the adverse effect of RT storage in the production of plates. The fast appearance of the effect (<30 min [24]) causes significant logistical problems. What's more, there are some physical and technological constraints. After quenching to room temperature thick plates cannot be heated to artificial aging temperature as quickly as necessary because of finite values of the heat transfer coefficient and the thermal conductivity of aluminum. Technologically, the production of plates often includes a stretching process between quenching and artificial aging to guarantee a stress-relieved material for cutting operations performed at the customer. This makes a certain period of room temperature storage unavoidable. Accordingly, the required duration of artificial aging to reach T6 strength is quite long for the state of the art process route. Although various pre-aging treatments optimizing the artificial aging behavior are available for Al-Mg-Si sheets, nothing similar is known or applied for plates. A reason for this might be that thick plates are difficult to reheat fast enough immediately after quenching to room temperature. Furthermore, the effort of such additional process step reduces the commercial benefit generated by a shorter duration of the artificial aging procedure. Hence, a simple method avoiding the negative effect of room temperature storage in the production of Al-Mg-Si plates would be highly beneficial to the industry in terms of improved energy efficiency, production capacity, profitability and achievable strength and would therefore facilitate a more sustainable production in general.

1.2.3 Other Al-Mg-Si wrought products

Wrought Al-Mg-Si products such as extrusions and forging are not in focus of interest of this work, because those products are not produced by AMAG. Nevertheless, extrusions and forging are commercially important, often used in artificial aged condition, and the influence of RT storage between quenching and artificial aging is of significant interest as well.

Extrusion is the most economical forming process for aluminum and the majority of profiles for construction purposes are made from age hardenable alloys. In particular Al-Mg-Si alloys are used because of their superior extrudability compared to other groups of age hardenable aluminum alloys. Nowadays the heat treatment is commonly integrated in the extrusion process and quenching is performed directly after forming (so-called “T5 condition”). The influence of a subsequent RT storage depends on the individual processing operations and the type of Al-Mg-Si alloy. AA6060 is frequently used for the extrusion of complex profiles exhibiting medium strength and the only highly important lean Al-Mg-Si alloy. As an exception, intermediate room temperature storage induces no adverse influence on artificial aging kinetics and exhibits a positive effect on the T6-strength in AA6060. Consequently, intermediate room temperature storage after quenching is preferential. For applications requiring a higher strength, rich Al-Mg-Si alloys (e.g. AA6082) are used. As stretching is often performed after quenching, the adverse effect of room temperature storage appears similar to the production of plates in these alloys, although the handling might be easier in case of small parts.

Forged aluminum alloys are used in the aerospace and automotive industries as well as many other areas where a high degree of tolerance against failure must be ensured. Especially the rich Al-Mg-Si alloys (e.g. AA6082) are easy to forge and have been established as standard alloys for automotive applications, shipbuilding and mechanical engineering. As most heat treated forgings are plastically deformed within in the last forging step for 1 to 3 % after quenching to eliminate distortion and residual stresses, the adverse effect of room temperature storage appears similar to the production of plates, although the handling might be easier in case of small forgings.

1.2.4 Cast products based on the Al-Mg-Si system

Al-Si-Mg cast alloys are commonly used for automotive components such as wheels and cylinder heads [2,40,41]. These alloys contain a significantly higher amount of Si (5 to 10 %) compared to wrought Al-Mg-Si alloys (< 1.5% Si) and Mg additions of 0.3 to 0.5 % [1,2,18]. Nonetheless, the precipitation sequence is believed to be comparable to that of Al-Mg-Si wrought alloys [2]. A typical T6 heat treatment is performed as follows: solution treatment at 525 to 540 °C for 6 to 18 h, quenching in water at ≤ 70 °C and artificial aging at 140 to 170 °C for 6 to 12 h. Often, overaging at 200 °C is also conducted for 7 h to guarantee a more stable

precipitation microstructure [1]. Interestingly, the effect of room temperature storage after quenching is somehow different from wrought alloys. It causes slow artificial aging kinetics similar to that reported for wrought alloys, but no loss in strength [41-43]. However, room temperature storage may be not so critical in the case of Al-Si-Mg cast alloys and the controllability of the effect might often be better. However, room temperature storage can also cause a longer duration of the heat treatment process in some cases.

1.3 Physical aspects of room temperature storage

The following sections provide an introduction to the physical framework to which aging of Al-Mg-Si alloys is based on. Questions and contradictions arising from the current knowledge are depicted.

1.3.1 Natural aging

During room temperature storage after quenching, natural pre-aging, being a more physical meaningful notation, occurs. Recently Banhart *et al.* [18,19] reported that natural aging of Al-Mg-Si alloys is a rather complex process which takes place in up to five distinct stages. These are not fully resolved yet but include individual and combined solute clustering of Si and Mg, and solute vacancy interactions. For long term natural aging Mg,Si co-clusters [18,20,29,44-46] have been found. The nomenclature of Mg,Si co-clusters is not systematic and they have also been termed as both initial- β'' [47] and GP-zones [48] in literature. A visualization of these early stage clusters is extremely difficult. Transmission electron microscopy (TEM) and even high-resolution transmission electron microscopy do not produce distinct contrast [18,49]. High resolution scanning transmission electron microscopy (HRSTEM), the most promising TEM method for this purpose, has not facilitated a successful study on Mg,Si co-clusters up to now, either. Other well-known techniques such as X-ray small angle scattering and small-angle neutron scattering (SANS) also provide only weak contrast. The problem of these methods to resolve early stage clusters in Al-Mg-Si alloys is based on the characteristics of the alloying elements. The low Mg and Si content implies a low signal to noise ratio for any element-sensitive probe. In addition, Mg, Al and Si are neighboring elements in the periodic table resulting in very similar interactions of x-rays and electrons for these three elements [18]. Today, atom probe tomography (APT) is the only technique to visualize Mg,Si co-clusters [18], but even this method operates at its limits and earlier stages as described by Banhart *et al* [18,19] are very hard to identify. Even a determination of an absolute number density or chemical composition for Mg,Si co-clusters formed after long-term natural aging cannot be

given by APT without controversy at the moment. The main restrictions in resolving very small solute aggregates are the low detection efficiency of current APT systems, local magnification effects and unsolved issues with the reconstruction procedure. Nevertheless, a combined approach of APT and measuring properties indirectly influenced by solute clustering such as electrical resistivity, hardness, yield strength, or methods like thermal analysis and positron annihilation spectroscopy is able to contribute significantly to the understanding of the physical mechanism occurring during natural aging. However, an interpretation of indirect data always requires appropriate models. A simple but meaningful model describing the evolution of clusters during natural aging has been established by Zurob and Seyedrezai [46,50]. Their theory assumes that solute-vacancy pairs, which migrate as a complex, immediately form after quenching. Because of attractive interactions between solutes and vacancies, these complexes survive and more solute atoms can be captured to form a cluster. For further cluster growth vacancies need to escape from clusters. This is assumed to be the rate-limiting step of natural aging resulting in a logarithmic time dependence of the model which describes the experimental observations aging quite well within a constricted parameter space. The escaped vacancies can assist the formation of new clusters or the growth of the existing ones. The probability of vacancy-escape depends on the cluster size. Due to this model, all vacancies are bound in clusters at the end of natural aging [50]. This seems to be realistic, because it has already been known for a long time that solutes (e.g. Mg) can suppress the annihilation of quenched-in vacancies in aluminum [2,51,52].

1.3.2 Artificial aging

A number of precipitates have been observed to form during artificial aging. Their nature in terms of structure and chemical composition as well as their transformation path in various types of Al-Mg-Si alloys is rather controversial. Figure 1.6 gives an overview of the possible precipitates evolving during aging at temperatures above room temperature. Some research studies claim that there is an arrangement of Si nanopillars remaining invariant during the precipitation sequence in certain Al-Mg-Si alloys [53], but it is questionable if this is valid for the whole group of Al-Mg-Si alloys [17]. However, the earliest precipitates that are formed during aging at elevated temperatures are spherical GP-I zones with a size of 1 to 3 nm [49,54]. Owing to an unsystematic nomenclature, these are sometimes also called Mg,Si-clusters [29] or clusters [55]. In general, GP-I zones are fully coherent and show f.c.c. structure. The knowledge about their chemical order is more or less restricted to theoretical models [16,47,48]. GP-I zones are thought to transform to β'' [21], and the already needle-like pre- β'' phase has therefore been described as the most developed GP-I zone by some authors [56]. β'' needles [15,54] are the typical precipitates in T6 conditions [20]. Although several structures

have been discussed [16] β'' has been generally accepted to be base-centered monoclinic. β'' needles are aligned along $\langle 100 \rangle_{\text{Al}}$, being fully coherent only along the needle-axis and semi-coherent on the tip of the needle. The chemical composition of the β'' phase was proposed to be Mg_5Si_6 [15,54], but there is a dispute as to whether this is generally true for all types of Al-Mg-Si alloys. It has been reported that the exact composition of β'' is strongly influenced by the composition of the alloy (e.g. the ratio of Mg/Si) [17,57,58]. A large number of other lath-needle- or rod-shaped phases have been reported to appear in the group of Al-Mg-Si alloys in overage conditions [16,59]. For special cases some of those phases might be also found in T6 conditions indicated by the hemicycle arrows in figure 1.6. This depends on the chemical composition and processing of the individual alloy (e.g. β' and B' have been shown to form instead of β'' if AA6060 is deformed before aging [60]). The rod-shaped phase β' [61] is the most prominent one in overaged conditions and shows a hexagonal structure. Additions of Cu generally influence the precipitation sequence [59]. Especially the formation of Q' , also exhibiting a hexagonal structure, is favored [16,20]. The Cu free variant B' of the Q' phase should be mentioned here because it is often found in AA6061, the alloy that is most intensively studied in the scope of this work. Figure 1.6 should only demonstrate that especially for overage conditions, numerous precipitates have been reported for the group of Al-Mg-Si alloys, but does not claim completeness and integrity. The end of the sequences is for sure the equilibrium phase β (Mg_2Si) exhibiting an f.c.c anti-fluorite structure [16,20].

In general, literature seems to be unsystematic. Frequently, phases are discussed using different names or some have been reported as new phase just exhibiting slightly differing lattice constants (e.g. β'' in [16]). However, precaution is recommended in using simplified or old precipitation sequences from literature and applying them to individual types of Al-Mg-Si alloys.

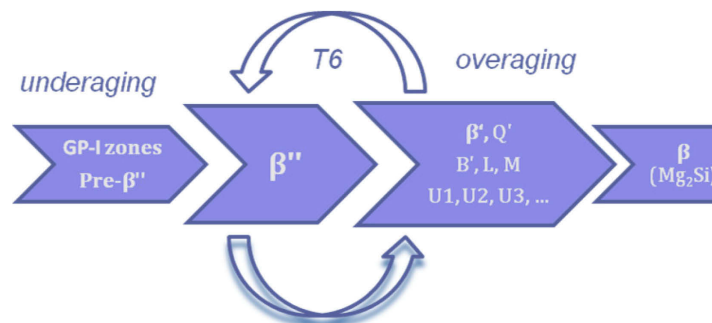


Figure 1.6: Possible precipitates evolving during artificial aging in the group of Al-Mg-Si alloys [16,59]

Many attempts have been made to understand the influence of natural pre-aging on artificial aging of Al-Mg-Si alloys within the last decades [13,23,25,45,62,63]. The discoverers of the

effect already speculated that the diffusion of the Mg and Si atoms is hindered by natural pre-aging for unknown reasons [13]. Ried *et al.* [23] proposed that natural pre-aging reduces the solute super-saturation and vacancy concentration for subsequent artificial aging, both explaining the reduced kinetics of subsequent artificial aging. One of the consequences of this is the lower T6 strength, which is associated with a coarser distribution of precipitates. Additionally, it has been supposed that the reduced solute super-saturation causes a rise of the critical nucleation size for β'' during artificial aging [62]. The only theory that is really accepted today is that Mg,Si co-clusters formed during room temperature storage are smaller than the critical size of nuclei (r_c) of precipitates formed during artificial aging [30,45] (figure 1.7a). Murayama *et al.* [30] supposed that only GP-I zones are large enough to evolve to β'' during artificial aging (figure 1.7b). Furthermore, a lower vacancy concentration in naturally pre-aged material and a complete dissolution of Mg,Si co-clusters during artificial aging was assumed [30,45]. Their model is supported by the observed transformation from GP-I zones to β'' in the case of direct artificial aging [20,21,30,63] and strongly promotes the idea that the majority of Mg,Si co-clusters are really smaller than the r_c of precipitates evolving during artificial aging. In contrast to rich Al-Mg-Si alloys, the positive effect of natural pre-aging in lean Al-Mg-Si alloys such as AA6060 has not been investigated that intensively [23,44]. Chang *et al.* [44] speculated that a different nature of co-clusters which could serve as nuclei for subsequent phases might exist in lean alloys, but this seems to be not conclusive concerning the critical size assumption of Murayama *et al.* [30] and the fact that in lean alloys r_c should be even larger due to a lower solute super-saturation.

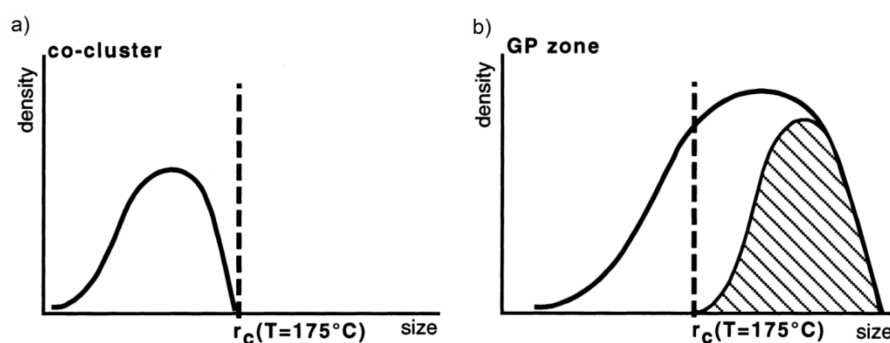


Figure 1.7: Size distribution of Mg, Si co-clusters formed during natural aging and GP-I zones formed at elevated temperatures [30]

As mentioned above, several researchers have claimed that natural pre-aging might reduce the concentration of quenched-in vacancies. This seems reasonable in the light of the current knowledge of natural aging, where it is assumed that most vacancies are bound in clusters at the end of natural aging. Hence, the question remains as to what happens to vacancies

incorporated in Mg,Si co-cluster and what are the consequences from this for the precipitation reactions occurring during artificial aging?

1.4 Approach

In view of the tremendous research efforts made in the past, the objective of finding new strategies to avoid the adverse impact of natural pre-aging on artificial aging in Al-Mg-Si alloys can only be achieved by an even deeper understanding of the mechanisms going on in the material. Historically, the effect of natural pre-aging has preferentially been studied at industrial common artificial aging temperatures (150 to 180 °C), because others than these are not able to guarantee the required properties in most cases. From a scientific point of view, things that are not straightforward could often lead to unexpected results. Therefore, many experimental investigations are not restricted to industrially reasonable aging conditions. Special attention was given to unconventionally high artificial aging temperatures. Furthermore, it was believed that only a multi-method-approach using atom probe tomography as the unique method for a direct visualization of early stage solute clustering and indirect methods combined with theoretical models are able to push the understanding of the physical mechanism responsible for the effect of natural pre-aging. Moreover, it was searched for gaps in the existing knowledge. The following fundamental issues have been dealt with inadequately or have been completely disregarded in the long history of research on the effect of natural pre-aging on the artificial aging of Al-Mg-Si alloys.

- Temperature dependence of artificial aging with regard to the effect of natural pre-aging
- Dissolution of Mg,Si co-clusters during artificial aging in a wide temperature range and different alloys
- Interdependence of the solute super-saturation and the effects of natural pre-aging on artificial aging
- Mg,Si co-cluster vacancy interactions during artificial aging
- Relationship between quenched-in vacancies and the nucleation of β'' for direct artificial aging and artificial aging after natural pre-aging
- Annihilation of quenched-in vacancies in the case of direct artificial aging or aging after natural pre-aging in a wide temperature range

The first three bullet points address experimental issues which have to be dealt with and can possibly be resolved by using state-of-the-art experimental methods. The last three bullet points can just be deduced from a combined approach of experimental investigations and theoretical considerations.

The issues above were considered within the thesis and are expected to support the aim of the work to develop a model which is able to describe the temperature and compositional dependence of the effect of natural pre-aging on artificial aging in the group of Al-Mg-Si alloys. It is believed that this will enable AMAG rolling to take process-related measures, such as optimum design of new stabilization treatments, in addition to alloy-related measures to control the effect of intermediate room-temperature storage, in a significantly more systematic and specific manner than before. Apart from that, a deep understanding of the physical mechanism is essential for computer-aided predictions of the precipitation microstructure and ultimately the property profile in the future.

References

- [1] Kammer C. Aluminium Taschenbuch 1. Düsseldorf: Aluminium-Verlag; 2002.
- [2] Ostermann F. Anwendungstechnologie Aluminium. Berlin Heidelberg New York: Springer-Verlag; 2007.
- [3] Altenpohl D. Aluminium von Innen. Düsseldorf: Aluminium-Verlag; 1994.
- [4] Metallgesellschaft. Statistische Zusammenstellung über Aluminium, Blei, Kupfer, Nickel, Quecksilber, Silber, Zink und Zinn. Frankfurt a. M.: Metallges.; 1. 1890/92 – 53. 1956/65 (1966).
- [5] The Mineral industry, its statistics, technology and trade. New York. 10. 1902 – 50. 1941 (1942).
- [6] Crowson P. Minerals handbook: statistics and analyses of the world's mineral industry. New York: Stockton Press; 1982.
- [7] Metal Statistics 2000 - 2010. Ware, England: World Bureau of Metal Statistics; 2011.
- [8] <http://minerals.usgs.gov/ds/2005/140/aluminum.pdf>; accessed on May 3 2012.
- [9] Wilm A. Metallurgie 1911;8:225.
- [10] Archer RS, Jeffries Z. Trans AIME 1925;71:828.
- [11] Guinier A. Nature 1938;142:569.
- [12] Preston GD. Nature 1938;142:570.
- [13] Brenner P, Kostron H. Z Metall 1939;4:89.
- [14] Smigelskas AD, Kirkendall EO. Trans AIME 1947;171:130.

-
- [15] Zandbergen HW, Anderson SJ, Jansen J. *Science* 1997;277:1221.
- [16] Ravi C, Wolverton C. *Acta Mater* 2004;52:4213.
- [17] Hasting HK, Frøseth AG, Andersen SJ, Vissers R, Walmsley JC, Marioara CD et al. *J. Appl. Phys.* 2009;106:123527-123527-9.
- [18] Banhart J, Chang CST, Liang ZQ, Wanderka N, Lay MDH, Hill AJ. *Adv Eng Mater* 2010;12:559.
- [19] Banhart J, Lay MDH, Chang CST, Hill AJ. *Phys Rev B* 2011;83:art. no. 014101.
- [20] Edwards GA, Stiller K, Dunlop GL, Couper MJ. *Acta Mater* 1998;46:3893.
- [21] Marioara CD, Anderson SJ, Jansen JE, Zandbergen HW. *Acta Mater* 2003;51:789.
- [22] Haase C, Wurts H. *Z Metall* 1941;33:399.
- [23] Ried A, Schwellinger P, Bichsel H. *Aluminium* 1977;53:595.
- [24] Kovacs I, Nagy E, Lendvai J. *Acta Metall* 1972;20:975.
- [25] Dorward RC. *Metall Trans* 1973;4:507.
- [26] Borchers H, Kainz M. *Metall* 1963;17:400.
- [27] Ebner T. Information AMAG Rolling. accessed on May 3 2012.
- [28] <http://aluminium.matter.org.uk/content/html/eng/default.asp?catid=&pageid=1>; accessed on May 3 2012.
- [29] De Geuser F, Lefebvre W, Blavette D. *Phil Mag Lett* 2006;86:227.
- [30] Murayama M, Hono K. *Acta Mater* 1999;47:1537.
- [31] Slámová M, Janecek M, Cieslar M, Šíma V. *Mater Sci Forum* 2007;567-568:333.
- [32] Bryant JD. *Metall Mater Trans A* 1999;30:1999.
- [33] Aluminium Ranshofen Walzwerk Gesellschaft mbH. Ausscheidungshärtung einer Aluminiumlegierung. Patent Number: EP1195449A2. 2001.
- [34] Uchida H, Yoshida H. Process for manufacturing aluminum alloy material having excellent shape fixability and bake hardenability. Patent Number: US5266130. 1993.
- [35] Fujita T, Mitao S, Hasegawa K, Suga M. Method of manufacturing natural aging-retardated aluminum alloy sheet exhibiting excellent formability and excellent bake hardenability. Patent Number: US5441582. 1995.
- [36] Shen TH. Method of manufacturing aluminum articles having improved bake hardenability. Patent Number: US5662750. 1997.
- [37] Bryant JD, Yoshida H, Uchida H. Process and apparatus to enhance the paintbake response and aging stability of aluminum sheet materials and product therefrom. Patent Number: US5718780. 1998.
- [38] Alcan international limited. Heat treatment process for aluminum alloy sheet. Patent Number: WO9607768A1. 1996.

-
- [39] Alcoa inc. Method for shortening production time of heat treated aluminum alloy castings. Patent Number: WO2004065043A2. 2004.
- [40] Rinderer B, Couper M, Xiong X, Gao S, Nie J-F. *Mater Sci Forum* 2010;654–656:590.
- [41] Sha G, Möller H, Stumpf WE, Xia JH, Govender G, Ringer SP. *Acta Mater* 2012;60:692.
- [42] Möller H, Govender G, Stumpf WE. *Int J Cast Metals Res* 2007;20:340.
- [43] Möller H, Govender G, Stumpf WE, Pistorius PC. *Int J Cast Metals Res* 2010;23:37.
- [44] Chang CST, Wieler I, Wanderka N, Banhart J. *Ultramicroscopy* 2009;109:585.
- [45] Murayama M, Hono K, Saga M, Kikuchi M. *Mater Sci Eng A* 1998;250:127.
- [46] Seyedrezai H, Grebennikov D, Mascher P, Zurob HS. *Mater Sci Eng A* 2009;525:186.
- [47] van Huis MA, Chen JH, Sluiter MHF, Zandbergen HW. *Acta Mater* 2007;55:2183.
- [48] van Huis MA, Chen JH, Zandbergen HW, Sluiter MHF. *Acta Mater* 2006;54:2945.
- [49] Buha J, Lumley RN, Crosky AG, Hono K. *Acta Mater* 2007;55:3015.
- [50] Zurob HS, Seyedrezai H. *Scr Mater* 2009;61:141.
- [51] Panseri C, Federighi T, Ceresara S. *Trans Metall Soc AIME* 1963;227:1122.
- [52] Panseri C, Gatto FG, Federighi T. *Acta Metall* 1958;6:198.
- [53] Chen JH, Costan E, van Huis MA, Xu Q, Zandbergen HW. *Science* 2006;312:416.
- [54] Anderson SJ, Zandbergen HW, Jansen JE, Taeholt C, Tundal U, Reiso O. *Acta Mater* 1998;46:3283.
- [55] Serizawa A, Hirosawa S, Sato T. *Mater Sci Forum* 2006;519-521:245.
- [56] Marioara CD, Anderson SJ, Jansen J, Zandbergen HW. *Acta Mater* 2001;49:321.
- [57] Hasting HK, Lefebvre W, Marioara C, Walmsley JC, Anderson S, Holmestad R et al. *Surf Inter Anal* 2007;39:189.
- [58] Buha J, Lumley RN, Crosky AG. *Phil Mag Lett* 2008;88:373.
- [59] Chakrabarti DJ, Laughlin DE. *Prog Mater Sci* 2004;49:389.
- [60] Teichmann K, Marioara CD, Andersen SJ, Pedersen KO, Gulbrandsen-Dahl S, Kolar M et al. *Phil Mag* 2011;91:3744.
- [61] Vissers R, van Huis MA, Jansen J, Zandbergen HW, Marioara CD, Anderson SJ. *Acta Mater* 2007;55:3815.
- [62] Huppert-Schemme G. *AlMgSi-Bleche für den Fahrzeugbau – Metallkunde und Fertigungstechnik*. Düsseldorf: Aluminium-Verlag; 1997.
- [63] Suzuki H, Kanno M, Itoh G. *Aluminium* 1981;57:628.

2 TEMPERATUR DEPENDENCE OF AGING

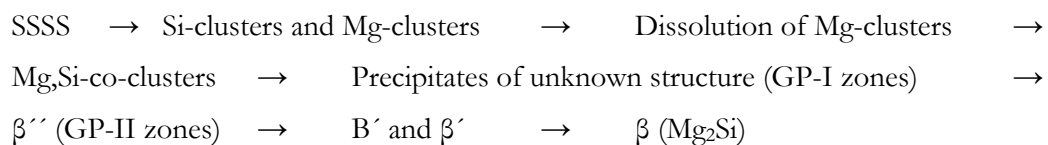
In this chapter different artificial aging strategies are investigated in a wide temperature range for the rich Al-Mg-Si alloy AA6061. Hardness data analysis is used to study the temperature dependence of precipitation kinetics and dissolution processes. Based on microstructural observations using atom probe tomography and electrical resistivity measurements a theoretical model explaining the temperature dependence of artificial aging taking account of the effect of natural pre-aging is presented. The introduced “vacancy-prison mechanism” addresses Mg,Si co-cluster vacancy interactions during artificial aging and is the basis to which all following chapters refer to.

Mechanisms Controlling the Artificial Aging of Al-Mg-Si Alloys *

In this study the artificial aging behavior of the Al-Mg-Si alloy AA6061 was investigated in the range of 150 to 250 °C by atom probe tomography, hardness and resistivity measurements for various thermal histories. It was found that the precipitation kinetics and age hardening response of artificial aging at temperatures below 210 °C are lowered by prior natural aging but enhanced above this temperature. A hardness data analysis was used to evaluate the temperature dependence of precipitation kinetics and dissolution processes. Supported by theoretical considerations, it is assumed that artificial aging of Al-Mg-Si alloys is controlled via the concentration of mobile vacancies. The “vacancy-prison mechanism” proposed determines the mobile vacancy concentration in the case of natural pre-aging by temperature-dependent dissolution of co-clusters and solute-vacancy interactions.

2.1 Introduction

Precipitation hardenable Al-Mg-Si alloys are widely used in cast, wrought and extruded form for construction, automotive engineering, shipbuilding and the aircraft industry [1,2]. A high ratio of strength to density, very good corrosion resistance, excellent surface properties and weldability together with relatively low price make these alloys commercially very attractive [3]. To gain insight in the artificial aging of Al-Mg-Si alloys, it is useful to examine the precipitation sequence of the commercially alloy AA 6061, which was determined by Edwards *et al.* [1] by means of differential scanning calorimetry (DSC) as follows:



Precipitation from the super-saturated solid solution (SSSS) starts with individual solute clustering of Si and Mg [1]. Due to difficulties in the experimental analysis of early stage precipitates, more or less purely theoretical considerations of the structure are available [4]. Co-clusters form after the dissolution of Mg-clusters and have been found in naturally aged alloys. Compared to co-clusters, GP-I zones are thermally more stable, contain more solute atoms, and are spherical, with typical size of 1 to 3 nm [5]. They are the earliest precipitate type in the sequence, which produce a distinct contrast for transmission electron microscopy (TEM) identification [6]. In general, all early stage precipitates are fully coherent and show f.c.c.

*Pogatscher S, Antrekowitsch H, Leitner H, Ebner T, Uggowitzer PJ. Acta Mater 2011;59:3352.

structure [4,7]. Since the notation of clusters and zones is not consistent in the literature (for example, co-clusters are termed as both initial- β'' [4] and GP-zones [7]; GP-I zones [1] are also labeled as pre- β'' [4,7]), in this work only the terms co-cluster and GP-I zone are used. The needle-like β'' (Mg_5Si_6) precipitates are associated with peak aged states [5]. They are aligned along $\langle 100 \rangle_{\text{Al}}$, monoclinic and only fully coherent along the needle-axis. Consecutively, the rod-shaped phases β' and B' are formed. These phases are typical for overaged microstructures. Various other phases have been observed at this stage of the precipitation sequence. Some contain Cu (Q'), but all of them show a hexagonal structure, are aligned along $\langle 100 \rangle_{\text{Al}}$, and are mainly distinguishable by their lattice constant [1,6-9]. Finally, the platelet-like equilibrium phase β (Mg_2Si) is formed, which shows an f.c.c anti-fluorite structure [1,4,7,10].

The effect of prior natural aging on precipitation hardening in Al-Mg-Si alloys has been well documented for common artificial aging temperatures (around 170 °C). A strong adverse influence of natural pre-aging on the precipitation kinetics and age hardening response has been reported for an intermediate storage period longer than a few minutes and alloys rich in Mg and Si [11-15]. Few alloys with low Mg and Si content show a slight positive influence of natural pre-aging [12,16]. Due to the fact that such alloys are commercially less important, however, in the present work the focus is on widely used high strength Al-Mg-Si alloys, which generally show a negative response of natural pre-aging. In most heat-treated semi-finished products (e.g. plates), it is impossible to avoid prior natural aging for logistical reasons. Accordingly the energy efficiency, production capacity, profitability and achievable strength is reduced [2]. The use of Al-Mg-Si alloys as hardenable auto body sheet has also revived the interest in investigating the negative influence of natural pre-aging in the last few years. A typical paint-bake cycle of 30 min at 175 °C is much too short to reach T6 strength, which requires 10 to 20 h at 175 °C for naturally pre-aged Al-Mg-Si alloys. Hence, various heat treatments for optimizing the paint-bake response were examined [17-22] and patented. Several reasons for the negative influence of intermediate storage on the artificial aging behavior have been discussed in the past. Ried *et al.* [12] found that natural aging reduces the solute supersaturation and vacancy concentration for subsequent artificial aging. This also causes a rise of the critical nucleation size for the most important strengthening phase β'' [23]. Murayama *et al.* [24] thought that co-clusters, which form during room temperature storage, are too small to act as nucleation sites for β'' and would be completely reverted at artificial aging temperature. Furthermore, a lower vacancy concentration in naturally pre-aged material was assumed. It is generally believed that stable hypercritical GP-I zones must be formed to minimize the negative influence of intermediate storage [24]. This assumption is supported by the observed transformation from GP-I zones to β'' in the case of direct artificial aging [1,3,25,26]. It is generally known that quenched-in vacancies play an important role in precipitation processes

by supporting solute diffusion. Although the effect of natural aging has been extensively studied, considerable confusion remains regarding the role of co-clusters and vacancies during artificial aging. Thus, the present work was performed to clarify the mechanisms which control artificial aging of Al-Mg-Si alloys, especially with regard to various thermal histories.

2.2 Experimental methods

The alloy AA6061 was supplied by AMAG Rolling in the form of wrought plate. Its composition is given in table 2.1.

Table 2.1: Composition of alloy AA 6061

Element	Al	Si	Fe	Cu	Mn	Mg	Cr	Zn	Ti
at.%	Balance	0.58	0.25	0.09	0.05	0.92	0.08	0.03	0.05
wt.%	-	0.60	0.52	0.22	0.11	0.82	0.15	0.07	0.08

Solution heat treatment of hardness test samples ($20 \times 25 \times 2.5 \text{ mm}^3$, grain size $\sim 100 \mu\text{m}$) was performed in a circulating air furnace (Nabertherm N60/85 SHA) at $570 \text{ }^\circ\text{C}$ for 20 min. Specimens were then heat treated according to the time-temperature sequences described in figure 2.1 Abbreviation ‘A’ denotes direct aging.

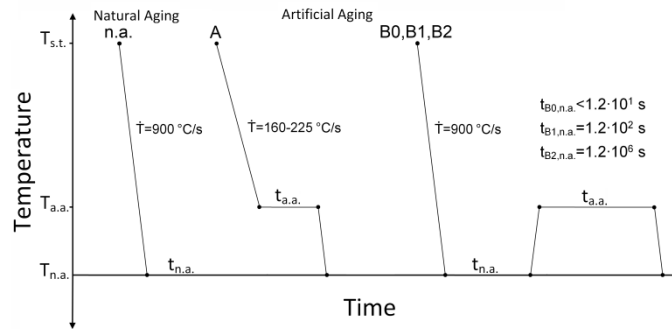


Figure 2.1: Heat treatment procedures

In order to archive good temperature accuracy and optimal heat transfer, an oil bath (LAUDA Proline P 26) with an integrated basin filled with a low-melting alloy as high performance heat transfer medium (Bi57Sn43) was used. Samples were positioned in a cage near a platinum thermometer (Pt100), which facilitated a temperature accuracy of $\pm 0.3 \text{ }^\circ\text{C}$ for direct quenching and $\pm 0.1 \text{ }^\circ\text{C}$ for artificial aging. For the heat treatment procedures ‘B1’ and ‘B2’ quenching

was carried out in water at RT, followed by room temperature storage for $1.2 \cdot 10^2$ s (B1) and $1.2 \cdot 10^6$ s (B2). With water quenching a cooling rate of approximately 900 °C/s was achieved (measured in the range from 540 °C to 290 °C). Quenching in Bi57Sn43 resulted in a cooling rate of about 225 °C/s for 150 °C and 160 °C/s for 250 °C metal bath temperature, respectively. Artificial aging was performed in the Bi57Sn43 basin for A, B1, and B2 at temperatures ranging from 150 to 250 °C, in steps of 10 °C. Natural aging (n.a.) was carried out at room temperature directly after water quenching.

Brinell hardness measurements (HBW 2.5/62.5) were performed in an EMCO-Test M4 unit. A maximum standard deviation of 1.5 HBW 2.5/62.5 was achieved.

Electrical resistivity measurements were carried out at -196 °C in liquid nitrogen using a custom made four-point probe system and drawn coiled AA6061 wires (1050 mm length, 0.83 mm diameter) as samples. Current and potential were measured separately with two digital multimeters (HP 34401 A) for a nearly constant applied current of 2 A [27,28]. To minimize measurement errors, the change in specific resistivity resulting from aging experiments ($\Delta\rho$) was calculated from equation (2.1). The as-quenched specific electrical resistance (ρ_0) was fixed at 1491 ± 15 nΩcm. R_a is the resistance after heat treatment and R_0 describes the as-quenched state for a specimen [27,28]. For $\Delta\rho$ an accuracy of ± 5 nΩcm was achieved. Solution treatment of the coils was done under Ar atmosphere for 20 min at 570 °C. Subsequent quenching was performed in water at RT and artificial aging was accomplished in an oil bath. Since it is not possible to measure the as-quenched resistivity for heat treatment A, procedure 'B0' was performed instead, which is similar to B1, but avoiding natural aging longer than $1.2 \cdot 10^1$ s.

$$\Delta\rho = \rho_0 \frac{R_a - R_0}{R_0} \quad (2.1)$$

In order to prepare needle-shaped specimens for atom probe tomography (APT), small rods with cross-section 0.3×0.3 mm² were cut out of corresponding hardness test samples. The specimens were then prepared by a standard two-step method: first by electropolishing of the small rods in a layer of 15 % perchloric and 85 % acetic acid solution topped over a dielectrical liquid called Galden™ which is a perfluoropolyether from Solvay Solexis; and secondly, using an electrolyte of 2 % perchloric acid in butoxyethanol [29]. APT was performed on a LEAP™ 3000 X HR atom probe at a temperature of -238 °C. All measurements were performed with a pulse fraction of 15 % under ultra-high vacuum ($< 10^{-10}$ mbar). The reconstruction procedure and analysis were conducted using the software package IVAS 3.4.3™ from Imago Scientific Instruments Corporation (Madison, WI, USA). For all heat treatment states at least $9 \cdot 10^6$ ions

were analyzed, although for purpose of clarity smaller sections of three dimensional atom maps are presented here. In order to identify enriched regions in an analyzed volume, isoconcentration surfaces [30] were used.

2.3 Experimental results

2.3.1 Age hardening behavior

2.3.1.1 Natural aging

A hardness curve for natural aging at 25 °C is shown in figure 2.2. After a negligible initial change in hardness and a rapid hardness increase, a nearly constant value of 73 HBW was reached which can be associated with the presence of co-clusters [1,26].

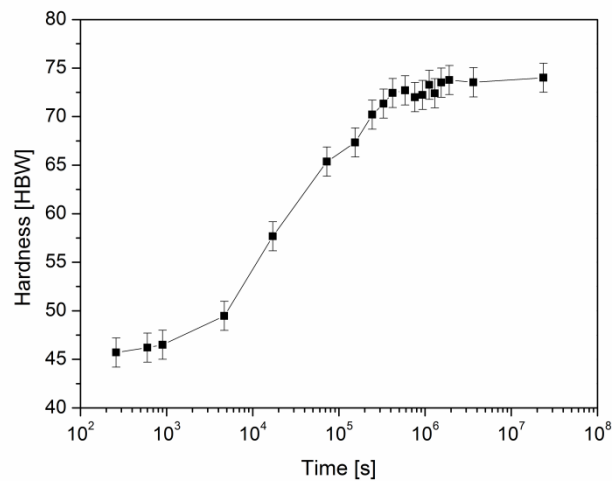


Figure 2.2: Hardness curve for natural aging at 25 °C

2.3.1.2 Artificial aging

Time-temperature-hardness diagrams (TTH) showing typical C-curves for iso-hardness-lines are presented for various heat treatment procedures in figure 2.3. Procedures A (figure 2.3a) and B1 (figure 2.3b) caused a similar age hardening behavior at low temperatures, but higher hardness values were achieved at elevated artificial aging temperatures by B1. A strongly different artificial aging behavior was found for the heat treatment procedure B2 (figure 2.3c). At low temperatures, the hardness stayed nearly constant at the value reached after natural aging over a long period, until a weak increase occurred. At high temperatures a significant reversion took place. Compared to A or B1, the overall variation of the hardness in the assayed time-temperature field was much smaller for B2. In addition, the C-curve seemed to shift to

higher temperatures with a larger temperature dependence (greater slope of the C-curve), which generated significantly higher hardness values at high temperatures for B2.

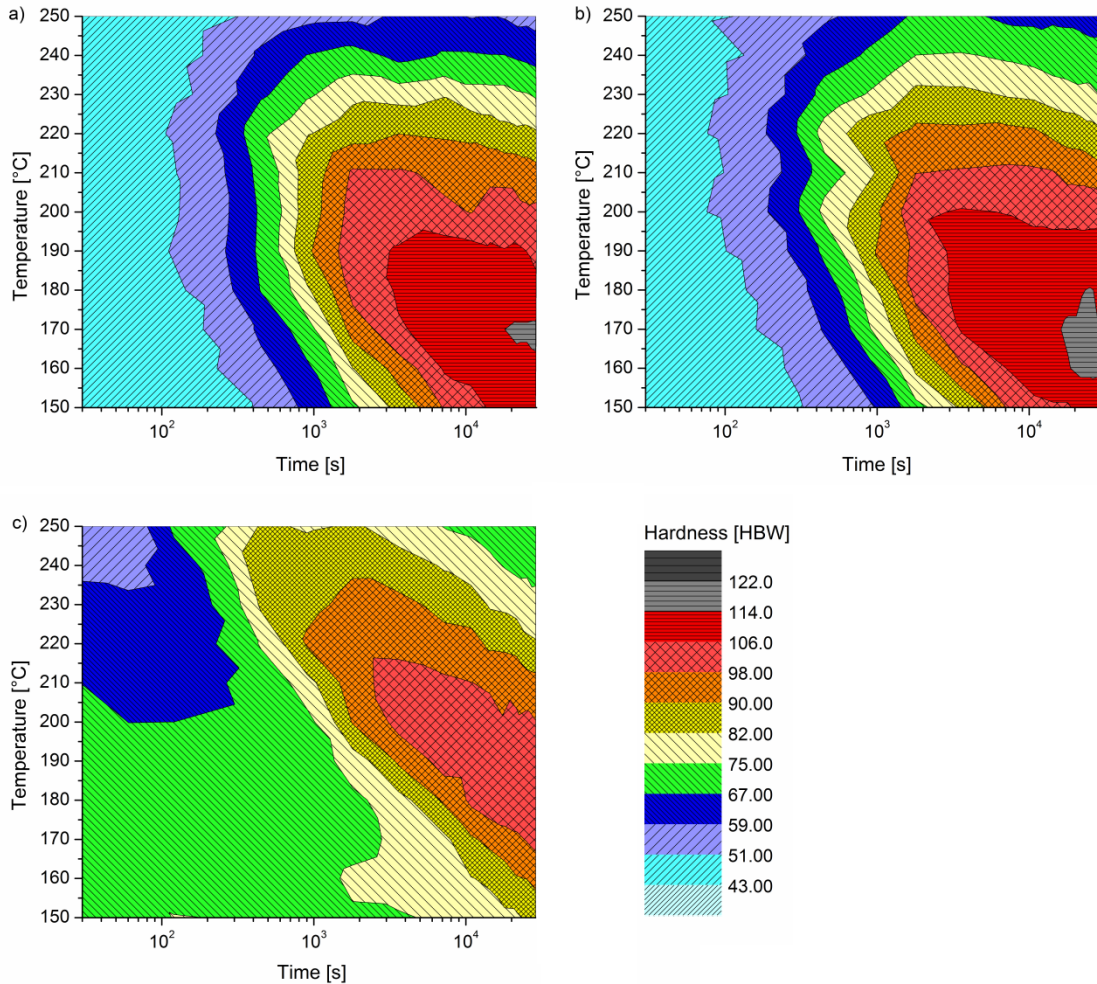


Figure 2.3: Time-temperature-hardness diagrams (TTH) for the heat treatment procedures (a) A, (b) B1 and (c) B2

For a more detailed evaluation, a comparison of hardness curves obtained by the artificial aging procedures A, B1 and B2 at 170 °C is shown in figure 2.4a. Similar hardness curves were observed for direct aging (A) and very short room temperature storage of $1.2 \cdot 10^2$ s (B1). For long-term naturally pre-aged samples (B2) strongly retarded aging kinetics was found. The hardness stayed nearly constant at the value reached after natural aging (n.a.) for 1.8 ks until an increase with a reduced slope compared to A and B1 occurred. No significant reversion took place. Figure 2.4b shows the hardness curves of A, B1 and B2 at 210 °C. For A and B1 treatments nearly identical hardness curves were found, revealing a lower peak hardness and starting overaging compared to figure 2.4a. For B2 a significant reversion occurred. Following this the slope of the hardness curve and achievable peak hardness was similar to A and B1. The

hardening behavior for A, B1 and B2 at 250 °C is shown in figure 2.4c. Significant differences between all heat treatment procedures appeared. Contrary to low artificial aging temperatures, the procedure A produced the slowest aging kinetics and lowest peak hardness. An increase in hardness was achieved by B1. The highest hardness and fastest aging kinetics were found for long-term naturally pre-aged samples (B2) after a distinct reversion.

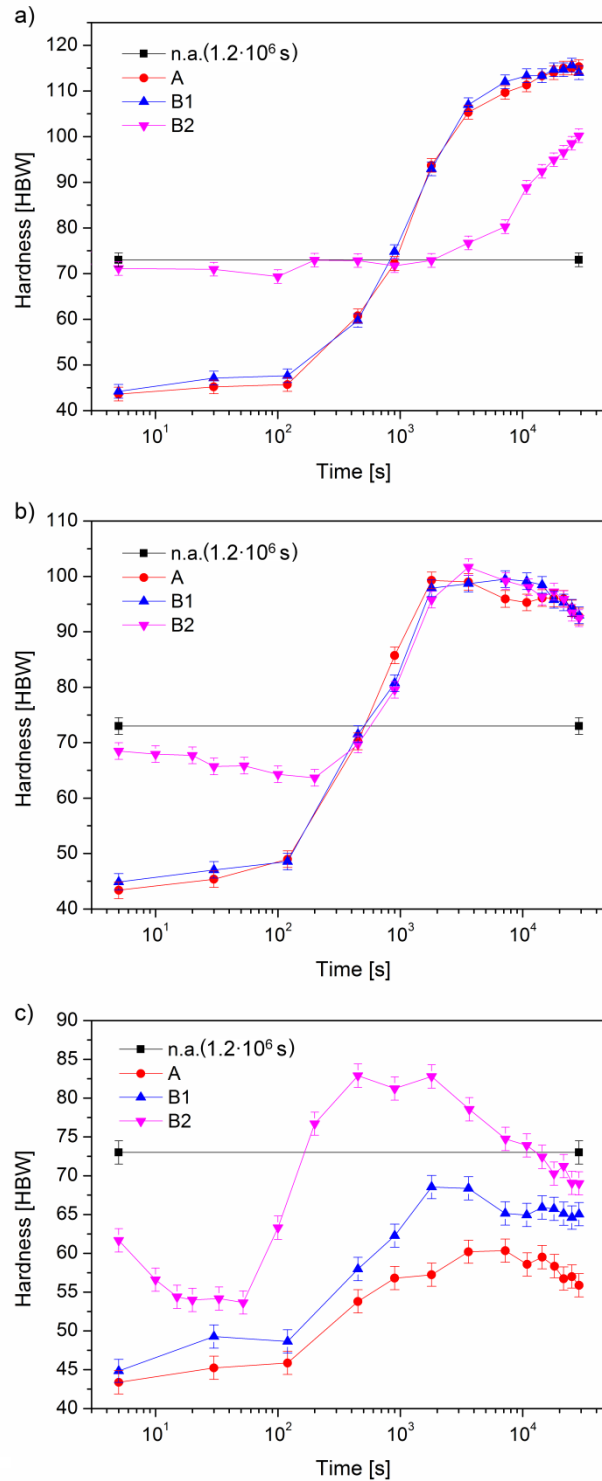


Figure 2.4: Hardness curves for artificial aging procedures A, B1 and B2 at (a) 170 °C, (b) 210 °C and (c) 250 °C

Isochronal (1.8 ks) hardness curves are given in figure 2.5. Artificial aging at 150 °C caused a similar hardness for all treatments. Temperatures below 210 °C led to higher hardness values for A and B1 compared to B2, with maximum hardness around 190 °C. Heat treatment procedure B2 shifted the maximum hardness to 210 °C. For temperatures above 210 °C, superior hardness was found for B2.

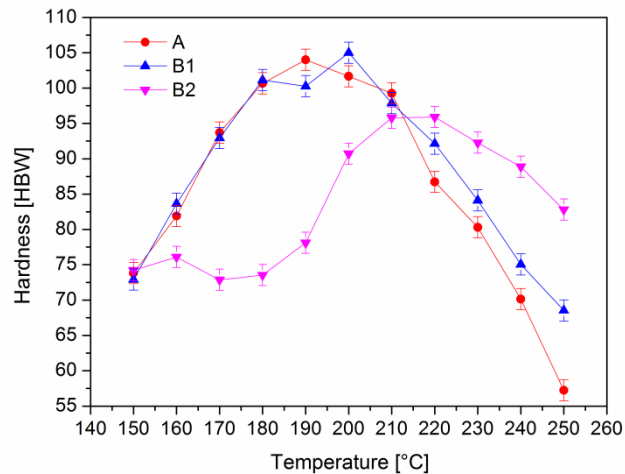


Figure 2.5: Isochronal hardness curves for 1.8 ks artificial aging according to A, B1 and B2

2.3.2 Microstructural evolution

2.3.2.1 Electrical Resistivity

Isochronal resistivity curves for 1.8 ks artificial aging according to B0 and B2, including the resistivity reached after natural aging, are shown in figure 2.6. Referred to the as-quenched state, natural aging (n.a.) of $1.2 \cdot 10^6$ s caused a strong resistivity increase ($\Delta\rho = 167 \text{ n}\Omega\text{cm}$). Subsequent artificial aging (B2) at 150 °C did not significantly influence the resistivity. Between 150 and 190 °C, a slight decrease in resistivity was found for B2. Above 200 °C a stronger decrease took place, such that $\Delta\rho$ became negative above 210 °C. Artificial aging immediately after quenching (B0) results only in a slightly positive $\Delta\rho$ for B0 at low artificial aging temperatures, whereby $\Delta\rho$ decreases with increasing temperature and drops below the as-quenched state above 165 °C. For 250 °C the heat treatment procedures B0 and B2 showed the smallest difference. In general, a strong influence of long-term natural aging on resistivity during artificial aging was found.

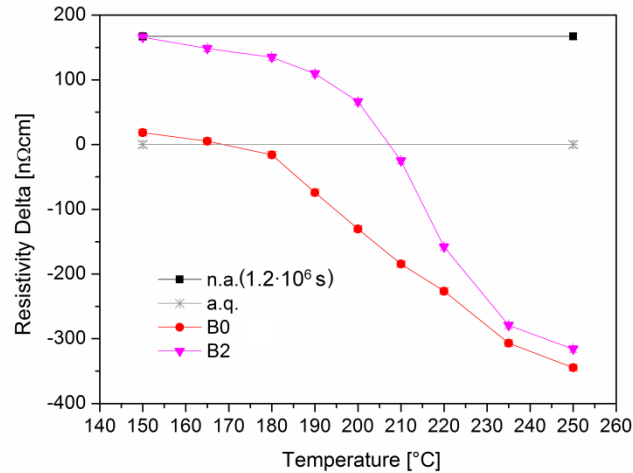


Figure 2.6: Isochronal resistivity curves for 1.8 ks artificial aging according to B0 and B2

2.3.2.2 Atom probe tomography

The microstructure induced by various heat treatment procedures was investigated by atom probe tomography (APT). For visualization, small cubes with identical size ($45 \times 45 \times 60 \text{ nm}^3$) were cut off the individually analyzed volume, which show three-dimensional reconstructions of the Al-matrix (figure 2.7). An important aspect of the APT study was the detection of small solute enriched regions formed by long-term natural pre-aging. Due to the fact that these regions could not be seen easily, isoconcentration surfaces were generated (figure 2.7). The threshold value was arbitrarily set to 2.8 at.% Mg, which is three times higher as the average Mg concentration of the alloy. A minimum solute detection number is not defined by this method, but it was found that the smallest isoconcentration surfaces contain about 15 Mg atoms, taking detection efficiency into account. Therefore, the calculated number densities are affected by both the isoconcentration value used and the detection efficiency of the atom probe. Because these parameters are equal for each sample investigated a comparison of number densities is appropriate, although the actual number density is assumed to be higher. Mg enriched regions with a number density of $6.8 \cdot 10^{23} \text{ m}^{-3}$ were found after natural aging (figure 2.7a). Proxigrams based on these isosurfaces clearly show a co-segregation tendency for Si. Hence, these small regions (black surface) were related to co-clusters [1,24] (Individual proxigrams are not displayed because detailed analysis of the chemical composition of precipitates is beyond the purpose of this paper and part of an additional study. For proxigram analysis see [31,32]). An atom map of the artificial aging state (3.6 ks at 170 °C, according to B2) is illustrated in figure 2.7b. Applying an isoconcentration of 2.8 at.% of Mg isoconcentration surfaces corresponding to co-clusters (black surface) with a number density of $6.7 \cdot 10^{23} \text{ m}^{-3}$ and GP-I zones (green surface) with a number density of $1.2 \cdot 10^{23} \text{ m}^{-3}$ were found. In the absence of TEM-investigations the co-clusters and GP-I zones were differentiated by size, shape and chemical

composition according to proxigrams [31,32]. GP-I zones are more spherical, larger and contain higher solute enrichment than co-clusters, which are formed during natural aging [6]. For the 28.8 ks artificial aging at 170 °C in the context of heat treatment procedure B2, beside co-clusters ($4.2 \cdot 10^{23} \text{ m}^{-3}$) and GP-I zones ($1.2 \cdot 10^{23} \text{ m}^{-3}$) few needle-like regions with a number density of $0.94 \cdot 10^{23} \text{ m}^{-3}$ were observed (figure 2.7c). Due to their typical shape and orientation along $\langle 100 \rangle_{\text{Al}}$, they were related to β'' [5,33]. The isoconcentration surface of 2.8 at.% Mg (yellow grid) was complemented by an isoconcentration surface of 10 at.% Mg (yellow surface), which illustrates the more pronounced solute enrichment in this phase.

Figure 2.7d shows the microstructure generated by the 28.8 ks aging at 170 °C (heat treatment procedure A). Compared to figure 2.7c, a denser distribution of β'' with a number density of $4.0 \cdot 10^{23} \text{ m}^{-3}$ and very few co-clusters ($0.47 \cdot 10^{23} \text{ m}^{-3}$) were found. Additional GP-I zones ($1.4 \cdot 10^{23} \text{ m}^{-3}$) were present.

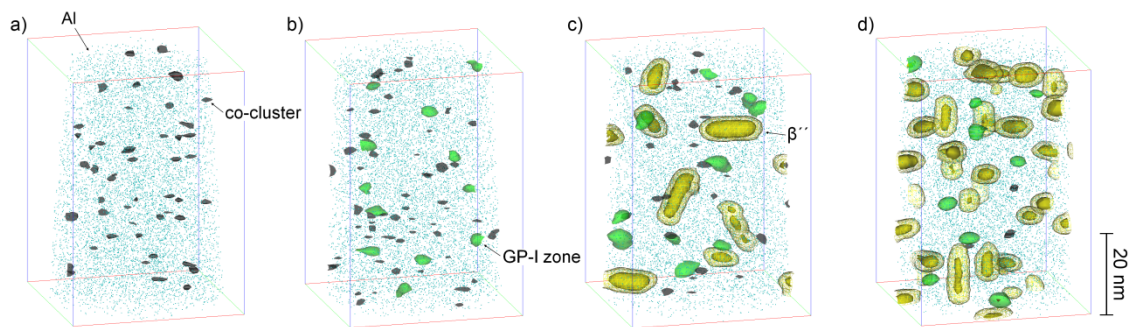


Figure 2.7: Atom probe analysis for (a) long-term natural aging, (b) 3.6 ks and (c) 28.8 ks aging according to heat treatment procedure B2, respectively, and (d) 28.8 ks aging according to heat treatment procedure A at 170 °C

2.4 Hardness data analysis

2.4.1 Temperature dependence of co-cluster dissolution

Between 190 °C and 250 °C, a significant hardness decrease for short artificial aging of naturally pre-aged samples (B2), so called ‘reversion’, was seen (figure 2.3c). Figure 2.8 shows the values of the hardness minima (reversion maxima) at the corresponding temperatures.

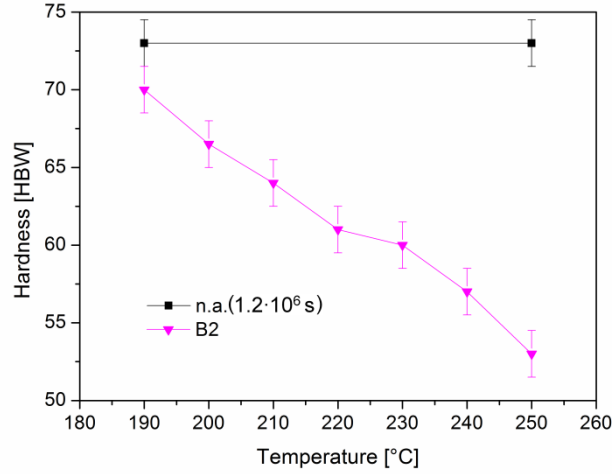


Figure 2.8: Hardness minima (reversion maxima) at the corresponding temperatures

For analyzing the temperature dependence of co-cluster dissolution a simple model was used. It is assumed that the hardness is proportional to the precipitation hardening contribution to yield strength. All precipitation types studied are shearable and can be treated as strong obstacles [34-36]. Thus, the contribution of aging to hardness can be roughly expressed as a function of the relative volume fraction of precipitates (f_r) in accordance to Esmacili *et al.* [36] by equation (2.2).

$$\Delta H \propto \sqrt{f_r} \quad (2.2)$$

If we neglect slightly increasing solution strengthening, a relationship between the relative volume fraction of natural aging co-clusters ($f_r^{n.a.}$) and the decreasing hardness during reversion may be supposed (equation (2.3)). $f_r^{n.a.}$ was defined as 1 at the start of artificial aging for long-term natural aging. $H_{n.a.}$ represents the hardness for long-term natural aging according to figure 2.2, and the as-quenched hardness ($H_{a.q.}$) was set to 43 HBW.

$$f_r^{n.a.} = \left(\frac{H - H_{a.q.}}{H_{n.a.} - H_{a.q.}} \right)^2 \quad (2.3)$$

The kinetics of co-cluster dissolution can be expressed using equation (2.4). It comprises the results of a mathematical model for a diffusion-controlled solution of a second phase in an infinite matrix and some approximations (described in detail by Esmacili *et al.* [36]).

$$f_r^{n.a.} = (1 - B \cdot t^{0.5})^3 \quad (2.4)$$

The temperature dependence of B can be modeled by an Arrhenius-type equation (equation 2.5). In this way, it is possible to determine the activation energy ($Q_{diss.}$) of co-cluster dissolution.

$$B = B_0 \cdot \exp\left(\frac{-Q_{diss.}}{k \cdot T}\right) \quad (2.5)$$

Hardening curves were normalized (equation (2.3)) and fitted by a least squares algorithm according to equation (2.4). In the temperature range of 190 to 250 °C, an activation energy for the co-cluster dissolution of 0.79 eV comparable with the value given in [36] was found from the Arrhenius plot shown in figure 2.9.

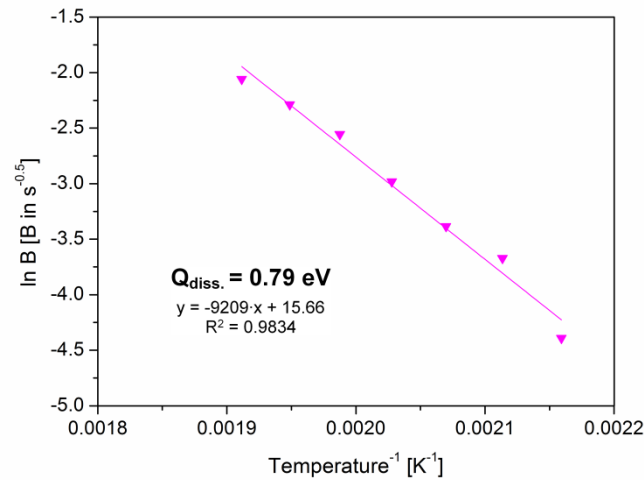


Figure 2.9: Arrhenius plot of equation (2.5)

2.4.2 Temperature dependence of precipitation kinetics

A simple analysis of hardness data was performed to examine the temperature dependence of precipitation kinetics during the major hardness increase caused by various thermal histories. Hardening curves were normalized and fitted by a least squares algorithm by the Johnson-Mehl, Avrami, Kolmogorov equation (equation (2.6)). H represents the actual hardness and H_{peak} is the corresponding peak hardness, whereby the square root in the normalization results from equation (2.2). A value of 1.4 was found to be the optimal value of the Avrami index (n) for a description of the hardness curves analyzed. k is the temperature dependent rate constant. Due to the normalization in equation (2.6), only the timescale is influenced by k . Note that this is just a mathematical model and hardly covers physically based background. However, the

method is very feasible for a simple description of precipitation kinetics during the major hardness increase, so that for 90 % of the fitted curves an R^2 -value greater than 0.97 was achieved. For fitting hardness data based on the heat treatment procedure B2, only sections of the hardness curves, where the dissolution of co-clusters has been completed for more than 95 % (equation (2.4)), were used. Due to the scope of equation (2.4) fitting of B2 was not possible below 190 °C.

$$\left(\frac{H - H_{a.q.}}{H_{peak} - H_{a.q.}} \right)^2 = 1 - \exp(-k \cdot t^n) \quad (2.6)$$

A direct comparison of the rate constants for heat treatment procedures A, B1 and B2 is shown in figure 2.10. The absolute values were found to be similar for A and B1. For B2, however, they were much lower at lower artificial aging temperatures and higher at increased temperatures, which is consistent with the observations shown in figure 2.4. The higher rate constant caused by the heat treatment procedure B2 at elevated temperature, in particular, has not been previously reported.

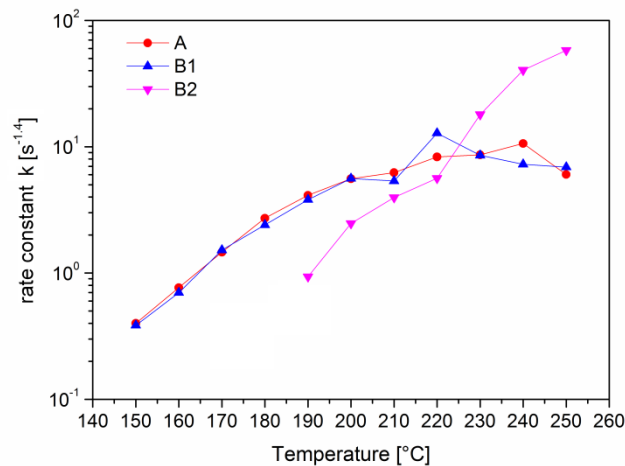


Figure 2.10: Comparison of the rate constants for heat treatment procedures A, B1 and B2

If a single thermally-induced process predominates, the relationship of the rate constant (k) with the temperature can be modeled by an Arrhenius-type equation (equation (2.7)). Hence, it is possible to determine apparent activation energies related to the precipitation process ($Q_{a.a.}$) by analyzing the discussed sections of the hardness curves for various artificial aging procedures.

$$k = k_0 \cdot \exp\left(\frac{-Q_{a.a.}}{k_B \cdot T}\right) \quad (2.7)$$

In the temperature range of 150 to 200 °C, for heat treatment procedure A an activation energy of 0.93 eV was found from the Arrhenius plot shown in figure 2.11a. Above 200 °C, no linear correlation was observed. B1 generated a similar behavior as found for A, with an activation energy of 0.94 eV between 150 and 200 °C (figure 2.11b). An Arrhenius relationship was observed in the range of 190 to 250 °C for naturally pre-aged samples (B2, figure 2.11c). Therefore the temperature dependence of the rate constant can be described by the revealed activation energy of 1.45 eV.

2.5 Discussion

Although the time-temperature-precipitation and -property diagrams for the Al-Mg-Si alloy AA6061 have been described in previous works [9,37], a systematic examination of the thermal history is still lacking. In the present study the heat treatment procedure was found to have a substantial impact on the time-temperature dependence of artificial aging of alloy AA6061 (figure 2.3). Below 210 °C, direct artificial aging (A) caused a behavior similar to that of short-term natural aging prior to artificial aging (B1). Long-term natural aging (B2), however, produced a detrimental effect on the artificial aging behavior (figure 2.4a). While the negative effect of prior room temperature storage on artificial aging behavior at common temperatures (e.g. 170 °C) has long been known [11-15], the influence of natural pre-aging on artificial aging at high temperatures has not been reported until now. Here it was found that precipitation kinetics and the age hardening response of artificial aging were enhanced by natural pre-aging at temperatures above 210 °C (figure 2.4b). Although the effect of natural aging has been studied extensively, the mechanisms suggested cannot explain the different temperature dependencies related to the various thermal treatments. Both nucleation and growth are controlled by diffusion and the solute super-saturation. For a specific alloy the metastable solvus line for the same type of precipitate should be equal for various heat treatment procedures.

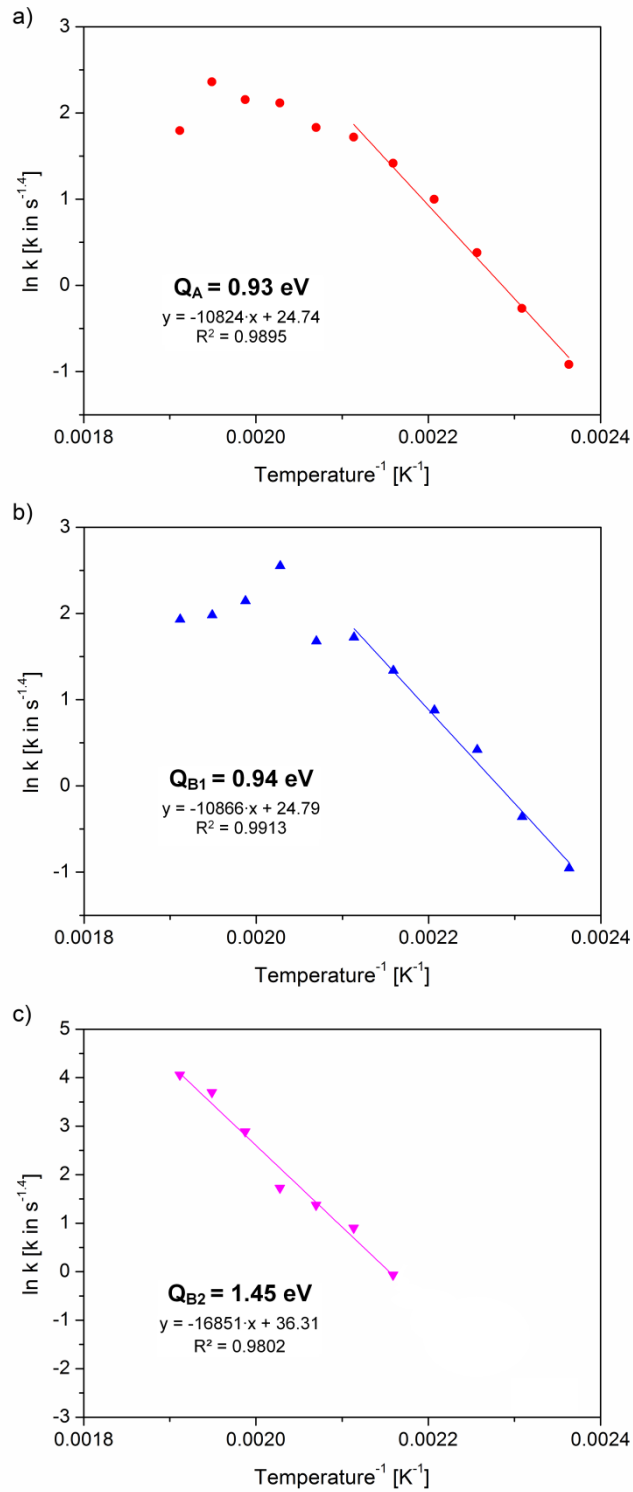


Figure 2.11: Arrhenius plot of equation (2.7) for heat treatment procedures (a) A, (b) B1 and (c) B2

For artificial aging according to A or B1 the initial solute super-saturation depends mainly on artificial aging temperature, whereby an increased solubility at higher temperature reduces the solute super-saturation. Long-term natural pre-aging (B2) reduces the initial solute super-saturation for subsequent artificial aging because of cluster formation. Therefore the solute

super-saturation for B2 is always lower than for the A or B1 procedures, even if very fast dissolution of co-clusters at high artificial aging temperatures occurs. Hence, a decreasing solute super-saturation might be a possible explanation for the stagnation of the rate constant of A or B1 above 210 °C, but not for the increasing rate constant of B2 in the same temperature range (figure 2.10). A linear Arrhenius relationship with a high apparent activation energy related to the precipitation process was found for B2 between 190 to 250 °C (figure 2.11c), although the super-saturation decreases with rising temperature. Thus the kinetics of B2 must be controlled by another thermally activated mechanism. Besides the solute super-saturation, diffusion processes effect nucleation and growth. It is generally known that quenched-in vacancies support diffusion during precipitation reactions. However, the significance of vacancies during artificial aging has only been poorly investigated. In the following we present a detailed analysis of their function in order to better understand the above-described phenomena.

2.5.1 Role of vacancies

Equilibrium diffusion of Mg and Si at a certain temperature can be described by the activation energy of mono-vacancy formation (E_F) and their migration energy (E_M) [38]. If quenched-in vacancies are involved, the solution treatment temperature must be taken into account in vacancy formation instead of the actual aging temperature [38]. Equation (2.8) describes the diffusion by the formation of vacancies at solution treatment temperature ($T_{s.t.}$) and their migration at artificial aging temperature ($T_{a.a.}$) [38].

$$D \propto A \cdot \exp\left(-\frac{E_M}{k \cdot T_{a.a.}}\right) \cdot \exp\left(-\frac{E_F}{k \cdot T_{s.t.}}\right) \quad (2.8)$$

For energetic reasons, di-vacancies are additionally present in aluminum at equilibrium conditions [39]. During quenching, the vacancy concentration is reduced due to annihilation at dislocations, which appear due to quenching tensions [40]. Thus, the equilibrium concentration of mono-vacancies in equation (2.8) is a simplification, but still very useful for a discussion of principles. It should also be noted that the diffusion is assisted by migration of di-vacancies [41] or by vacancy interactions with solute atoms [42], factors which are also neglected in equation (2.8). To investigate the effect of natural pre-aging on artificial aging it is crucial to discuss the behavior of quenched-in vacancies immediately after quenching. Due to differences in size and electronic structure between matrix and solute atoms, attractive interactions of about 0.1 eV among vacancies and solute atoms exist in many cases [39]. An association tendency of vacancies with Mg atoms during natural aging was shown by positron annihilation

lifetime spectroscopy (PALS) [42-44]. The growth of clusters during natural aging can be described by the model of Zurob and Seyedrezai [42,45]. Their theory assumes that vacancies need to escape from clusters, this being the rate-limiting step of natural aging. According to their model, all vacancies are bound in clusters at the end of natural aging [45].

In the present work isochronal resistivity curves were used to analyze co-cluster stability during artificial aging according to B2 and for a comparison of B2 and B0. Panseri *et al.* [28] found that small clusters generate an anomalous increase in resistivity, with a maximum at approximately 1 nm cluster radius. This is due to increased electron scattering [46], which depends on the size, composition and especially on the number density of clusters [47]. In natural aging of Al-Mg-Si alloys a huge anomalous increase in resistivity associated with co-cluster formation was observed [13,27]. Hence, a positive $\Delta\rho$ in figure 2.6 could be attributed to small clusters, whereby a decrease in resistivity is mainly caused by the dissolution of small clusters, the evolution of other larger precipitates and solute depletion [27]. For artificial aging which avoids natural pre-aging (B0) the slightly positive $\Delta\rho$ observed at low temperatures might be caused by GP-I zones, as found under comparable conditions [3]. They are larger and not so densely distributed as co-clusters, which accords well with the considerable difference in resistivity for B0 and B2 at 150 °C (note that at 150°C the same hardness for all heat treatment procedures was achieved (figure 2.5)). Rising temperature decreased the resistivity caused by B0, probably due to solute depletion and a lower contribution of precipitates. At 250 °C B2 and B0 showed the smallest deviation because the metastable solvus boundary might nearly be reached for both and the contribution of larger precipitation is small. When lowering the artificial aging temperature, the resistivity of B2 after 1.8 ks is determined by a total or partial dissolution of co-clusters, evolution of GP-I zones and solute depletion. Due to the still extant huge anomalous increase in resistivity, it can be deduced from figure 2.6 that co-clusters formed during natural preaging are prominently present after subsequent artificial aging for 1.8 ks below 180 °C.

This is supported by the results of atom probe tomography analysis. For long-term natural aging ($1.2 \cdot 10^6$ s) according to heat treatment procedure B2, small solute enriched regions associated with co-clusters were identified (figure 2.7a). Their number density was not significantly changed by one hour of subsequent artificial aging at 170 °C (figure 2.7b). For eight hours the number density of these solute enriched regions was about 40 % lower, but they were still present (figure 2.7c). Therefore it can be concluded that quenched-in vacancies which are bound with co-clusters and therefore caged in a 'prison' of solute atoms cannot assist diffusion at common artificial aging temperatures for B2. To be activated they need to be released by dissolution of the co-clusters. The dissolution of co-clusters is accelerated with rising artificial aging temperature according to equation (2.4), controlled by an activation energy

for dissolution of 0.79 eV (revealed in the temperature range between 190 to 250 °C). From figure 2.4 it can be seen that the kinetics of procedure B2 is getting faster with increasing reversion, which can be attributed to co-cluster dissolution involving vacancy release. This is approved by the higher temperature dependence of the rate constant caused by natural pre-aging compared to that of aging procedures A or B1 (figure 2.10). Apparently, co-cluster dissolution is equivalent to vacancy formation and determines the concentration of mobile vacancies in the matrix ($c_{v,mobil}^a$) and thus controls diffusion during aging according to equation (2.9). Edwards *et al.* [1] speculated that the transition from co-clusters to GPI zones might be associated with ordering and the release of vacancies. This possibly occurs in our experiments at low artificial aging temperatures. The fact that immobile vacancies can be mobilized by plastic deformation and this, in turn, can accelerate precipitation reactions was already reported by Kelly and Nicholson [38].

$$D \propto A \cdot \exp\left(-\frac{E_M}{k \cdot T_{a.a.}}\right) \cdot c_{v,mobil}^a \quad (2.9)$$

Panseri *et al.* [48,49] found that the annihilation of quenched-in vacancies is prevented by small additions of Mg in aluminum at room temperature and delayed at temperatures above 100 °C. It is thought that vacancy-solute clustering during natural aging can ‘temporarily stabilize’ vacancies at high artificial aging temperatures and slow annihilation processes. It can be assumed that the lifetime of a vacancy is enhanced if it is located in a region with a higher Mg concentration, because a jump from energetically favored positions next to Mg atoms into the matrix is less likely than a jump inside the matrix [45]. Hence the probability of a vacancy jump depends on the number of surrounding Mg atoms, and the vacancy lifetime is supposed to be a function of cluster size. For artificial aging of long-term naturally preaged material at high temperatures vacancies may be temporarily stabilized if they are associated with dissolving co-clusters (vacancy prisons). Recently, Barnhart *et al.* [50] reported that there is strong evidence from PALS that Mg and Si form vacancy-solute complexes within the first few minutes of natural aging. Further, Vaumousse *et al.* [51] found small clusters of an Al-Mg-Si-Cu alloy in the as-quenched state. Therefore it is likely that short-term natural pre-aging can also influence the mobility of vacancies and might temporarily stabilize them at high artificial aging temperatures.

2.5.2 Mechanisms controlling artificial aging in dependence on heat treatment procedure and aging temperature

2.5.2.1 Artificial aging at common temperatures

For direct artificial aging (A) at common temperatures a high initial concentration of mobile quenched-in vacancies is assumed. In addition, a huge solute super-saturation results in a strong driving force and a small critical nucleation size [23]. Both generate enhanced precipitation kinetics and can explain the rapid hardness increase found (figure 2.4a). A further consequence of the quenched-in vacancy-enhanced diffusion and the low energy barrier for nucleation is an increased nucleation rate for procedure A, which accords well with the observed high number density of β'' (figure 2.7d). The fundamental role of quenched-in vacancies is supported by Esmacili *et al.* [47], who already suggested that the migration of solute atoms assisted by quenched-in vacancies controls the early stage decomposition for AA 6111 in the range of 60 to 180 °C.

Hardness evolution (figure 2.4a) and precipitation kinetics (figure 2.10) caused by heat treatment procedure B1 differ insignificantly from A at common artificial aging temperatures, whereby both are assumed to be controlled by the same mechanisms.

For heat treatment procedure B2 co-clusters are supposed to act as ‘vacancy prisons’ at common artificial aging temperatures. Hence, a low initial concentration of mobile quenched-in vacancies in the matrix can be assumed. Natural aging also causes a reduction of solute super-saturation, or a rise in the critical nucleation size [23]. However, co-clusters are too small to act as nucleation sites for β'' [24]. The above-mentioned effects cause retarded precipitation kinetics and can explain the observed slow hardness evolution for B2 at common artificial aging temperatures (figure 2.4a). A further consequence of the small concentration of mobile quenched-in vacancies and the decreased solute super-saturation is a reduced nucleation rate. This is in accordance with the observed low number density of β'' precipitates (figure 2.7c) for artificial aging under industrially common conditions (28.8 ks at 170 °C), which finally causes the lower hardness of B2 compared to A or B1.

2.5.2.2 Artificial aging at high temperatures

There are some possible reasons for the observed stagnation of the rate constant (figure 2.10) and the deviation from the Arrhenius relationship (figure 2.11a) above 210 °C for direct aging (A). One is the decreasing driving force due to an increasing solubility and therefore lower solute super-saturation at higher temperatures. Evidence for this not being the controlling mechanism is that B2 shows no stagnation of the rate constant (figure 2.10), although the temperature dependence of the metastable solvus line should be equal for A and B2 (see

introduction of section 5). Another reason for the stagnation of the rate constant could be a more pronounced annihilation of quenched-in vacancies at higher temperatures. This is supported by an observation of Kelly and Nicholson [38]; they report on a reduced clustering rate at low temperatures after a short interruption of quenching at 200 °C and attribute this effect to annihilation of quenched-in vacancies. The influence of the moderately decreasing quenching rate for procedure A (225 °C/s to 160 °C/s) on kinetics is assumed to be negligible, because B1 (constant quenching rate of 900 °C/s), showed a similar behavior at elevated artificial aging temperatures (figure 2.10).

Compared to A hardness curves for procedure B1 were slightly shifted to higher values at increased artificial aging temperatures (figure 2.4c). Although a full explanation of this minor effect cannot be provided in this work two possible explanations are mentioned: i) The applied quenching rates of A and B1 are very high and should not directly influence the hardness by significant solute depletion at grain boundaries during quenching [2,52,53]. However, the higher quenching rate of B1 may reduce the nucleation of grain boundary precipitates during quenching, which will cause a lower amount of non-hardening grain boundary precipitates to evolve during high temperature artificial aging, and thus result in higher hardness values. ii) Short-term natural pre-aging may reduce grain boundary precipitation and the formation of precipitation free zones, which are caused by vacancy and/or solute depletion [54] during high-temperature artificial aging, due to a reduced mobility of vacancies (described in section 5.1). The lower hardness values for procedure A might therefore be caused by the presence of non-hardening grain boundary precipitates and precipitation free zones, which can reduce the strength as reported for precipitation-strengthened superalloys [55,56].

For procedure B2 no stagnation of the rate constant at high temperatures was observed (figure 2.10). As described in section 5.1, vacancies are supposed to be released from dissolving co-clusters and to accelerate precipitation kinetics. The suggestion that thermally-activated vacancy release controls the kinetics of B2 is supported by the fact that a linear Arrhenius relationship was found between 190 and 250 °C (figure 2.11c), although the solute super-saturation decreases. The higher revealed apparent activation energy related to the precipitation process of B2 compared to A or B1 may be caused by the dissolution of co-clusters, which must be overcome to release vacancies. Hence the positive influence of long-term natural aging on artificial aging above 210 °C (figure 2.4c) can be explained by an enhanced nucleation rate caused by vacancies, which are temporarily stabilized and released during co-cluster dissolution.

2.6 Conclusions

The objective of this study was to shed more light on the mechanisms which control artificial aging of Al-Mg-Si alloys over a wide temperature range and taking into account various thermal histories.

- In the case of direct artificial aging, mobile quenched-in vacancies and the solute supersaturation control precipitation reactions at common temperatures (e.g. 170 °C). At higher artificial aging temperatures (> 210 °C), besides the decreasing solute supersaturation the annihilation of vacancies becomes the predominant rate-controlling process step.
- The proposed ‘vacancy-prison mechanism’ provides a very satisfactory explanation for the known detrimental effect of natural pre-aging for common artificial aging temperatures, and the discovered positive influence of natural pre-aging at high artificial aging temperatures. Vacancy-rich co-clusters act as ‘vacancy prisons’ during artificial aging with a temperature dependent release behavior, resulting in slow precipitation kinetics at low temperatures but an enhanced nucleation rate at high temperatures.
- Over all artificial aging of Al-Mg-Si alloys was found to be mainly controlled by the concentration of mobile vacancies.

References

- [1] Edwards GA, Stiller K, Dunlop GL, Couper MJ. *Acta Mater* 1998;46:3893.
- [2] Ostermann F. *Anwendungstechnologie Aluminium*. Berlin Heidelberg New York: Springer-Verlag; 2007.
- [3] Marioara CD, Anderson SJ, Jansen JE, Zandbergen HW. *Acta Mater* 2003;51:789.
- [4] van Huis MA, Chen JH, Sluiter MHF, Zandbergen HW. *Acta Mater* 2007;55:2183.
- [5] Andersen SJ, Zandbergen HW, Jansen JE, Tacholt C, Tundal U, Reiso O. *Acta Mater* 1998;46:3283.
- [6] Buha J, Lumley RN, Crosky AG, Hono K. *Acta Mater* 2007;55:3015.
- [7] van Huis MA, Chen JH, Zandbergen HW, Sluiter MHF. *Acta Mater* 2006;54:2945.
- [8] Vissers R, van Huis MA, Jansen J, Zandbergen HW, Marioara CD, Andersen SJ. *Acta Mater* 2007;55:3815.

- [9] Massardier V, Epicier T, Merle P. *Acta Mater* 2000;48:2911.
- [10] Ravi C, Wolverton C. *Acta Mater* 2004;52:4213.
- [11] Haase C, Wurts H. *Z Metall* 1941;33:399.
- [12] Ried A, Schwellinger P, Bichsel H. *Aluminium* 1977;53:595.
- [13] Kovács I, Nagy E, Lendvai J. *Acta Metall* 1972;20:975.
- [14] Dorward RC. *Metall Trans* 1973;4:507.
- [15] Borchers H, Kainz M. *Metall* 1963;17:400.
- [16] Chang CST, Wieler I, Wanderka N, Banhart J. *Ultramicroscopy* 2009;109:585.
- [17] Zhuang L, Janse JE, De Smet P, Chen JH, Zandbergen HW. In: Das SK, Kaufman JG, Lienert TJ, editors. *Aluminum 2001*. Warrendale (PA): TMS; 2001. p. 77.
- [18] Røyset J, Stene T, Saeter JA, Reiso O. *Mater Sci Forum* 2006;519-521:239.
- [19] Bryant JD. *Metall Mater Trans A* 1999;30:1999.
- [20] Saga M, Sasaki Y, Kikuchi M, Yan Z, Matsuo M. *Aluminium Alloys: Their Physical and Mechanical Properties* 1996;217:821.
- [21] Slámová M, Janecek M, Cieslar M, Šíma V. *Mater Sci Forum* 2007;567-568:333.
- [22] Ou BL, Shen CH. *Scand J Metall* 2005;34:318.
- [23] Huppert-Schemme G. *AlMgSi-Bleche für den Fahrzeugbau – Metallkunde und Fertigungstechnik*. Düsseldorf: Aluminium-Verlag; 1997.
- [24] Murayama M, Hono K, Saga M, Kikuchi M. *Mater Sci Eng A* 1998;250:127.
- [25] Suzuki H, Kanno M, Itoh G. *Aluminium* 1981;57:628.
- [26] Murayama M, Hono K. *Acta Mater* 1999;47:1537.
- [27] Esmaili S, Lloyd DJ, Poole WJ. *Mater Lett* 2005;59:575.
- [28] Panseri C, Federighi T. *J Inst Met* 1966;94:99.
- [29] Miller MK, Cerezo A, Hetherington MG, Smith GDW. *Atom Probe Field Ion Microscopy*. Oxford: Oxford University Press; 1996.
- [30] Hellman OC, du Rivage JB, Seidman DN. *Ultramicroscopy* 2003;95:199.
- [31] Hellman OC, Vandenbroucke JA, Rusing J, Isheim D, Seidman DN. *Microsc Microanal* 2000;6:437.
- [32] Yoon KE, Noebe RD, Hellman OC, Seidman DN. *Surf Inter Anal* 2004;36:594.
- [33] Hasting HK, Lefebvre W, Marioara C, Walmsley JC, Andersen S, Holmestad R, Danoix F. *Surf Inter Anal* 2007;39:189.
- [34] Esmaili S, Lloyd DJ, Poole WJ. *Acta Mater* 2003;51:2243.
- [35] Shercliff HR, Ashby MF. *Acta Metall Mater* 1990;38:1789.
- [36] Esmaili S, Lloyd DJ, Poole WJ. *Acta Mater* 2003;51:3467.
- [37] Ber LB. *Mater Sci Eng A* 2000;280:91.
- [38] Kelly A, Nicholson RB. *Prog Mater Sci* 1963;10:149.

- [39] Haasen P. *Physikalische Metallkunde*. Berlin Heidelberg New York Tokyo: Springer-Verlag; 1984.
- [40] Panseri C, Federighi T. *Acta Metall* 1960;8:217.
- [41] Altenpohl D. *Aluminium* 1961;37:401.
- [42] Seyedrezai H, Grebennikov D, Mascher P, Zurob HS. *Mater Sci Eng A* 2009;525:186.
- [43] Dupasquier A, Kögel G, Somoza A. *Acta Mater* 2004;52:4707.
- [44] Buha J, Muramatsu T, Lumley RN, Crosky AG, Hillel AJ. *Mater Forum* 2004;28:1028.
- [45] Zurob HS, Seyedrezai H. *Scr Mater* 2009;61:141.
- [46] Hillel AJ, Rossiter PL. *Phil Mag B* 1981;44:383.
- [47] Esmaili S, Vaumousse D, Zandbergen MW, Poole WJ, Cerezo A, Lloyd DJ. *Phil Mag* 2007;87:3797.
- [48] Panseri C, Federighi T, Ceresara S. *Trans Metall Soc AIME* 1963;227:1122.
- [49] Panseri C, Gatto FG, Federighi T. *Acta Metall* 1958;6:198.
- [50] Banhart J, Chang CST, Liang ZQ, Wanderka N, Lay MDH, Hill AJ. *Advanced Engineering Materials* 2010;12:559.
- [51] Vaumousse D, Cerezo A, Warren PJ, Court SA. *Mater Sci Forum* 2002;396-402:693.
- [52] Steele D, Evans D, Nolan P, Lloyd DJ. *Mater Charct* 2007;58:40.
- [53] Esmaili S, Poole WJ, Lloyd DJ. *Mater Sci Forum* 2000;331-337:995.
- [54] Porter DA, Easterling KE. *Phase Transformations in Metals and Alloys*. London Weinheim New York Tokyo Melbourne Madras: Chapman & Hall; 1992.
- [55] Krol T, Baither D, Nembach E. *Acta Mater* 2004;52:2095.
- [56] Krol T, Baither D, Nembach E. *Scr Mater* 2003;48:1189.

3 THE β'' PHASE

This chapter focuses on the controversy concerning the structure and chemical composition of precipitates formed in Al-Mg-Si alloys mentioned in the introduction section. The β'' phase present in the alloy AA6061 induced by two artificial aging strategies is studied in detail by a comparative approach using atom probe tomography and transmission electron microscopy. The “vacancy-prison mechanism” presented in chapter 2 is used to describe its genesis.

The two basic T6 microstructures of AA6061*

In this study the T6 microstructure of the aluminum alloy AA6061 was investigated by atom probe tomography and transmission electron microscopy. Direct artificial aging induced a mono-modal size distribution of β'' precipitates, while for artificial aging after long-term natural pre-aging a bimodal size distribution was found. This difference can be explained by the impact of lattice defects on the β'' -nucleation. In AA6061 β'' is supposed to contain Al and exhibits a Mg/Si ratio higher than the expected Mg_5Si_6 stoichiometry.

3.1 Introduction

For the well-known aluminum alloy AA6061 a strong adverse influence of natural pre-aging on kinetics and T6 strength has been reported [1-4]. This phenomenon, occurring in the rich Al-Mg-Si alloys, is commonly called ‘negative effect’ and has been linked to a coarser distribution of precipitates than that formed by direct artificial aging [4,5]. The simplified precipitation sequence of AA6061 [6] can be described as SSSS \rightarrow Clustering stage \rightarrow Mg,Si co-clusters \rightarrow GP-I zones ‘a. o.’ \rightarrow β'' ‘a. o.’ \rightarrow B’, β' ‘a. o.’ \rightarrow β -Mg₂Si. ‘a. o.’ refers to ‘and others’, and indicates that various other precipitates [7] have been reported in addition to the most common ones named above. The early stages of aging resulting in the formation of Mg,Si co-clusters [8] take place in several individual steps which are not yet clearly distinguished [9]. Today, atom probe tomography (APT) is the only technique for visualizing such small clusters [10], but even this method operates at its limit for this purpose. The earliest precipitates in the sequence which produce a distinct contrast for transmission electron microscopy (TEM) identification are spherical GP-I zones [11]. GP-I zones are thought to transform to β'' [12], and the already needle-like pre- β'' phase [13] has therefore been described as the most developed GP-I zone. β'' needles [14,15] are the typical precipitates under T6 conditions in AA6061 [6]. They have a base-centered monoclinic structure and are aligned along $\langle 100 \rangle_{Al}$, being fully coherent only along the needle-axis. Although the chemical composition of the β'' phase has been proposed as Mg_5Si_6 [14,15], it has become clearer in the past few years that the exact composition of β'' seems to be strongly influenced by the composition of the studied alloy [16-18]. For overaged conditions, the rod-shaped phases β' [19], B’ [20], and a large number of other lath or rod-shaped phases have been reported [7]. A close look at the T6 microstructure variants of AA6061 resulting from T6 treatment realized either by direct

*Pogatscher S, Antrekowitsch H, Leitner H, Sologubenko AS, Uggowitzer PJ. Acta Mater 2012. Submitted

artificial aging or artificial aging after long-term natural pre-aging reveals significant differences in the shape and population of the precipitates. In this paper we call this phenomenon ‘the two basic T6 microstructures’, and explain its genesis by means of the “vacancy-prison mechanism” recently described in [4].

3.2 Experimental methods

The studied alloy AA6061 (Mg 0.92, Si 0.58, Cu 0.09, Fe 0.25, Cr 0.08, Mn 0.05 Zn 0.03 and Ti 0.05, all in at.%) was provided by AMAG Rolling in the form of wrought plate. Solution heat treatment was conducted in a circulating air furnace at 570 °C for 1.2 ks. Direct artificial aging and artificial aging after long-term natural pre-aging of $1.2 \cdot 10^6$ s after quenching was performed at 170 °C for $2.88 \cdot 10^4$ s (common industrial conditions for reaching T6) according to the time-temperature sequences described in figure 3.1.

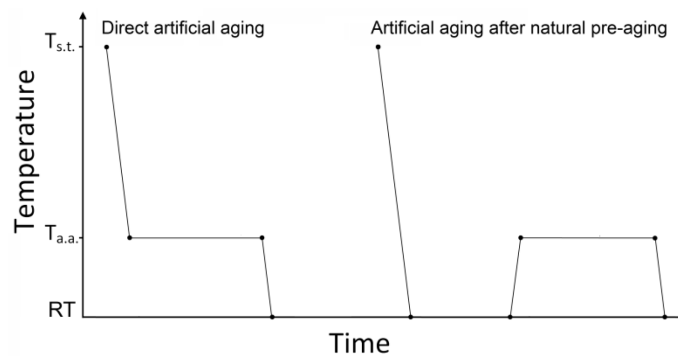


Figure 3.1: Schematic representation of the heat treatment procedure

Needle-shaped specimens for APT were prepared via a standard two-step method [21]. APT was performed on a LEAP™ 3000 X HR atom probe at a temperature of -238 °C with a pulse fraction of 15 % under ultra-high vacuum ($< 10^{-10}$ mbar). The reconstruction procedure and analysis were conducted using the software package IVAS 3.6.0™ from CAMECA.

TEM specimens were prepared by the standard route of grinding, dimpling and finally electrolytic polishing as described in [6]. Conventional TEM (CTEM), high resolution TEM (HRTEM) and scanning TEM (STEM) studies were performed on an FEI Tecnai F30 machine operated at 300 kV.

3.3 Results and discussion

3.3.1 Atom probe tomography

Figure 3.2 shows three-dimensional (3D) reconstructions of the atom positions for Mg, Si and Cu, and isoconcentration surfaces of Mg embedded in the Al matrix for the two T6 microstructure variants. It is obvious that the distributions of Mg, Si and Cu differ for direct artificial aging and artificial aging after long-term natural pre-aging. To visualize the precipitation microstructure more clearly, isoconcentration surfaces, with an arbitrary threshold value of 2.8 at.% Mg, which is three times higher than the average Mg concentration of the alloy, were used. A separation between individual precipitates was made according to their morphology and composition. Direct artificial aging (figure 3.2a) revealed a dense mono-modal distribution of short needles oriented in three directions perpendicular to each other with a high number density ($2.9 \cdot 10^{23} \text{ m}^{-3}$). In addition, smaller iso-surfaces, which might include GP-I zones and few co-clusters [4], are present. Artificial aging after long-term natural pre-aging (figure 3.2b) revealed two morphologies of needles oriented in three perpendicular directions. Beside short needles ($0.8 \cdot 10^{23} \text{ m}^{-3}$), long needles with a much higher aspect ratio were found in a low number density ($\sim 0.1 \cdot 10^{23} \text{ m}^{-3}$). Moreover, smaller and nearly spherical iso-surfaces, very likely indicating co-clusters, and a few GP-I zones are present [4].

Proxigrams [22,23] based on the iso-surfaces shown in figure 3.2 were used to compare the chemical composition of various needle-like precipitates. The core composition of short needles observed after direct artificial aging was found to be 34 ± 3.3 at.% Al, 3.3 ± 1.8 at.% Cu, 37 ± 3.4 at. % Mg and 26 ± 3.0 at.% Si (figure 3.3a). Short needles induced by artificial aging after long-term natural pre-aging revealed 29 ± 3.0 at.% Al, 2.6 ± 1.0 at.% Cu, 41 ± 3.3 at.% Mg and 27 ± 3.0 at.% Si (figure 3.3b). The long needles exhibited a composition of 26 ± 3.0 at.% Al, 2.0 ± 0.9 at.% Cu, 44 ± 3.1 at.% Mg and 27 ± 2.8 at.% Si (figure 3.3c) in the core. A comparison of the proximity histograms revealed no distinct discrepancy for the individual needles studied. The average solute concentration seems to be slightly higher in the short and long needles generated by artificial aging after long-term natural pre-aging than that observed in the short needles produced by direct artificial aging, but the differences are not significant. A cluster search algorithm based on the maximum separation method taking into account Mg, Si and Cu as involved solutes was also utilized [24]. The separation distance (d_{max}), surround distance (L) and erosion distance (d_{ero}) were determined based on the method described in [25] and were set to 0.48. Note that all numbers of atoms discussed are the detected values of atoms and do not take the detection efficiency (36 %) into account.

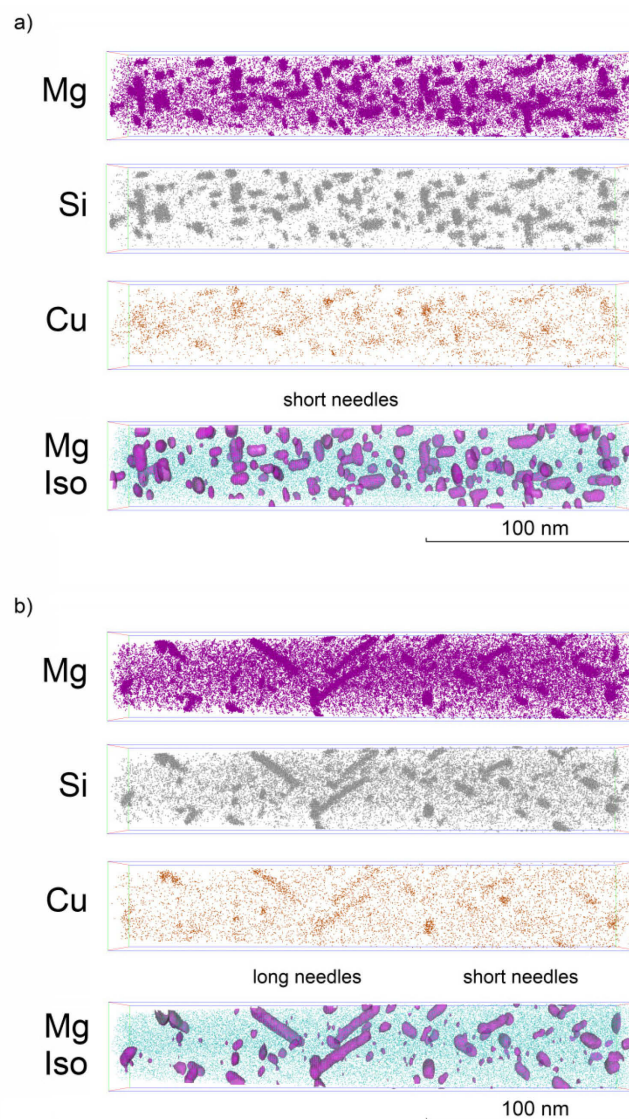
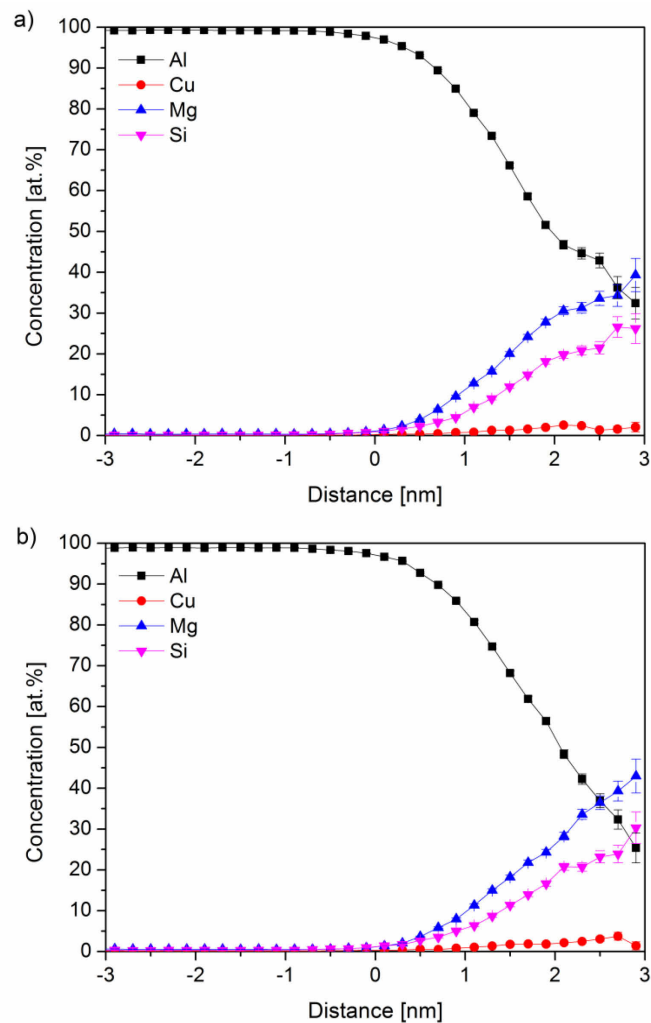


Figure 3.2: Three-dimensional (3D) reconstructions of the atom positions for Mg, Si and Cu and isoconcentration surfaces of Mg embedded in the Al matrix for (a) direct artificial aging and (b) artificial aging after long-term natural pre-aging (all in T6 condition)

For direct artificial aging, 61 needle-like clusters, each containing more than 250 detected solute atoms (505 ± 234 solute atoms on average), were analyzed. An average concentration of 45 ± 5.1 at.% Al, 2.4 ± 0.9 at.% Cu, 32 ± 3.3 at.% Mg and 20 ± 2.4 at.% Si and a Mg/Si ratio of 1.6 ± 0.2 was found. For artificial aging after long-term natural pre-aging, 19 clusters that contained more than 250 but fewer than 1350 solute atoms (671 ± 308 solute atoms on average) were analyzed (non-needle-like precipitates and long needles were not considered). An average concentration of 44 ± 4.9 at.% Al, 2.8 ± 0.8 at.% Cu, 32 ± 2.9 at.% Mg and 21 ± 2.3 at.% Si and a Mg/Si ratio of 1.5 ± 0.2 was evaluated. The average number of solute atoms contained in long needles was found to be 2672 ± 579 , although this value may actually be higher because some were cut by the surface of the analyzed volume. The 3 long needles studied revealed an average

concentration of around 43 ± 4.0 at.% Al, 2.3 ± 0.7 at.% Cu, 33 ± 3.2 at.% Mg and 21 ± 1.9 at.% Si and a Mg/Si ratio of 1.6 ± 0.2 . Because the cluster search includes the shell of the studied precipitates it revealed a higher Al content compared to the core composition deduced from the proxigrams. However, it showed no significant differences between the needles occurring during the two thermal histories. Numerous previous studies described needles occurring in peak aged conditions in AA6061 as β'' [6,11]. Obviously the Mg/Si ratio of all observed needles is higher than expected for β'' precipitates with Mg_5Si_6 stoichiometry [14,15]. Nevertheless, our results are consistent with other APT studies on AA6061 [18] and balanced Al-Mg₂Si alloys [8,26], which reported even higher Mg/Si ratios for β'' . In addition, a significant Al content in the needles investigated was observed. This is consistent with the findings of Hasting *et al.* [16], who claimed that $Mg_5Al_2Si_4$ [17] may be energetically more beneficial than Mg_5Si_6 , but that the exact composition depends on the alloy composition.



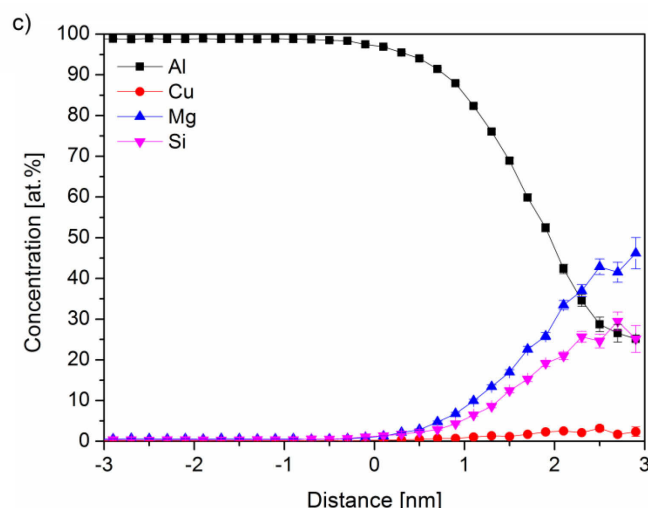


Figure 3.3: Proximity histograms for Al, Mg, Si, and Cu, based on (a) short needles found after direct artificial aging and (b) short or (c) long needles induced by artificial aging after long-term natural pre-aging (all in T6 condition)

3.3.2 Transmission electron microscopy

To confirm the results from APT, the T6 microstructures were studied by TEM. In figure 3.4a, a HAADF (high angle annular dark field) STEM image acquired in the $[100]_{\text{Al}}$ zone axis from the specimen subjected to direct artificial aging shows randomly distributed short needles that range between 7 nm and 13 nm in length. To distinguish the needle-like from the spherical precipitates, the same area of the specimen was also studied in other zone axis orientations, revealing the presence of spherical precipitates in the matrix. The observed T6 microstructure accords well with the results of APT. Both TEM and APT revealed a mono-modal size distribution of short needles after direct artificial aging. Figure 3.4b shows the microstructure induced by artificial aging after long-term natural pre-aging. Beside some spherical precipitates and short needles (7 nm to 17 nm), few long needles (37 nm to 48 nm) with a much higher aspect ratio aligned along $\langle 100 \rangle_{\text{Al}}$ were observed, perfectly supporting the results from APT. The contrast in images does not reveal any detectable differences between long and short needles formed by artificial aging after long-term natural pre-aging (figure 3.4b). Note that the brighter appearance of short needles in figure 3.4a in comparison to figure 3.4b results from the greater thickness of the sample area and not the nature of the needles. A bright field (BF) TEM image acquired in the $[110]_{\text{Al}}$ zone axis from a specimen subjected to artificial aging after long-term natural pre-aging is presented in figure 3.4c and shows needles aligned along $[100]_{\text{Al}}$ which are accumulated at a dislocation line. These needle-like particles were found to be the same size as the long needles presented in figure 3.4b.

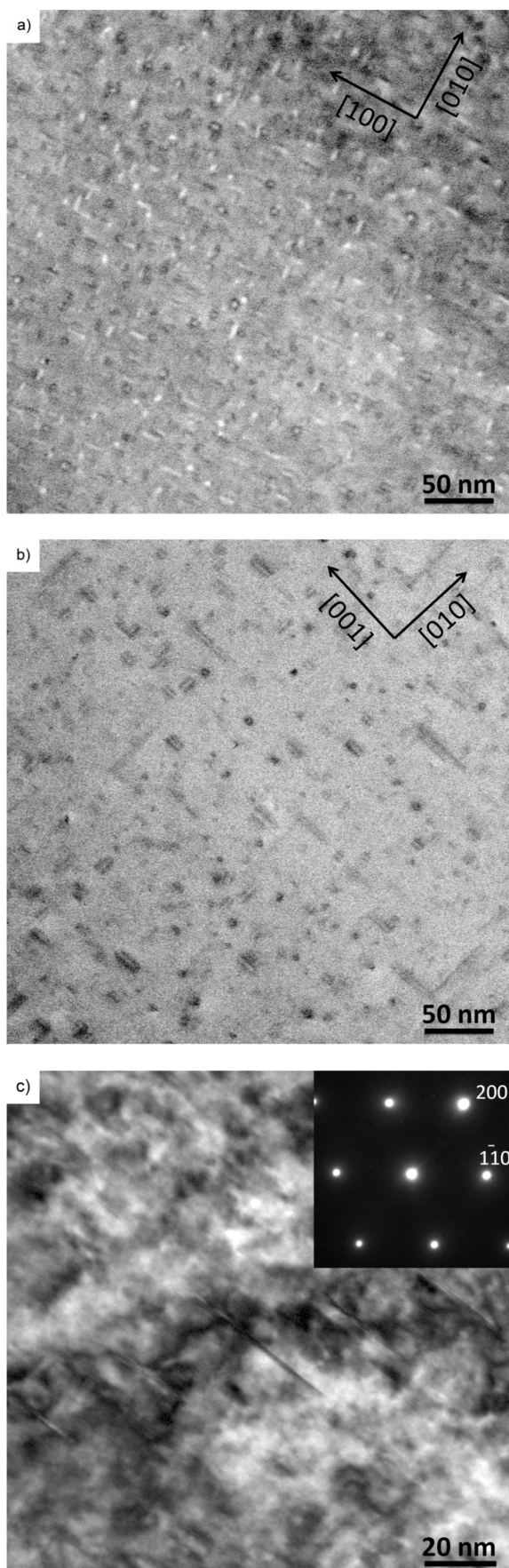


Figure 3.4: HAADF STEM images taken in the $[100]_{\text{Al}}$ zone axis for specimens subjected to (a) direct artificial aging and (b) artificial aging after long-term natural pre-aging. (c) BF image acquired in the $[110]_{\text{Al}}$ zone axis for a material artificially aged after long-term natural pre-aging (all in T6 condition)

The structures of the needles formed upon direct artificial aging and artificial aging after long-term natural aging were studied by HRTEM and corresponding FFTs (Fast Fourier Transform). A number of FFT patterns acquired from HRTEM image areas with needles were analyzed. No indications for a high degree of chemical order corresponding to the Mg_5Si_6 composition of the β'' phase were found. However, it is important to note that HRTEM image analysis and TEM techniques in general are normally not considered as reliable methods for the evaluation of the extend of the chemical order since the electron scattering intensity modulations in DP's or FFTs are strongly influenced by a number of effects, i.e. thickness of the illuminated area, deviation from the zone axis, lattice strain, etc. Nevertheless, the FFT analyses revealed the monoclinic crystal structure of the β'' phase described by Zandbergen *et al.* [15] or Edwards *et al.* [6] for the analyzed particles. Note that no structures other than this could be deduced from the FFTs, although a few blurred patterns were unidentifiable. In figure 3.5a, an HRTEM image of such a particle (framed) is presented with a corresponding FFT in the insert. The analysis of the FFT fits the monoclinic structure of β'' phase exhibiting an orientation relationship $(010)_{\beta''} // (001)_{\text{Al}}$; $[001]_{\beta''} // [1\bar{3}0]_{\text{Al}}$; $[100]_{\beta''} // [320]_{\text{Al}}$ [27]. The FFT analysis of the images of the needles in specimens subjected to artificial aging after long-term natural pre-aging showed similar results. Because it is not possible to distinguish between long and short needles by studying needle cross-sections, the HRTEM images acquired in the $[100]_{\text{Al}}$ zone axis from needles lying parallel to the image plane were analyzed. In figure 3.5b a long needle (45 nm in length) is indicated by arrows. The FFT pattern of the marked area revealed good coincidence with the β'' phase exhibiting an orientation relationships $(010)_{\beta''} // (100)_{\text{Al}}$; $[001]_{\beta''} // [031]_{\text{Al}}$; $[100]_{\beta''} // [0\bar{2}3]_{\text{Al}}$ or $(010)_{\beta''} // (\bar{1}00)_{\text{Al}}$; $[001]_{\beta''} // [03\bar{1}]_{\text{Al}}$; $[100]_{\beta''} // [023]_{\text{Al}}$ [27].

It is very likely that short needles formed upon direct artificial aging and both morphologies of needles (short and long) generated by artificial aging after long-term natural pre-aging are two variants of the same β'' phase. Taking the results from atom probe tomography and the findings of Hasting *et al.* [17] into consideration, we conclude that the β'' found in the studied AA6061 alloy may not necessarily be of Mg_5Si_6 composition: note that according to our results the β'' phase exhibits a significant amount of Al and a higher Mg/Si ratio. Probably it is chemically ordered to a lesser extent, as was already reported for Al-Mg-Si alloys rich in Mg [28]. This is certainly not unlikely if we consider the very high Mg/Si ratio present in the matrix after the solution treatment (≈ 2.9 ; calculated by the thermodynamic software FactSage™ 6.2 [29] and the FACT FTlite light alloy database (2009)).

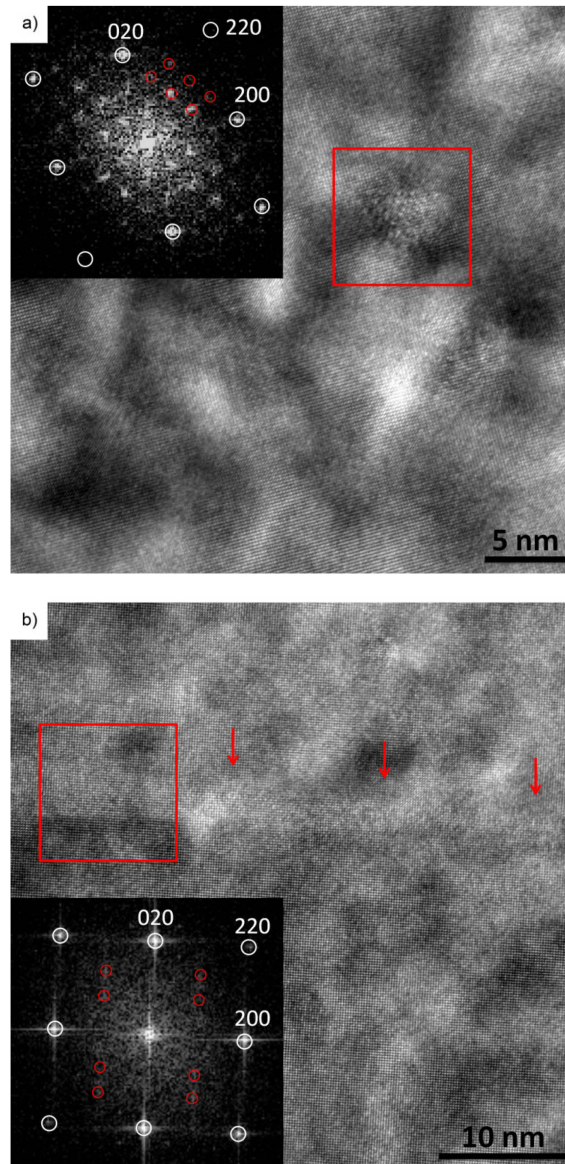


Figure 3.5: HRTEM images taken in the $[100]_{Al}$ zone axis with the FFT of the framed areas in the inserts for specimens subjected to (a) direct artificial aging and (b) artificial aging after long-term natural pre-aging (all in T6 condition)

The differences in the morphologies of the β'' precipitates for both thermal treatment paths can be explained by considering the impact of lattice defects on the nucleation process during artificial aging. It is known that quenched-in vacancies strongly enhance the nucleation of the β'' phase for direct artificial aging [4,30]. Therefore a dense and uniform distribution of β'' nuclei can be expected. Due to their high number density these grow to a relatively short length until the solute super saturation has been significantly reduced. Recently we showed that the negative effect of natural pre-aging is linked to a lack of mobile quenched-in vacancies after natural pre-aging (“vacancy-prison mechanism” [4]). A low concentration of mobile quenched-in vacancies hinders the nucleation of β'' [30]. We suggest that heterogeneous nucleation at the beginning of artificial aging gains in importance for the distribution of β'' after natural pre-

aging. Nucleation at dislocations, observed in figure 3.4c, might be a possible mechanism. In addition, the formation from very sparsely distributed Mg, Si co-clusters above the critical size of nuclei for β'' may play a role. Note that the majority of Mg,Si co-clusters formed by long-term natural pre-aging have been shown to be smaller than the critical size of nuclei for β'' [8], but a statistical size distribution might cover some above the critical size. Due to the coarse distribution of precipitates, a reduced overlapping of the diffusion fields and a high remaining solute super saturation enable heterogeneously nucleated β'' to grow to a great length. Generally, because of a lack of mobile quenched-in vacancies nucleation of β'' in the Al matrix takes much longer and results in few short needles, finally generating the observed bimodal distribution of β'' needles in AA6061 for artificial aging after long-term natural pre-aging.

3.4 Conclusions

In summary, the two basic T6 microstructure variants generated by direct artificial aging and artificial aging after natural pre-aging were studied for the alloy AA6061.

- Direct artificial aging caused the formation of a mono-modal size distribution of short, needle-like β'' precipitates.
- Upon artificial aging after long-term natural pre-aging, a bimodal size distribution of long and short β'' needles was seen.
- The β'' phase induced by both thermal treatments in AA6061 is believed to contain a significant amount of Al and shows a Mg/Si ratio higher than expected from the Mg_5Si_6 stoichiometry.
- The differing size distributions of β'' precipitates in both cases can be explained by the impact of lattice defects and the reduced availability of vacancies on their nucleation.

Acknowledgments

The authors wish to express their sincere thanks to the people at AMAG Rolling. We are also grateful to the Austrian Research Promotion Agency (FFG) and AMAG Rolling for their financial support of this work.

References

- [1] Brenner P, Kostron H. *Z Metall* 1939;4:89.
- [2] Borchers H, Kainz M. *Metall* 1963;17:400.
- [3] Ried A, Schwellinger P, Bichsel H. *Aluminium* 1977;53:595.
- [4] Pogatscher S, Antrekowitsch H, Leitner H, Ebner T, Uggowitzzer PJ. *Acta Mater* 2011;59:3352.
- [5] Buha J, Lumley RN, Crosky AG. *Metall Mater Trans A* 2006;37A:3119.
- [6] Edwards GA, Stiller K, Dunlop GL, Couper MJ. *Acta Mater* 1998;46:3893.
- [7] Ravi C, Wolverson C. *Acta Mater* 2004;52:4213.
- [8] Murayama M, Hono K. *Acta Mater* 1999;47:1537.
- [9] Banhart J, Lay MDH, Chang CST, Hill AJ. *Phys Rev B* 2011;83:014101.
- [10] Banhart J, Chang CST, Liang ZQ, Wanderka N, Lay MDH, Hill AJ. *Adv Eng Mater* 2010;12:559.
- [11] Buha J, Lumley RN, Crosky AG, Hono K. *Acta Mater* 2007;55:3015.
- [12] Marioara CD, Anderson SJ, Jansen JE, Zandbergen HW. *Acta Mater* 2003;51:789.
- [13] Marioara CD, Anderson SJ, Jansen J, Zandbergen HW. *Acta Mater* 2001;49:321.
- [14] Anderson SJ, Zandbergen HW, Jansen JE, Taeholt C, Tundal U, Reiso O. *Acta Mater* 1998;46:3283.
- [15] Zandbergen HW, Anderson SJ, Jansen J. *Science* 1997;277:1221.
- [16] Hasting HK, Lefebvre W, Marioara C, Walmsley JC, Anderson S, Holmestad R *et al.* *Surf Inter Anal* 2007;39:189.
- [17] Hasting HS, Frøseth AG, Anderson SJ, Vissers R, Walmsley JC, Marioara CD *et al.* *J Appl Phys* 2009;106:123527.
- [18] Buha J, Lumley RN, Crosky AG. *Phil Mag Lett* 2008;88:373.
- [19] Vissers R, van Huis MA, Jansen J, Zandbergen HW, Marioara CD, Anderson SJ. *Acta Mater* 2007;55:3815.
- [20] Dumolt SD, Laughlin DE, Williams JC. *Scr Metall Mater* 1984;18:1347.
- [21] Miller MK, Cerezo A, Hetherington MG, Smith GDW. *Atom Probe Field Ion Microscopy*. Oxford: Oxford University Press; 1996.
- [22] Hellman OC, Vandenbroucke JA, Rusing J, Isheim D, Seidman DN. *Microsc Microanal* 2000;6:437.
- [23] Yoon KE, Noebe RD, Hellman OC, Seidman DN. *Surf Inter Anal* 2004;36:594.
- [24] Cerezo A, Davin L. *Surf Inter Anal* 2007;39:184.
- [25] Vaumousse D, Cerezo A, Warren PJ. *Ultramicroscopy* 2003;95:215.
- [26] Murayama M, Hono K, Saga M, Kikuchi M. *Mater Sci Eng A* 1998;250:127.

- [27] Yang WC, Wang MP, Zhang RR, Zhang Q, Sheng XF. *Scr Mater* 2010;62:705.
- [28] Marioara CD, Anderson SJ, Zandbergen HW, Holmestad R. *Metall Mater Trans A* 2005;36:691.
- [29] Bale CW, Chartrand P, Degterov SA, Eriksson G, Hack K, Ben Mahfoud R *et al.* *Calphad* 2002;26:189.
- [30] Pogatscher S, Antrekowitsch H, Leitner H, Pöschmann D, Zhang Z, Uggowitzer PJ. *Acta Mater* (2012), <http://dx.doi.org/10.1016/j.actamat.2012.04.026>

4 NUCLEATION AND ITS USE

This chapter addresses the relationship between quenched-in vacancies and the nucleation of the β'' phase, considering different strategies of artificial aging, which results in further refinement of the model described in chapter 2. Furthermore, interrupted quenching (I.Q.) is presented as a new and beneficial heat treatment strategy for the alloy AA6061. The nucleation of β'' precipitates is discussed for this novel heat treatment in a wide temperature range considering vacancy-assisted nucleation in the matrix and nucleation at heterogeneous nucleation sites.

Influence of Interrupted Quenching on Artificial Aging of Al-Mg-Si Alloys*

In this study the influence of interrupted quenching (I.Q.) in a temperature range of 150-250 °C for periods of 15-1080 s on artificial aging after long-term natural pre-aging was studied for the Al-Mg-Si alloy AA6061 by atom probe tomography, transmission electron microscopy, electrical resistivity and hardness measurements, and differential scanning calorimetry. Compared with a standard quenching procedure, the results showed that hardening kinetics and the age hardening response were enhanced for I.Q. at low temperatures but reduced at high temperatures. Quenched-in vacancies were shown to be of particular importance for the nucleation of precipitates occurring during I.Q. at the lower end of the temperature range, finally leading to the formation of a dense distribution of β'' during artificial aging. For standard water quenching and subsequent natural aging nucleation is hindered by a low concentration of quenched-in vacancies in the matrix. I.Q. at high temperatures affects subsequent artificial aging via the formation of precipitates which do not contribute to hardening but consume a significant amount of solute.

4.1 Introduction

The aluminum alloy AA6061 is an important member of the Al-Mg-Si alloy family [1]. Although this group of age hardenable aluminum alloys is the most frequently used commercially [2], aging is not understood as deeply as for Al-Cu alloys or Al-Mg-Zn alloys due to its complexity and the limits of the available experimental methods [3]. The precipitation sequence, rather controversial in the early stages, is usually considered to occur as follows during linear heating [4]: SSSS \rightarrow Si-clusters and Mg-clusters \rightarrow dissolution of Mg-clusters \rightarrow Mg,Si-co-clusters \rightarrow GP-I zones \rightarrow β'' \rightarrow B' and β' \rightarrow β . After the first stages including individual solute clustering of Si and Mg and the dissolution of Mg-clusters, co-clusters are formed from the super-saturated solid solution (SSSS) [4]. Co-clusters [3-8] were also found after long-term room temperature exposure, whereby it should be mentioned that Banhart *et al.* recently reported that natural aging of Al-Mg-Si alloys is a rather complex process which takes place in several individual stages which are not yet fully resolved [2]. Since the notation of clusters is not consistent in literature (co-clusters are termed as both initial- β'' [9] and GP-zones [10]), in this paper the term co-cluster is only used for clusters formed after long-term natural aging. Consecutively formed GP-I zones [11-13] are thermally more stable, contain

*Pogatscher S, Antrekowitsch H, Leitner H, Pöschmann D, Zhang Z, Uggowitzer PJ. Acta Mater (2012), <http://dx.doi.org/10.1016/j.actamat.2012.04.026>

more solute atoms, and are generally found to be spherical, with a typical size of 1 to 3 nm [14]. Note that Marioara *et al.* [15] described the needle-like pre- β'' phase as the most developed GP-I zone, and in [16] GP-zones are generally described as fine plates. Due to the fact that the nomenclature 'GP-I zones' is still controversial, it is used in the current study for precipitates formed between co-clusters and the β'' -phase. The needle-like β'' (Mg_5Si_6) precipitates found at peak aged states are aligned along $\langle 100 \rangle_{Al}$, are monoclinic and are only fully coherent along the needle-axis [14,17]. Subsequently, the rod-shaped phases β' [18] and B' [19] are formed. These are hexagonal, aligned along $\langle 100 \rangle_{Al}$ and typical for overaged microstructures. The equilibrium phase β (Mg_2Si) is platelet-like and shows an f.c.c anti-fluorite structure [4,9,10,20]. For alloys rich in Mg and Si, such as AA6061, a strong adverse influence of natural pre-aging on subsequent artificial aging has been noted [21-24]. Even though this effect has been investigated for the last 70 years, it has not yet been fully resolved [3]. Recent results indicate that artificial aging kinetics of AA6061 is controlled via the concentration of mobile vacancies, which is determined by a temperature-dependent dissolution of co-clusters associated with the release of immobile quenched-in vacancies. Due to a very slow co-cluster dissolution at common artificial aging temperatures, the precipitation process is strongly retarded [25]. In addition, co-clusters are too small to act as nucleation sites for consecutively formed precipitates [12]. However, in most heat-treated semi-finished products, it is impossible to avoid prior natural aging for logistical reasons, meaning that energy efficiency, production capacity, profitability and achievable strength are reduced [1]. Moreover, over the last few years Al-Mg-Si alloys have been increasingly used for automotive outer panel applications, where a typical paint-bake cycle is much too short to reach T6 strength for naturally pre-aged Al-Mg-Si alloys. Hence, various heat treatments, in addition to quenching and artificial aging, to minimize the negative influence of intermediate room temperature storage have been investigated and patented. It is assumed that stable hypercritical GP-I zones [12] (due to the unsystematic nomenclature Mg,Si-clusters [6], clusters [26] and pre- β'' [27] are named in this context) formed during these extra heat treatments and act as nuclei for consecutively formed β'' -precipitates [12] or transform to β'' [27], and therefore enhance artificial aging. Most additional long-term heat treatments (pre-aging treatments) are performed immediately after quenching for several hours at temperatures around 100 °C [6,12,28,29]. Although some researchers have considered direct quenching to the pre-aging temperature [30], a systematic study of the effect of interrupted quenching (I.Q.) at temperatures above 100 °C on artificial aging after natural pre-aging is still pending. In most cases quenching has only been investigated concerning the effect of the quenching rate on the formation of grain boundary precipitation [31] and its adverse effect on mechanical properties [1] and fracture behavior [32], or regarding the effect of a quench interruption at high temperatures on intergranular corrosion

of Al-Mg-Si(Cu) alloys [33]. The present study was performed to determine the influence of I.Q. on precipitation reactions in Al-Mg-Si alloys over a wide temperature range from 150 to 250 °C, via a multi-method approach which included atom probe tomography, transmission electron microscopy, electrical resistivity and hardness measurements, and differential scanning calorimetry. Besides generally outlining the usability of I.Q. as a new and beneficial heat treatment strategy, fundamental aspects regarding the role of quenched-in vacancies in the nucleation of β'' are addressed and should help to shed more light on the influence of natural pre-aging on the artificial aging of Al-Mg-Si alloys.

4.2 Experimental methods

The alloy AA6061 was provided by AMAG Rolling in the form of wrought plate. The composition is given in table 4.1.

Table 4.1: Composition of alloy AA6061

Element	Al	Si	Fe	Cu	Mn	Mg	Cr	Zn	Ti
at.%	Balance	0.58	0.25	0.09	0.05	0.92	0.08	0.03	0.05
wt.%	Balance	0.60	0.52	0.22	0.11	0.82	0.15	0.07	0.08

Solution heat treatment was performed at 570 °C for 1.2 ks in a circulating air furnace (Nabertherm N60/85 SHA). I.Q. was performed in an oil bath (LAUDA Proline P 26) with an integrated basin filled with a low-melting alloy as a high performance heat transfer medium (Bi57Sn43) at temperatures ranging from 150 to 250 °C, in steps of 10 °C. Quenching was then continued by transferring the samples into water at room temperature. Subsequent intermediate natural aging was carried out at 25 °C for $1.2 \cdot 10^6$ s and artificial aging was conducted at 170 °C from 10 s to 43.2 ks. The schematic representation of the heat treatment procedure is shown in figure 4.1.

Brinell hardness measurements (HBW 2.5/62.5) were performed on samples of $20 \times 25 \times 2.5$ mm³ in an EMCO-Test M4 unit. A maximum standard deviation of 2 HBW 2.5/62.5 was achieved.

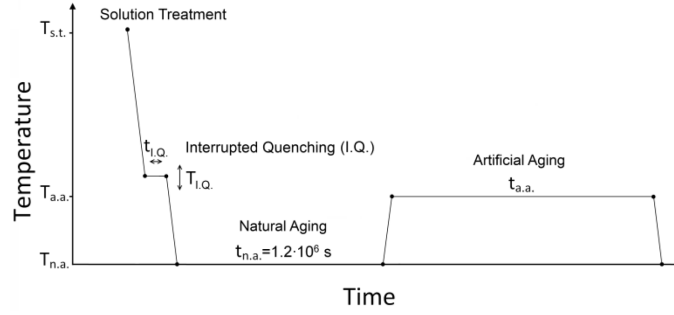


Figure 4.1: Schematic representation of the heat treatment procedure

The electrical resistivity was measured at $-196\text{ }^{\circ}\text{C}$ in liquid nitrogen using a custom-made four-point probe system and coiled AA6061 wires (1050 mm in length, 0.83 mm in diameter) as samples. Current and potential were measured separately using two digital multimeters (HP 34401 A) for a nearly constant applied current of 2 A [34,35]. To compensate systematic measurement errors, the change in specific resistivity resulting from aging experiments ($\Delta\rho$) was calculated according to equation (4.1). R_a describes the resistance after heat treatment and R_0 denotes the as-quenched state for a specimen [34,35].

$$\Delta\rho = \rho_0 \frac{R_a - R_0}{R_0} \quad (4.1)$$

The as-quenched specific electrical resistance immediately after water quenching (ρ_0) was found to be $1490 \pm 4.2\text{ n}\Omega\text{cm}$ at $-196\text{ }^{\circ}\text{C}$.

Differential scanning calorimetry (DSC) was performed on a Netzsch DSC 204 F1 Phoenix using heating rates of 2, 3.5, 6, 10, 18 Kmin^{-1} for specimens of 0.5 mm thickness and 5 mm diameter. Samples were put in the DSC apparatus at room temperature and cooled to $-40\text{ }^{\circ}\text{C}$ and equilibrated for 10 min already employing a nitrogen gas flow of 30 mlmin^{-1} . Thus, leveling of the DSC apparatus occurred at the low starting temperature and not at the interesting region above room temperature. Measurements were performed between $-40\text{ }^{\circ}\text{C}$ and $450\text{ }^{\circ}\text{C}$ in an aluminum pan with an empty aluminum pan on the reference platform. A rerun was used as baseline correction.

In order to prepare needle-shaped specimens for atom probe tomography (APT), small rods with cross-sections of $0.3 \times 0.3\text{ mm}^2$ were cut out of the corresponding hardness test samples. The specimens were then prepared via a standard two-step method: first by electropolishing of the small rods in a layer of 15 % perchloric and 85 % acetic acid solution topped over a dielectrical liquid called GaldenTM (perfluoropolyether from Solvay Solexis) and secondly using an electrolyte of 2 % perchloric acid in butoxyethanol [36]. APT was performed on a LEAPTM

3000 X HR atom probe at a temperature of $-238\text{ }^{\circ}\text{C}$. All measurements were performed with a pulse fraction of 15 % under ultra-high vacuum ($< 10^{-10}$ mbar). The reconstruction procedure and analysis were conducted using the software package IVAS 3.6.0TM from CAMECA.

Plan-view specimens for transmission electron microscopy (TEM) were prepared by a standard procedure, grinding, dimpling and electrolytic polishing and then followed by a final low energy (2.0 kV) short-time ion milling. A TEM/STEM JEOL 2100F microscope, operated at 200 kV and equipped with an image-side spherical aberration (C_s)-corrector (CEOS) and an energy filter (Gatan, Tridiem), was deployed. The atomic resolution of this microscope at 200 kV is better than 1.4 \AA . The high-resolution TEM (HRTEM) images presented here were recorded on a $2\text{ k} \times 4\text{ k}$ pixel CCD camera at a magnification of 800 k using an acquisition time of 1.0 second for each image and under negative C_s imaging conditions. To image the precipitates appropriately the specimen were tilted in [100] and [110] directions, via which the orientation relationship between needle precipitate and substrate could be clearly revealed.

4.3 Results

4.3.1 Hardness evolution

The influence of I.Q. time and temperature on hardness after intermediate natural aging and artificial aging at $170\text{ }^{\circ}\text{C}$ for 1.8 ks (common conditions for paint baking) and 28.8 ks (comparable to an industrial T6-treatment at $170\text{ }^{\circ}\text{C}$) is shown in figure 4.2. It was found that I.Q. at the lower end of the temperature range investigated (region 1) generated much higher hardness than I.Q. at the upper end of the range (region 2). This effect becomes more pronounced with longer artificial aging (figure 4.2b).

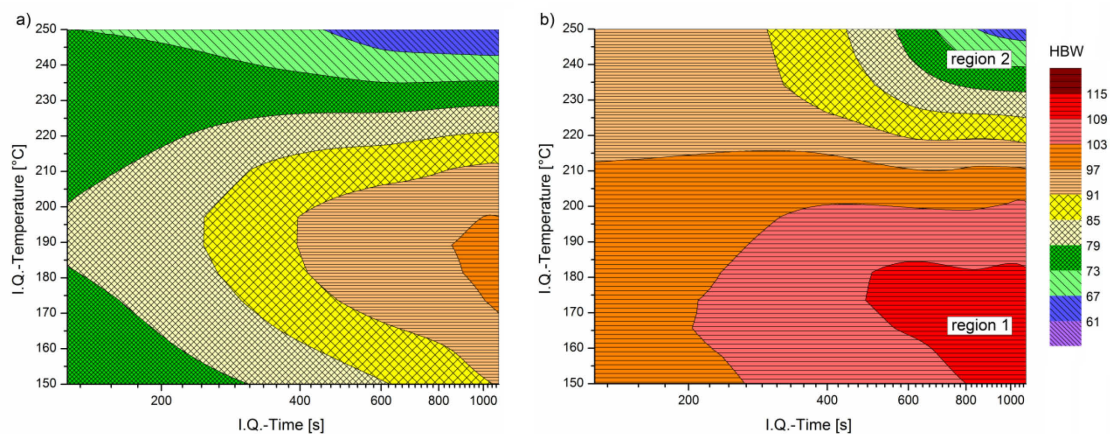


Figure 4.2: Influence of I.Q. time and I.Q. temperature on hardness after artificial aging for (a) 1.8 ks and (b) 28.8 ks at $170\text{ }^{\circ}\text{C}$ after intermediate natural aging of $1.2 \cdot 10^6$ s

For a more detailed evaluation, figure 4.3 compares the effect of I.Q. on artificial aging for various dwell periods at 160 °C (region 1) and 250 °C (region 2) to a standard water quenching procedure (w.q.). Both the kinetics and the hardening response were promoted by I.Q. at 160 °C and reduced at 250 °C with increasing I.Q. time. I.Q. of 1.08 ks at 160 °C produced superior hardening kinetics and response. I.Q. of 1.08 ks at 250 °C totally suppressed further hardening during artificial aging.

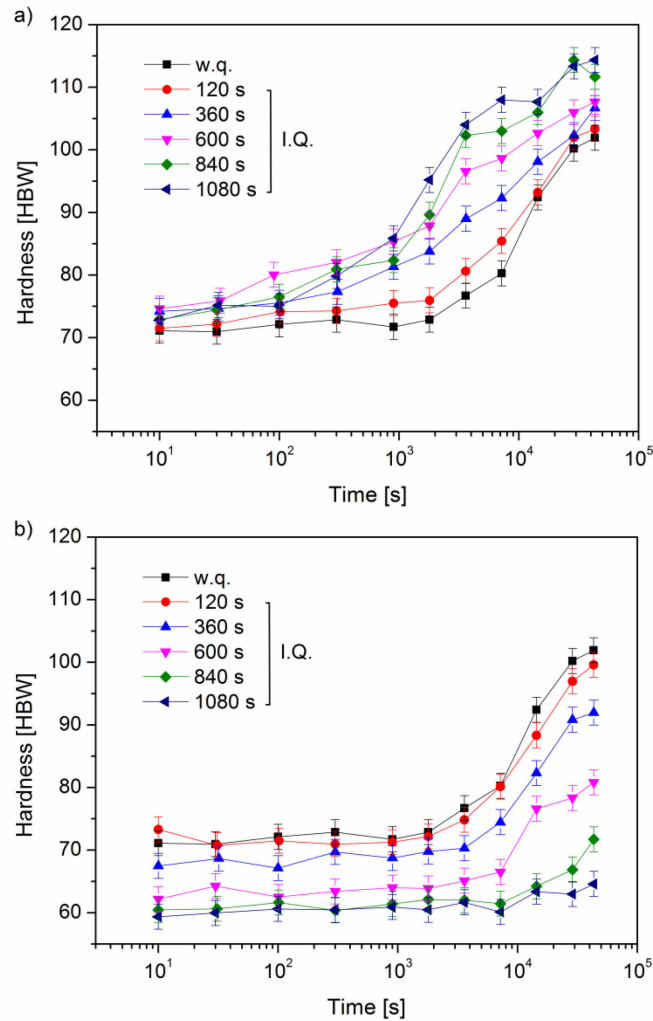


Figure 4.3: Effect of I.Q. for 120, 360, 600, 840 and 1080 s at (a) 160 °C and (b) 250 °C compared to a standard water quenching procedure (w.q.) on artificial aging at 170 °C for quoted periods after intermediate natural aging of $1.2 \cdot 10^6$ s (Hardness values after quoted artificial ageing periods)

Figure 4.4 shows the hardness immediately after I.Q. and after subsequent natural aging (I.Q. + n.a.) of $1.2 \cdot 10^6$ s depending on the I.Q. time. Interrupted quenching at 160 °C (figure 4.4a) and 250 °C (figure 4.4b) increased the hardness measured directly after quenching significantly for an I.Q. time above 120 s. This effect is more pronounced for I.Q. at 160 °C. The hardness reached after subsequent natural aging was not greatly influenced by I.Q. at 160 °C, while for

250 °C it decreased significantly with an increasing dwell period. For both temperatures, I.Q. of 1.08 ks suppressed hardening during subsequent natural aging.

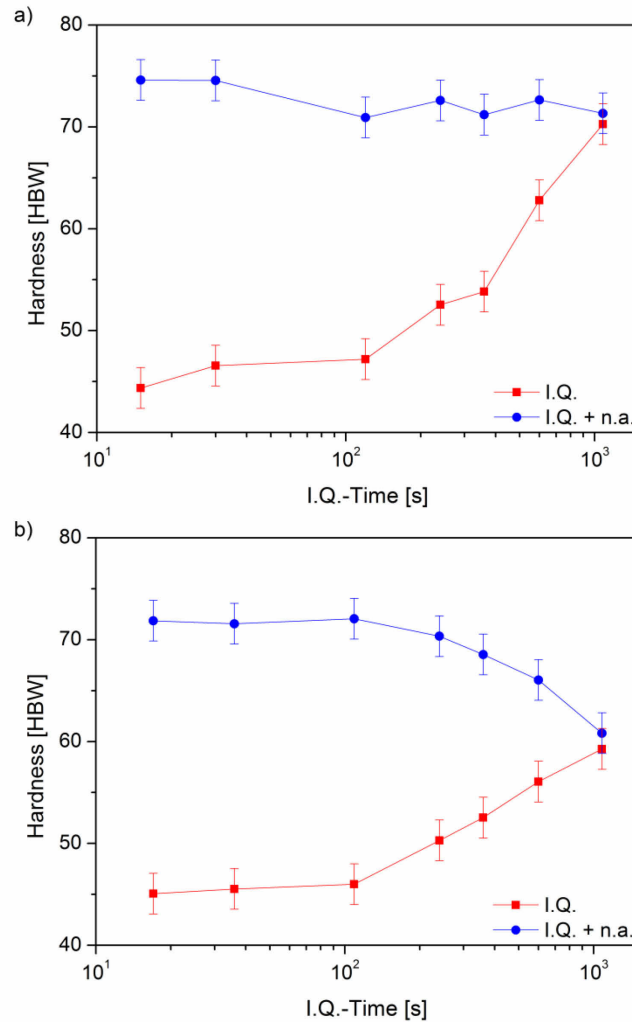


Figure 4.4: Hardness immediately after I.Q. at (a) 160 °C and (b) 250 °C and after subsequent natural aging of $1.2 \cdot 10^6$ s

4.3.2 Electrical resistivity evolution

Electrical resistivity values measured after I.Q. and subsequent natural aging of $1.2 \cdot 10^6$ s for various I.Q. conditions are shown in figure 4.5. All values of $\Delta\rho$ are referred to the as-quenched state of the water-quenched samples (see equation (4.1)). I.Q. at 160 °C did not significantly influence the resistivity measured immediately after quenching, while at 250 °C a strong decrease with increasing I.Q. time was seen (figure 4.5a). Subsequent natural aging for $1.2 \cdot 10^6$ s generated an increase in resistivity for all the quenching procedures investigated. The highest value was found for w.q., but for 120 s of I.Q. at 160 °C and 250 °C natural aging also caused a significant increase in resistivity compared to the values from figure 4.5a. For 1.08 ks

of I.Q. at 160 °C a still significant but much lower increase occurred during subsequent natural aging, while at 250 °C the rise from the level reached in figure 4.5a in resistivity was near the significance level.

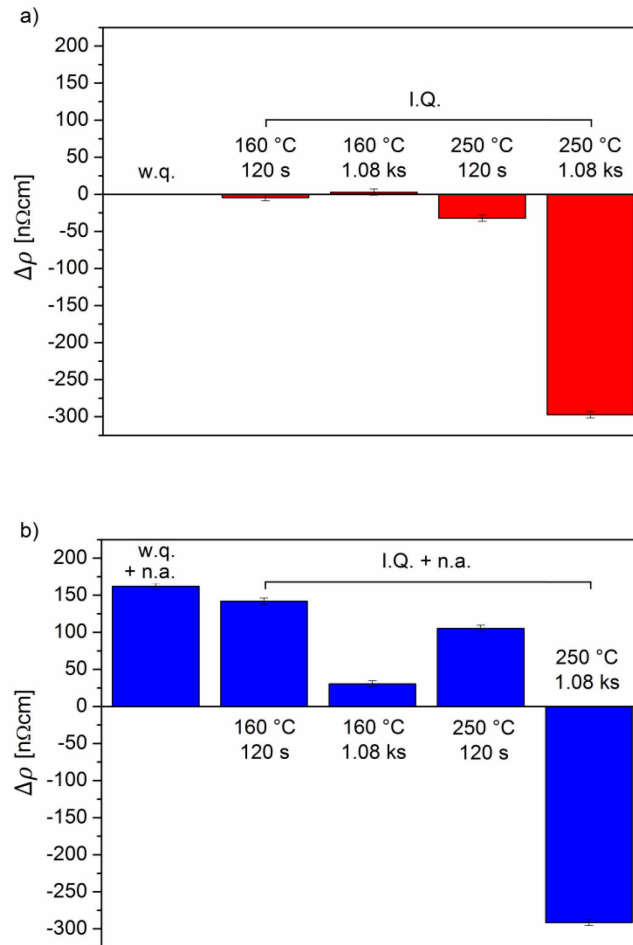


Figure 4.5: $\Delta\rho$ according to equation (4.1) (a) immediately after I.Q. and (b) after subsequent natural aging of $1.2 \cdot 10^6$ s measured at -196 °C

4.3.3 Microstructure evolution

The evolution of the microstructure during the heat treatment procedure described in figure 4.1 was investigated by APT for states where small precipitates and clusters are expected to form. For better visualization, small cylinders of identical size (65 nm in length, 45 nm in diameter) were cut from the individually analyzed volumes. Figure 4.6 shows three-dimensional (3D) reconstructions of the atom positions for Mg, Si and Cu of a sample which was interrupted quenched at 160 °C for 1.08 ks and subsequently stored at room temperature. It is obvious that the analyzed volume contains regions enriched in elements that are most relevant for precipitation in the investigated alloy AA6061. To estimate the number density and size of the clusters present, a cluster search algorithm based on the maximum separation method was deployed [37]. The separation distance (d_{max}), the surround distance (L), the erosion distance

(d_{ero}) and the minimum number of solute atoms (N_{min}) within the cluster were determined based on the method described elsewhere [38]. Accordingly, a value of 0.55 nm for d_{max} , L and d_{ero} and a value 22 for N_{min} were found to be optimal values, considering Mg, Si and Cu as constituent solute atoms of clusters. Note that all numbers of atoms discussed here take the detection efficiency of 36 % into account. Applying the parameters determined above to the cluster search algorithm, a total number density of $1.09 \cdot 10^{24} \text{ m}^{-3}$ with 78 solute atoms per cluster on average was calculated. The depletion of solute from the super-saturated solid solution was observed to be around 4 % for Cu, 8 % for Mg and 10 % for Si at this stage of the heat treatment procedure. Clusters containing less than 41 solute atoms, which was found to be the maximum number of solute atoms in co-clusters formed after long-term natural aging in the same alloy (investigated in one of our previous studies [25]), were excluded from the results of the cluster search with an N_{min} of 22 solute atoms in a second analysis. Consequently, the number density of clusters bigger than co-clusters was determined to be $5.1 \cdot 10^{23} \text{ m}^{-3}$, with 135 solute atoms per cluster on average in the sample which was I.Q. at 160 °C for 1.08 ks and subsequently stored at room temperature.

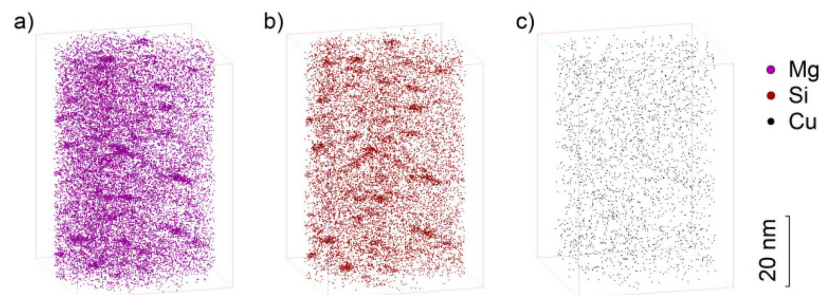


Figure 4.6: Atom probe analysis for I.Q. at 160 °C for 1.08 ks and subsequent natural aging. Atom maps of (a) Mg, (b) Si and (c) Cu

Figure 4.7 shows 3D reconstructions of the atom positions for Mg, Si and Cu of a sample which was I.Q. at 160 °C for 1.08 ks, subsequently stored at room temperature, and finally artificially aged at 170 °C for 28.8 ks. In addition to some spherical particles, a dense distribution of needle-like precipitates oriented perpendicular in three directions can be seen in figure 4.7. Applying the cluster search algorithm (0.55 nm for d_{max} , L and d_{ero} and 22 for N_{min}) a total number density of $1.03 \cdot 10^{24} \text{ m}^{-3}$ with 384 solute atoms per cluster on average was calculated. The simultaneously calculated depletion of the solute super-saturated solution increased substantially to approximately 33 % for Cu, 43 % for Mg and 51 % for Si. An exclusion of clusters smaller than 41 solute atoms revealed a number density of $5.8 \cdot 10^{23} \text{ m}^{-3}$, with 659 solute atoms per cluster on average in the sample which was I.Q. at 160 °C for 1.08 ks, stored at room temperature and finally artificially aged at 170 °C for 28.8 ks.

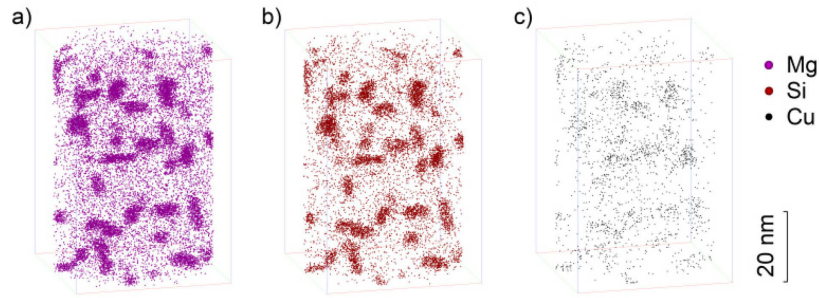


Figure 4.7: Atom probe analysis for I.Q. at 160 °C for 1.08 ks and subsequently stored at room temperature for $1.2 \cdot 10^6$ s and artificial aging at 170 °C for 28.8 ks. Atom maps of (a) Mg, (b) Si and (c) Cu

The microstructure formed by I.Q. at high temperatures was investigated by conventional transmission electron microscopy (CTEM) as well as HRTEM and scanning transmission electron microscopy (STEM). In figure 4.8a, a STEM bright-field (BF) image of the sample treated by I.Q. for 1.08 ks at 250 °C and subsequent natural aging is shown in $[100]_{\text{Al}}$ zone axis. Randomly distributed needles between 70 nm and 350 nm in length aligned along $\langle 100 \rangle_{\text{Al}}$ are dominant, and a corresponding HRTEM image from one needle along $[110]_{\text{Al}}$ zone axis is shown in figure 4.8b. The structure for the needle was determined by analyzing the fast Fourier transform (FFT) pattern calculated from the HRTEM image (figure 4.8b). By comparing the two FFTs obtained with and without needle, spots associated with this precipitate could be clearly identified in the FFT diffractogram, so that d -values of specific diffraction spots could be easily measured there (example shown in figure 4.8b). A comparison with theoretically calculated d -values for various possible structures summarized by Ravi *et al.* [20] revealed a good accordance to β'' as reported by Edwards *et al.* [4]. In addition, precipitates exhibiting approximately the same size range as the needles in the Al matrix were found on the grain boundary for I.Q. of 1.08 ks at 250 °C.

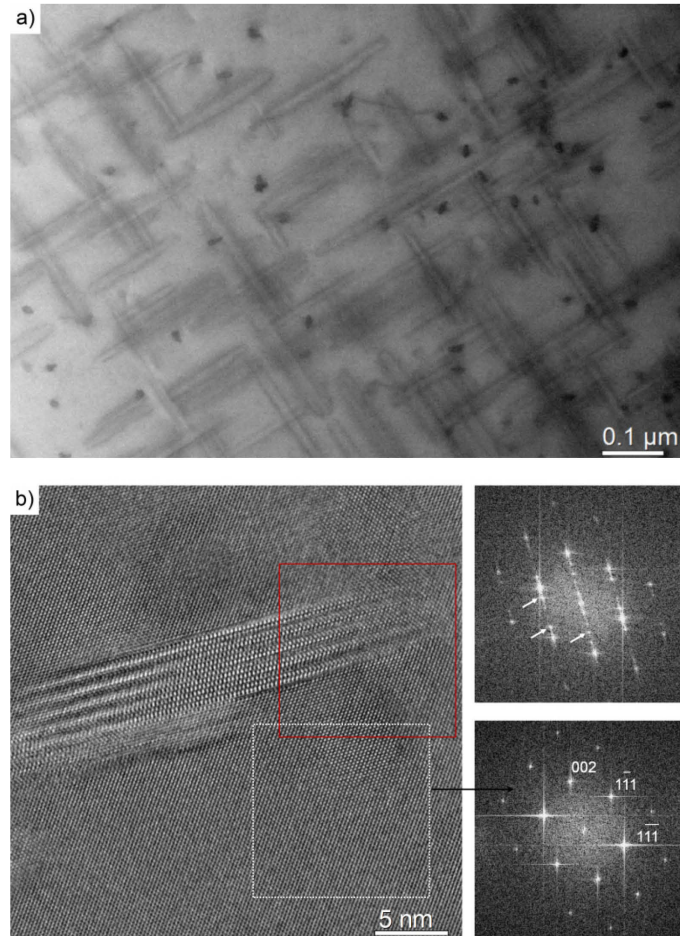


Figure 4.8: (a) STEM BF image in $[100]_{\text{Al}}$ zone axis, and (b) HRTEM image in $[110]_{\text{Al}}$ zone axis with FFTs from different regions for the sample treated by I.Q. for 1.08 ks at 250 °C

In the condition 'I.Q. for 120 s at 250 °C' no needles randomly distributed in the Al matrix were observed. Only big particles (P1) in the Al matrix were found (Fig 9a). At the P1-matrix interface small elongated precipitates (P2) were observed. The different nature of those precipitates can be deduced from the Z contrast in the high-angle annular dark field (HAADF) image. Spectra analysis by EDX (energy dispersive X-ray spectroscopy) line-scan through P1, P2 and the matrix revealed, besides Al, mainly Fe, Mn, Cr and Si for P1, and Mg and Si for P2. Additionally, it was possible to calculate an FFT pattern from the HRTEM image for P2 (Fig 9c) and to measure the corresponding d -values of specific diffraction spots for P2, which revealed a good accordance to β'' as reported by Edwards *et al.* [4]. No clear grain boundary precipitates were found for I.Q. for 120 s at 250 °C, although very small precipitates may have remained undetected by the analysis performed.

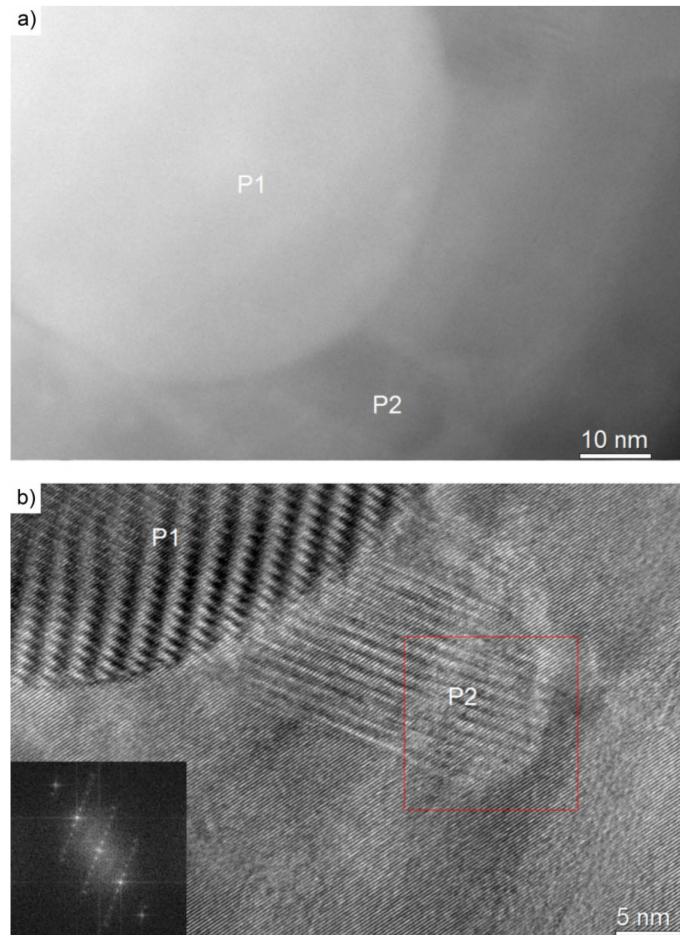


Figure 4.9: (a) HAADF-image as well as (b) HRTEM-image of particles P1 and P2 for the sample treated by I.Q. at 250 °C for 120 s in $[110]_{\text{Al}}$ zone axis

4.3.4 Differential scanning calorimetry

Figure 10 shows DSC thermograms obtained at a heating rate of 10 Kmin^{-1} of samples which were naturally aged for $1.2 \cdot 10^6 \text{ s}$ after water quenching (w.q. + n.a.) or I.Q. at 160 °C for 1.08 ks (I.Q. + n.a.). Several exothermic and endothermic reactions were observed. Those relevant to our discussion are examined in detail below. For the water quenched and naturally aged condition a small exothermic process starting at around 80 °C (I) and a following endothermic region (II) between 150 and 240 °C were seen, where the observed shoulder (I+II) may be caused by the overlapping of I and II. Between 240 and 320 °C two sharp exothermic peaks (III, IV) occurred. I.Q. for 1.08 ks at 160 °C caused a strongly differing DSC trace. Only the exothermic process I, but not the endothermic region II, was observed. Peak III appeared much broader and was strongly shifted to a lower temperature, meaning that I and III may overlap to some extent.

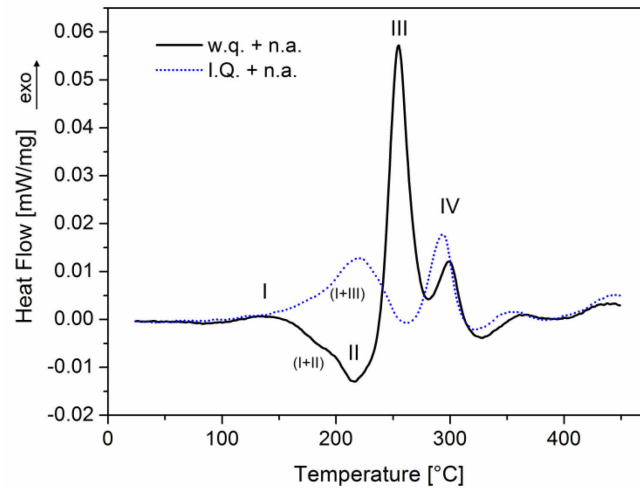


Figure 4.10: DSC thermograms of differently quenched and naturally pre-aged samples obtained at a heating rate of 10 Kmin⁻¹

In addition DSC measurements at five individual heating rates (ϕ) were performed. According to Mittemeijer *et al.* [39] an effective activation energy of precipitation reactions (Q_{eff}) can be determined from a shift of the temperatures (T_f) at which a certain fixed stage of transformation has been reached from measurements with different heating rates (equation (4.2)). Q_{eff} can be found as the slope of the straight line obtained by plotting $\ln(T_f^2/\phi)$ versus $1/T_f$ according to equation (4.2) [39,40].

$$\ln \frac{T_f^2}{\phi} = \frac{Q_{eff}}{R \cdot T_f} + \ln \frac{Q_{eff}}{R \cdot k_0} + \ln \beta_f \quad (4.2)$$

Due to overlapping effects and an uncertain baseline construction for peak III shown in figure 4.10, values of T_f could not be easily generated by integrating the DSC peak. It is assumed here that peak III corresponds to the maximum reaction rate which always occurs at about the same stage of transformation [39]. Hence the effective activation energy for III can be derived from the peak temperatures. Note that equation (4.2) is formally equivalent to the so-called ‘Kissinger analysis’ [41,42], which was originally developed for a specific kinetic model which takes into account homogenous reactions, whereas equation (4.2) was generally established for heterogeneous solid state reactions [39]. For water quenching and subsequent natural aging for $1.2 \cdot 10^6$ s an effective activation energy of 123 kJmol⁻¹ for peak III was found from figure 4.11. I.Q. at 160 °C for 1.08 ks generated an effective activation energy for peak III of 98.8 kJmol⁻¹. All graphs hold a good linear correlation.

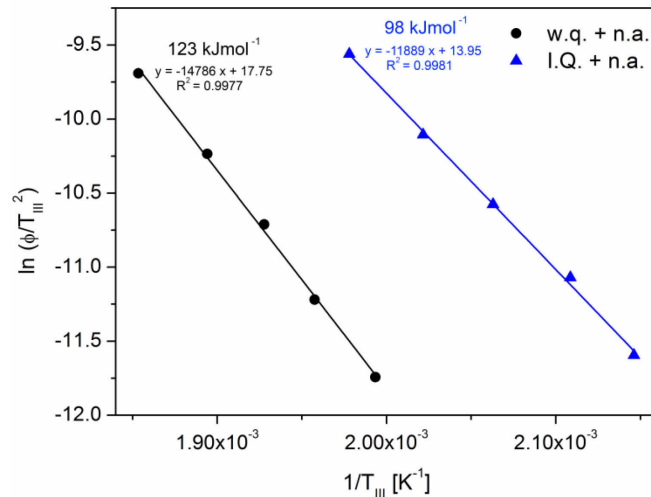


Figure 4.11: Linear fit to data points according to equation (4.2) for peak III after w.q. and subsequent natural aging and after I.Q. for 1.08 ks at 160 °C and subsequent natural aging

4.4 Discussion

It was found that the hardening kinetics and age hardening response during artificial aging after intermediate natural aging were enhanced by I.Q. at low temperatures (region 1), but reduced at high temperatures (region 2) in comparison to a standard quenching procedure (figure 4.2). The mechanisms dividing the influence of I.Q. in these two principal regions are discussed below. Furthermore, the correlation between nucleation processes during I.Q. in region 1, the co-cluster formation during natural aging and the precipitation process of β'' during artificial aging is addressed.

4.4.1 Interrupted quenching in region 1

I.Q. at low temperatures (e.g. 160 °C) has shown significant potential for preventing the negative influence of subsequent long-term natural pre-aging and for improving kinetics and the overall hardening response of artificial aging (figure 4.3). A general assumption in the discussion is that during I.Q. in region 1 similar to conventional long-term pre-aging treatments at temperatures around 100 °C [6,12,28,29], a dense distribution of nuclei for β'' or directly transformable precursors (GP-I zones) is formed. These have been shown to be capable of evolving to β'' during subsequent artificial aging [12,27]. Therefore the negative influence of natural pre-aging, which is strongly associated with the formation of co-clusters unable to act as nuclei for β'' [12] and which also immobilize quenched-in vacancies [25], can be overcome by I.Q. for a certain time in the appropriate temperature range. This agrees well with our results

from APT, which reveal a similar number density for clusters larger than co-clusters formed during I.Q. (figure 4.6) and precipitates present after the final artificial aging step, which may be mostly β'' due to their typical orientation perpendicular in three directions and needle-like appearance [14,17] (figure 4.7). β'' was also found to be the main precipitate type in a comparable heat treatment state of the same alloys studied by HRTEM by our group [43]. Although nearly the same hardness directly after I.Q. (e.g. 160 °C; 1.08 ks, figure 4.4a) was reached as via standard water quenching and subsequent long-term natural aging [25], superior artificial aging behavior (figure 4.3a) was observed for the I.Q. procedure. In addition, a totally different electrical resistivity after quenching and subsequent natural aging was measured for these two heat-treatment conditions (figure 4.5), revealing a substantially different precipitation microstructure. For Al-Mg-Si alloys, small clusters generate an anomalous resistivity maximum [35] due to an increased electron scattering [44] depending not only on their size and composition, but particularly on their number density [13]. Co-clusters formed during long-term natural aging exhibit superior scattering potential compared to later stages in the precipitation sequence [25,35]. Especially during artificial aging for long periods or at high temperatures, electrical resistivity is decreased by depletion of solute atoms from the matrix and the concurrent evolution of larger precipitates [23,34]. As a result a strong positive resistivity delta in figure 4.5 can be mostly attributed to co-clusters formed by natural aging. For I.Q. of 1.08 ks at 160 °C a suppression of the co-cluster formation can be deduced from figure 4.5b. The small remaining increase in the resistivity during natural aging may be caused by a strongly reduced number density of co-clusters and is somehow comparable to secondary aging phenomena found in under-aged Al-Mg-Si alloys [11,45]. Interestingly, the total hardness after I.Q. and long-term natural aging is not significantly influenced by I.Q. at 160 °C up to 1.08 ks (figure 4.4a), because a contribution of I.Q. reduces the potential for natural aging such that the total hardness stays constant. The observed successive suppression of co-cluster formation can be explained by a decreased solute super-saturation and/or a lowered concentration of quenched-in vacancies. According to Zurob and Seyedrezai's model [8,46] the co-cluster formation requires a high concentration of quenched-in vacancies and solute atoms which demonstrate attractive interaction, but no chemical super-saturation as a driving force. Due to the broadly accepted fact that clustering during natural aging requires enhanced diffusion [1], and because of the just slightly reduced solute content in the matrix after I.Q. for 1.08 ks at 160 °C determined by the cluster search analysis of APT data, a significant reduction in the concentration of quenched-in vacancies during I.Q. seems to be a reasonable explanation for the suppression of the co-cluster formation. We assume that the concentration of quenched-in vacancies is concurrently lowered during the formation of nuclei for β'' or its directly transformable precursors, which are supposed to be formed during I.Q.. This is in

good accordance with the found low value of the activation energy for nucleation (Q_N) reported by Esmacili *et al.* [13] for direct artificial aging (55 kJmol⁻¹). These authors concluded that this can only be explained by the migration of quenched-in vacancies (the migration energy of Mg into a nearest neighbor vacancy in Al–Mg alloys was found to be 49 kJmol⁻¹ by atomistic simulations in [47]).

We will now consider the effect of different quenching strategies on DSC measurements (figure 4.10). According to Edwards *et al.* [4], who described the precipitation process in detail for alloy AA6061, the exothermic peaks I, III and IV in figure 4.10 are associated with the formation of GP-I zones, β'' and β'/B' . The endothermic peak II is thought to be caused by the dissolution of co-clusters, which was also reported by Buha *et al.* [45], who studied samples of the alloy AA6061 with various thermal histories. The observed overlapping of GP-I zones and the β'' phase for I.Q. for 1.08 ks at 160 °C was also reported for a DSC trace directly recorded after quenching of AA6061 by Dutta and Allen [48]. I.Q. at its optimum conditions caused a broad exothermic peak at a low temperature (221.5 °C) for β'' , which accords well with supposed pre-existing nuclei. No dissolution of co-clusters was found either, matching the above-described suppression of co-cluster formation. For standard water quenching and subsequent long-term natural aging, β'' reveals a very sharp exothermic peak at much higher temperatures (254.8 °C) immediately after the dissolution of co-clusters. This accords with the model described in [25], where the dissolution of co-clusters was associated with a mobilization of imprisoned quenched-in vacancies which simultaneously enhance precipitation processes at higher temperatures. In addition, we calculated different effective activation energies for the formation of β'' for the different investigated quenching strategies (figure 4.11). The used analysis assumes an Arrhenius temperature dependency for the effective activation energy (Q_{eff}) incorporating separate activation energies for nucleation (Q_N) and growth (Q_G) [40]. In the case of a large undercooling, valid for the highly super-saturated solid solution studied in this paper, this assumption is well accepted [49]. According to Kempen *et al.* [50] Q_{eff} can be described using a weighted sum of Q_N and Q_G (equation (4.3)) applying JMA kinetics. Note that Q_N is the activation energy for atoms to jump through the interface of a particle of critical size and Q_G is similar to the activation energy for diffusion for diffusion-controlled growth [40,49]. A calculation of separate values for Q_N and Q_G has been shown to be possible by varying the nucleation mode e.g. by pre-aging [50,51]. This approach is used for a principle discussion of the determined values of Q_{eff} (figure 4.11). Taking the precipitation of β'' as a diffusion-controlled and three-dimensional process d/m is 3/2 and the growth exponent n can be expressed analytically as d/m (1.5) for pre-existing nuclei and $d/m + 1$ (2.5) for continuous nucleation [40,49,50].

$$Q_{eff} = \frac{d/m \cdot Q_G + (n - d/m) \cdot Q_N}{n} \quad (4.3)$$

The results of atom probe tomography clearly indicate the presence of pre-existing nuclei (figure 4.6), and the precipitation of β'' after I.Q. at 160 °C for 1.08 ks may be described by an n of 1.5. Applying this and Q_{eff} measured for I.Q. at 160 °C for 1.08 ks to equation (4.3) it is obvious that Q_{eff} equals Q_G (98.8 kJmol⁻¹) which is lower than for equilibrium diffusion of Mg- (121 kJmol⁻¹ [52]) and Si-diffusion (118 kJmol⁻¹ [52]) in aluminum. One reason for this may be pipe diffusion enhancing the precipitation of a certain amount of β'' precipitates, which are formed on dislocations [43].

According to the fact that co-clusters cannot act as nuclei for β'' [12] and dissolve during linear heating before the formation of β'' proceeds (figure 4.10), the precipitation of β'' after standard water quenching and subsequent long-term natural aging may be described by an n of 2.5. A value of 123 kJmol⁻¹ was found for Q_{eff} from figure 4.11. Assuming Q_G as 98.8 kJmol⁻¹, Q_N can then be found to be 159 kJmol⁻¹ from equation (4.3). Even if a value of 120 kJmol⁻¹ (estimated for equilibrium diffusion) is used for Q_G , 127.5 kJmol⁻¹ are found for Q_N .

The found high Q_N after standard water quenching and subsequent long-term natural aging can be explained by the role of vacancies for the nucleation of β'' or its directly transformable precursors. After standard water quenching and long-term natural aging, a very low concentration of mobile vacancies is expected in the matrix at common artificial aging temperatures [25]. Therefore a generation of mobile vacancies in the matrix is necessary to support the nucleation. Considering the findings in [25] it is likely that a large number of already-existing imprisoned quenched-in vacancies is released during the dissolution of co-clusters. Therefore the high activation energy found for the nucleation after long-term natural pre-aging might be seen as the sum of the activation energies for co-cluster dissolution (76 kJmol⁻¹ [25]) and vacancy-solute migration. All in all, it seems conclusive that a fast nucleation process finally leading to β'' requires quenched-in vacancies, which are not available after standard water quenching and long-term natural pre-aging, but can be provided during I.Q. in the right temperature region.

4.4.2 Interrupted quenching in region 2

It has been shown that natural (figure 4.4) and artificial aging (figure 4.3) can be adversely influenced by I.Q. at 250 °C. Beside the aforementioned effect of small clusters [35], electrical resistivity is mainly influenced by solute depletion [53]. Therefore the strong decrease found in electrical resistivity by I.Q. of 1.08 ks at 250 °C (figure 4.5a) can be explained by solute depletion and a concurrent evolution of precipitates much larger than those responsible for the anomalous increase in resistivity. A similar decrease in resistivity has been previously reported for artificial aging of Al-Mg-Si alloys [23,34]. Those precipitates formed during I.Q. at 250 °C were identified to be β'' [4] by a comparison of measured d -spacings from the FFT (figure 4.8b) with theoretically calculated values for various possible structures summarized by Ravi *et al.* [20]. The observed rapid formation of a coarse distribution of β'' during I.Q. at 250 °C does not contribute much to the hardness (figure 4.4b) according their huge separation distance (figure 4.8a). Instead, it lowers the solute super-saturation of the matrix and therefore reduces the potential for subsequent aging, because its kinetics is linked to the driving force depending on the solute super-saturation [54]. For a short period of I.Q. (120 s at 250 °C), a significant decrease in resistivity was also observed (figure 4.5), although no precipitates could be found in the matrix via TEM investigations. The reduction in the hardening potential compared to a standard water-quenched sample was observed to be very small (figure 4.3b). This might be explained by the lower sensitivity to the solute super-saturation of the hardness compared to electrical resistivity. A possible explanation for the observed decrease in electrical resistivity is the formation of precipitates at heterogeneous nucleation sites. For low quenching rates (e.g. air cooling) grain boundary precipitation is a well-known phenomenon in Al-Mg-Si alloys [31,55]. In addition, AA6061 contains dispersoids of type α -AlFe(Cr,Mn)Si, which have been reported as preferential nucleation sites [1,55-57]. Grain boundary precipitates were not found for I.Q. for 120 s at 250 °C, although very small precipitates may not have been detected by the STEM analysis performed. Heterogeneous nucleation on dispersoids, however, was observed in a sample I.Q. for 120 s at 250 °C. An FFT generated from the HRTEM image of the heterogeneously nucleated precipitate P2 shown in figure 4.9b was found to be analogous to those of β'' precipitates found in the matrix for I.Q. of 1.08 ks at 250 °C (figure 4.8b).

In summary, two mechanisms responsible for the reduction of the solute super-saturation during I.Q. at high temperatures were identified which can significantly affect the subsequent potential for artificial aging: i) precipitation at heterogeneous nucleation sites dominates during short I.Q. ii) formation of random, but non-hardenable precipitates during proceeding I.Q..

4.5 Conclusions

The objective of this study was to investigate interrupted quenching (I.Q.) as a new heat treatment strategy and shed more light on the role of quenched-in vacancies in the nucleation of β'' .

- Depending on the temperature range, I.Q. can either affect artificial aging by a reduction of the remaining solute super saturation or promote artificial aging by the formation of a dense distribution of nuclei for β'' or its directly transformable precursors.
- Rapid nucleation, finally leading to β'' -precipitates, requires quenched-in vacancies. These can be provided via I.Q. in the right temperature region, but not by standard water quenching and long-term natural pre-aging.
- Overall, the role of quenched-in vacancies during nucleation is considered to be the key to understanding the influence of natural pre-aging on artificial aging of Al-Mg-Si alloys.

Acknowledgments

The authors gratefully thank the people at AMAG Rolling, especially Thomas Ebner, for the fruitful discussion and for providing the alloys. We are also grateful to the Austrian Research Promotion Agency (FFG) and AMAG Rolling for financial support of this work.

References

- [1] Ostermann F. Anwendungstechnologie aluminium. Berlin: Springer-Verlag; 2007.
- [2] Banhart J, Lay MDH, Chang CST, Hill AJ. Phys Rev B 2011;83:art. no. 014101--.
- [3] Banhart J, Chang CST, Liang ZQ, Wanderka N, Lay MDH, Hill AJ. Adv Eng Mater 2010;12:559.
- [4] Edwards GA, Stiller K, Dunlop GL, Couper MJ. Acta Mater 1998;46:3893.
- [5] Chang CST, Wieler I, Wanderka N, Banhart J. Ultramicroscopy 2009;109:585.
- [6] De Geuser F, Lefebvre W, Blavette D. Phil Mag Lett 2006;86:227.
- [7] Murayama M, Hono K, Saga M, Kikuchi M. Mater Sci Eng A 1998;250:127.

- [8] Seyedrezai H, Grebennikov D, Mascher P, Zurob HS. *Mater Sci Eng A* 2009;525:186.
- [9] van Huis MA, Chen JH, Sluiter MHF, Zandbergen HW. *Acta Mater* 2007;55:2183.
- [10] van Huis MA, Chen JH, Zandbergen HW, Sluiter MHF. *Acta Mater* 2006;54:2945.
- [11] Buha J, Lumley RN, Crosky AG, Hono K. *Acta Mater* 2007;55:3015.
- [12] Murayama M, Hono K. *Acta Mater* 1999;47:1537.
- [13] Esmacili S, Vaumousse D, Zandbergen MW, Poole WJ, Cerezo A, Lloyd DJ. *Phil Mag* 2007;87:3797.
- [14] Andersen SJ, Zandbergen HW, Jansen JE, Taeholt C, Tundal U, Reiso O. *Acta Mater* 1998;46:3283.
- [15] Marioara CD, Andersen SJ, Jansen J, Zandbergen HW. *Acta Mater* 2001;49:321.
- [16] Matsuda K, Gamada H, Fujii K, Uetani Y, Sato T, Kamio A *et al.* *Metall Mater Trans A* 1998;29:1161.
- [17] Zandbergen HW, Andersen SJ, Jansen J. *Science* 1997;277:1221.
- [18] Vissers R, van Huis MA, Jansen J, Zandbergen HW, Marioara CD, Andersen SJ. *Acta Mater* 2007;55:3815.
- [19] Dumolt SD, Laughlin DE, Williams JC. *Scr Metall Mater* 1984;18:1347.
- [20] Ravi C, Wolverton C. *Acta Mater* 2004;52:4213.
- [21] Brenner P, Kostron H. *Z Metall* 1939;4:89.
- [22] Borchers H, Kainz M. *Metall* 1963;17:400.
- [23] Kovacs I, Nagy E, Lendvai J. *Acta Metall* 1972;20:975.
- [24] Ried A, Schwellinger P, Bichsel H. *Aluminium* 1977;53:595.
- [25] Pogatscher S, Antrekowitsch H, Leitner H, Ebner T, Uggowitzner PJ. *Acta Mater* 2011;59:3352.
- [26] Serizawa A, Hirozawa S, Sato T. *Mater Sci Forum* 2006;519-521:245.
- [27] Marioara CD, Andersen SJ, Jansen JE, Zandbergen HW. *Acta Mater* 2003;51:789.
- [28] Slámová M, Janecek M, Cieslar M, Šíma V. *Mater Sci Forum* 2007;567-568:333.
- [29] Bryant JD. *Metall Mater Trans A* 1999;30:1999.
- [30] Saga M, Sasaki Y, Kikuchi M, Yan Z, Matsuo M. *Mater Sci Forum* 1996;217:821.
- [31] Steele D, Evans D, Nolan P, Lloyd DJ. *Mater Charct* 2007;58:40.
- [32] de Haas M, De Hosson JTM. *J Mater Sci* 2002;37:5065.
- [33] Svenningsen G, Larson MH, Nordlien JH, Nisancioglu K. *Corr Sci* 2006;48:258.
- [34] Esmacili S, Lloyd DJ, Poole WJ. *Mater Lett* 2005;59:575.
- [35] Panseri C, Federighi T. *J Inst Met* 1966;94:99.
- [36] Miller MK, Cerezo A, Hetherington MG, Smith GDW. *Atom Probe Field Ion Microscopy*. Oxford: Oxford University Press; 1996.
- [37] Cerezo A, Davin L. *Surf Inter Anal* 2007;39:184.

- [38] Vaumousse D, Cerezo A, Warren PJ. *Ultramicroscopy* 2003;95:215.
- [39] Mittemeijer EJ. *J Mater Sci* 1992;27:3977.
- [40] Liu F, Sommer F, Bos C, Mittemeijer EJ. *Int Mater Rev* 2007;52:193.
- [41] Kissinger HE. *J Res Nat Bur Stand* 1956;57:217.
- [42] Kissinger HE. *Anal Chem* 1957;29:1702.
- [43] Pogatscher S, Antrekowitsch H, Leitner H, Sologubenko AS, Uggowitzner PJ. *Scr Mater* 2012. To be published
- [44] Hillel AJ, Rossiter PL. *Phil Mag B* 1981;44:383.
- [45] Buha J, Lumley RN, Crosky AG. *Metall Mater Trans A* 2006;37A:3119.
- [46] Zurob HS, Seyedrezai H. *Scr Mater* 2009;61:141.
- [47] Picu RC, Zhang D. *Acta Mater* 2004;52:161.
- [48] Dutta I, Allen SM. *J Mater Sci Lett* 1991;10:323.
- [49] Bauer R, Rheingans BF, Mittemeijer EJ. *Metall Mater Trans A* 2011;42:1750.
- [50] Kempen ATW, Sommer F, Mittemeijer EJ. *J Mater Sci* 2002;37:1321.
- [51] Kempen ATW, Sommer F, Mittemeijer EJ. *Acta Mater* 2002;50:1319.
- [52] Du Y, Chang YA, Huang BY, Gong WP, Jin ZP, Xu HH *et al.* *Mater Sci Eng A* 2003;363:140.
- [53] Fickett FR. *Cryogenics* 1971;11:349.
- [54] Christian JW. *The Theory of Transformations in Metals and Alloys*. Oxford: Pergamon; 1981.
- [55] Morgeneyer TF, Starink MJ, Wang SC, Sinclair I. *Acta Mater* 2008;56:2872.
- [56] Bomas, H. Effect of the Cooling Rate during the Solution Heat Treatment on the Structure and Mechanical Properties of AlMgSi Alloys, in: Jeglitsch F (Ed.), 7th Internationale Leichtmetalltagung. Leoben and Vienna, Austria: Vereinigten Metallwerke Ranshofen-Berndorf; 1981.
- [57] Røyset J, Tundal U, Reiso O. *Mater Forum* 2004;28:300.

5 COMPOSITION I

This chapter addresses the fundamental differences in the effect of natural pre-aging on artificial aging in the rich Al-Mg-Si alloy AA6061 and the lean Al-Mg-Si alloy AA6060. The dissolution of Mg,Si co-clusters during artificial aging is studied in a wide temperature range for both types of alloys, which is a key to applying the model developed in chapter 2. To extend the model to the lean alloy AA6060 the annihilation of quenched-in vacancies during artificial aging is discussed in a wide temperature range.

The Role of Co-Clusters in the Artificial Aging of AA6061 and AA6060*

In this study the role of Mg,Si-co-clusters formed during long-term natural aging on the artificial aging behavior was investigated by hardness measurements for the alloys AA6061 and AA6060. It was found that kinetics and age hardening response of artificial aging at common temperatures (e.g. 170 °C) are lowered by a strong presence of co-clusters, but enhanced at high temperatures (e.g. 250 °C) for AA6061. Co-cluster formation in the alloy AA6060 increases the age hardening response at 170 °C, but barely influences kinetics in both temperature regions. The co-cluster dissolution was analyzed by a model based on temperature dependent reversion of the hardness, which showed similar activation energies for both alloys. It is supposed that the different behavior of the alloys AA6061 and AA6060 can be explained by solute-vacancy interactions.

5.1 Introduction

Nowadays Al-Mg-Si alloys are the commercially most frequently used group of age hardenable aluminum alloys [1]. Although they were developed 85 years ago, several aging phenomena are still poorly understood. This arises from the limits of available experimental methods [2] and the complexity of early stage precipitation reactions in this alloy system. Especially the influence of natural pre-aging on artificial aging, which depends on the type of Al-Mg-Si alloy and the temperature where artificial aging is performed [3], is not fully resolved even though it has been investigated over the last 70 years [2]. The alloys AA6061 and AA6060 are important members in the family of Al-Mg-Si alloys and mark two extreme cases concerning the influence of natural pre-aging [4]. Alloys with higher alloying content such as AA6061 are used for applications that require higher strength such as construction, automotive engineering, shipbuilding and the aircraft industry. For these alloys a strong adverse influence of natural pre-aging on the precipitation kinetics and the hardening response at common artificial aging temperatures (e.g. 170 °C) has been reported [5-8]. Further it has been reported recently that kinetics and age hardening response of AA6061 can also be enhanced by natural pre-aging, when artificial aging is performed at unconventional high temperatures (e.g. 250 °C) [3]. Lean alloys such as AA6060 provide a medium strength and are often used for extrusions in transportation [4]. In contrast to rich alloys a positive influence of natural pre-aging has been found at common artificial aging temperatures [8,9].

*Pogatscher S, Antrekowitsch H, Ebner T, Uggowitzer PJ. In Suarez EC, editor. TMS Light Metals. Orlando. TMS; 2012. p. 415.

Beside the fundamental aspect of understanding the mechanisms responsible for the ambiguous influence of natural pre-aging, the negative effect in rich alloys is of considerable industrial importance because the production of many heat-treated semi-finished products is affected by logistically unavoidable natural pre-aging [4]. Furthermore, the use of such alloys for automotive outer panel applications is restricted by the sluggish kinetics after intermediate natural aging. This led to the development of numerous heat treatments strategies to minimize the negative effect of natural pre-aging [10-15]. The industrial importance of the negative effect might be the reason that rich alloys have been extensively studied at common artificial aging temperatures, while lean alloys and unconventional artificial temperatures have been barely investigated. For an appropriate examination of these two previously untended issues the precipitation sequence of Al-Mg-Si alloys should be addressed first [16]:

SSSSS \rightarrow Individual clusters \rightarrow Co-clusters \rightarrow GP-I zones $\rightarrow \beta'' \rightarrow \beta'$ and others $\rightarrow \beta$

Note that this general sequence is not without controversy in the early stages, can differ with the alloy composition, and is only valid during linear heating. After the first stages including individual solute clustering of Si and Mg and cluster dissolution reactions, Mg,Si-co-clusters are formed from the super-saturated solid solution (SSSS) [16]. Co-clusters [2,9,16,17,17-19] were also found after long-term room temperature exposure, whereat Banhart *et al.* [1] recently reported that natural aging of Al-Mg-Si alloys is a rather complex process taking place in several individual stages. Since the notation of the finally formed clusters is not consistent in the literature (co-clusters are termed as both initial- β'' [20] and GP-zones [21]) in this work the term co-cluster is only used for clusters formed after long-term natural aging. Consecutively formed GP-I zones [22-24] are thermally more stable, contain more solute atoms, and are most often found to be spherical, with a typical size of 1 to 3 nm [25]. At peak aged states needle-like monoclinic β'' (Mg_5Si_6) precipitates were found to be responsible for the major hardness increase [25,26]. For overaged microstructures various hexagonal rod-shaped phases [16,21,22,27-29] have been reported (β' and others). The equilibrium phase is the platelet-like β precipitate (Mg_2Si) [16,20,21,30]. In the past many researchers argued on the negative influence of natural pre-aging at common artificial aging temperatures more or less addressing the role of co-clusters during artificial aging. Ried *et al.* [8] thought that natural aging reduces the vacancy concentration and solute super-saturation (due to the formation of co-clusters), which should rise the critical nucleation size for β'' [31]. Murayama *et al.* [18] expected that co-clusters, which form during room temperature storage, are too small to act as nucleation sites for β'' and would be completely reverted at common artificial aging temperatures. Resent results indicate that artificial aging kinetics of AA6061 is controlled via the concentration of mobile vacancies,

which is determined by a temperature-dependent dissolution of co-clusters associated with the release of imprisoned quenched-in vacancies. Due to a very slow co-cluster dissolution at low temperatures the precipitation process is strongly retarded at common artificial aging temperatures and enhanced at high artificial aging temperatures [3]. The positive effect has not been investigated comprehensively, but Chang *et al.* [9] assumed that in lean alloys a different nature of co-clusters might exist, which dissolve very slowly and could serve as nuclei for subsequent phases. However, the picture of the role of co-clusters during artificial aging at different temperatures for various Al-Mg-Si alloys is far from complete. Thus, the present work was performed to investigate the artificial aging behavior at common and high temperatures of two principal Al-Mg-Si alloys especially focusing on the role of co-clusters.

5.2 Experimental methods

The alloy AA6061 was supplied by AMAG Rolling and the alloy AA6060 was provided by Light Metals Technologies Ranshofen. Their composition is given in table 5.1.

Table 5.1: Composition of alloy AA6060 and AA6061

Alloy \ wt%	Al	Si	Fe	Cu	Mn	Mg	Cr
AA6060	Balance	0.41	0.17	-	-	0.43	-
AA6061	-	0.60	0.52	0.22	0.11	0.82	0.15

Solution heat treatment was performed in a circulating air furnace (Nabertherm N60/85 SHA) at 570 °C for 20 min. Specimens were then heat treated according the time-temperature sequences described in figure 5.1. Quenching was carried out in water at RT, followed by natural pre-aging for $1.2 \cdot 10^2$ s (B1) and $1.2 \cdot 10^6$ s (B2) at 25 °C. In order to achieve a good temperature accuracy during artificial aging, an oil bath (LAUDA Proline P 26) with an integrated basin filled with a low-melting alloy as a high performance heat transfer medium (Bi57Sn43) was used. Samples were positioned in a cage near a platinum thermometer (Pt100), which facilitated a temperature accuracy of ± 0.1 °C.

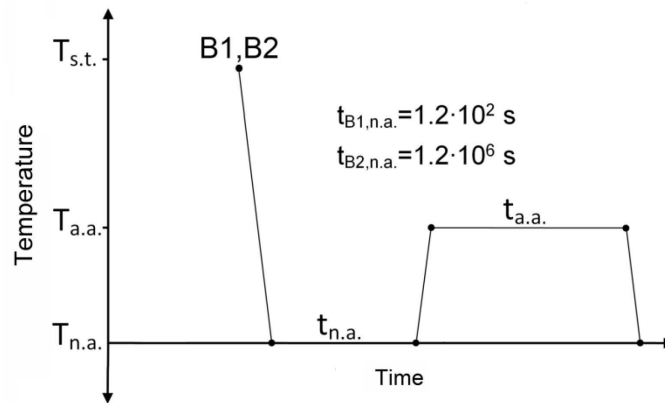


Figure 5.1: Heat treatment procedures

Brinell hardness measurements were performed in an EMCO-Test M4 unit. For the alloy AA6061 HBW 2.5/62.5 was used. Especially for the lower range of the hardness of the softer alloy AA6060 this method is not optimal. Therefore HBW 2.5/31.25, which facilitated a more accurate measurement in terms of deviation of the measured hardness values, was used. Note that hardness values measured with different methods cannot be exactly converted into each other in principal. But for the present study it was proven experimentally that both values do not differ strongly in the investigated range and can therefore be roughly compared.

5.3 Experimental results

5.3.1 Natural aging

Hardness curves for natural aging at 25 °C of AA6060 and AA6061 are shown in figure 5.2. After a slow initial change and a rapid hardness increase a nearly constant value of 39.2 HBW 2.5/31.25 was reached for AA6060 (figure 5.2a). AA6061 exhibited the same three stage behavior resulting in a nearly constant hardness value of 73 HBW 2.5/62.5 (figure 5.2b). The natural aging kinetics of AA6060 is only slightly slower than for AA6061, but the total increase of the hardness is much lower for the alloy AA6060.

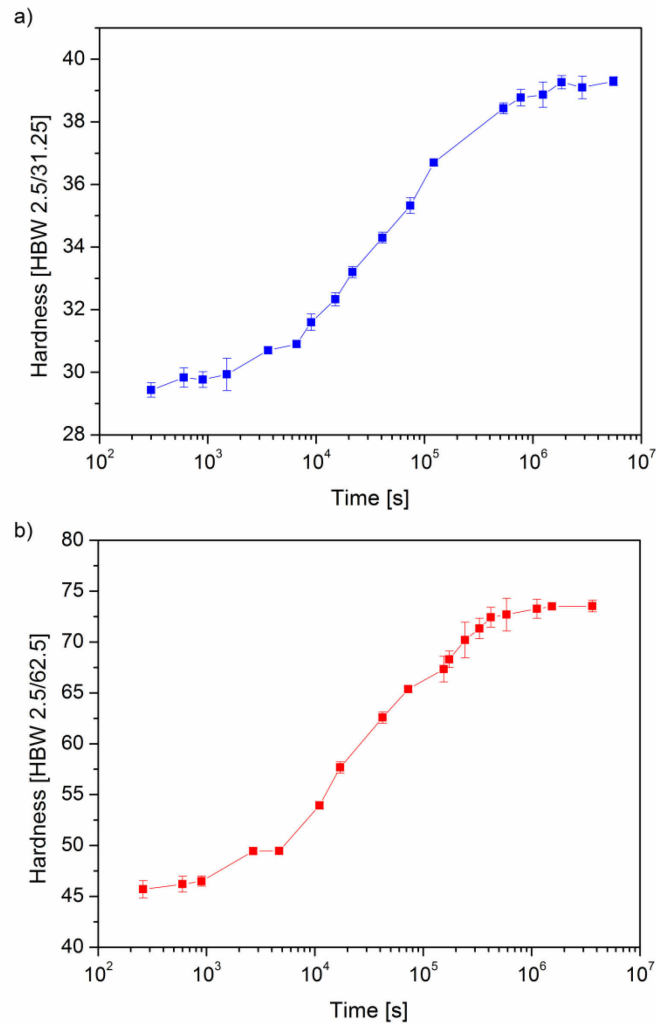


Figure 5.2: Hardness curve for natural aging at 25 °C of (a) AA6060 and (b) AA6061

5.3.2 Artificial aging

Hardness curves obtained by the artificial aging procedures B1 and B2 at 170 °C are shown for AA6060 and AA6061 in figure 5.3. In order to help the reader, additionally the hardness measured after long-term natural aging (n.a.) is plotted. Examining alloy AA6060, the intermediate natural aging (B2) shifted the hardness curve to higher values, whereby the contribution of co-clusters to the hardness seems to be constant over a long aging time and no significant reversion was observed (figure 5.3a). Kinetics was not affected by long-term natural pre-aging (B2) and has been found to be similar but very slow for B1 and B2. The alloy AA6061 exhibited a totally different behavior (figure 5.3b). Artificial aging directly after quenching (B1) resulted in very rapid kinetics and high peak hardness. For B2, kinetics was found to be strongly retarded and nearly as slow as for the alloy AA6060. Furthermore, the peak hardness of B2 is lower than for B1. Similar to AA6060 no observable reversion of co-clusters took place.

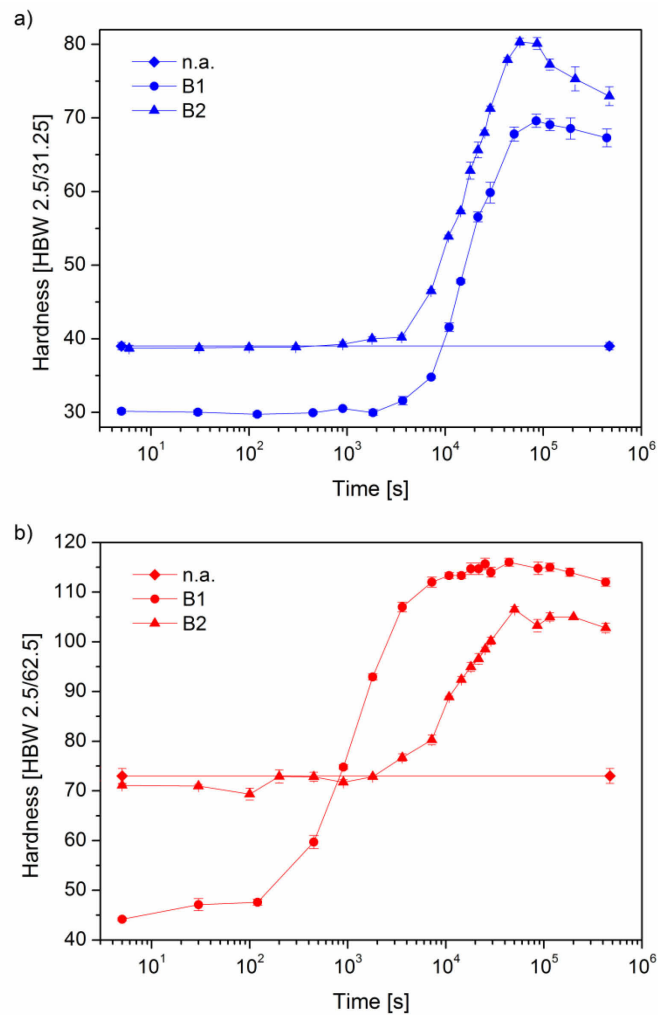


Figure 5.3: Hardness curves for artificial aging procedures B1 and B2 at 170 °C for (a) AA6060 and (b) AA6061

The hardening behavior of the two alloys applying procedure B1 and B2 at 250 °C artificial aging temperature is shown in figure 5.4. Beside a rapid reversion of the hardness, reached after natural aging and a slightly higher peak hardness for B2, both heat treatment procedures exhibited similar kinetics for the alloy AA6060 (figure 5.4a). Compared to artificial aging at 170 °C faster kinetics has been found for B1 and B2, so that the initial period till the first hardness increase occurred, reduced from $\sim 3 \cdot 10^3$ s to $\sim 10^2$ s and the time to peak hardness decreased from $\sim 7 \cdot 10^4$ s to $\sim 3 \cdot 10^3$ s. For the alloy AA6061 a different behavior has been found (figure 4b). Beside a rapid reversion, procedure B2 showed accelerated aging kinetics and significant higher peak hardness than B1. Compared to artificial aging at 170 °C extremely enhanced kinetics has been found for B2, so that the initial period till the first hardness increase occurred, reduced from $\sim 2 \cdot 10^3$ s to $\sim 2 \cdot 10^1$ s and the time to peak hardness decreased from $\sim 1 \cdot 10^5$ s to \sim

$9 \cdot 10^2$ s. Interestingly, B1 revealed nearly the same initial period till the first hardness increase occurred ($\sim 10^2$ s) at both temperatures, while the time to peak hardness decreased from $\sim 3 \cdot 10^4$ s to $\sim 3 \cdot 10^3$ s.

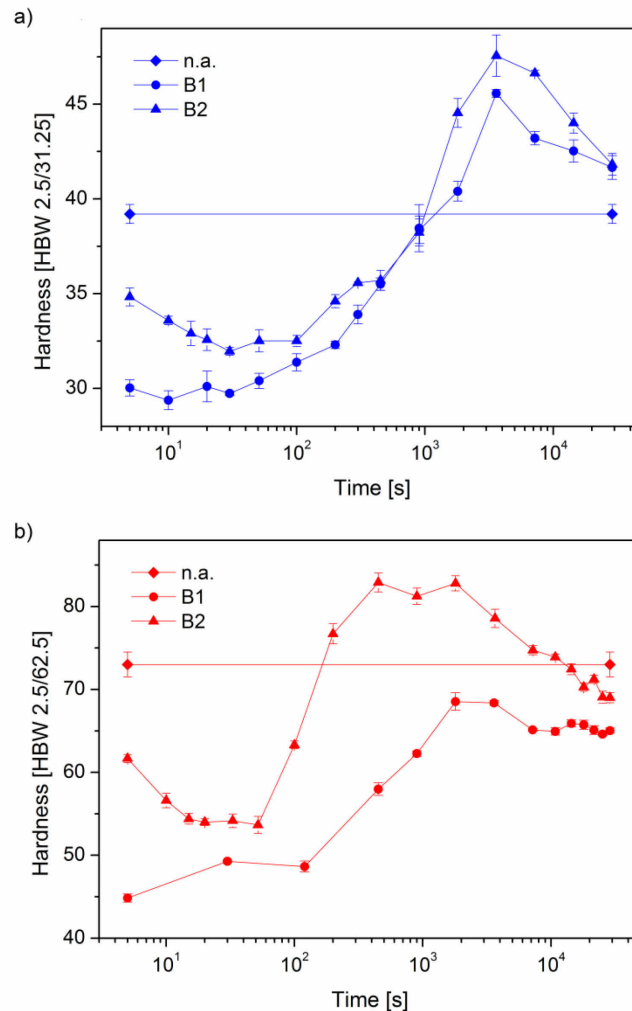


Figure 5.4: Hardness curves for artificial aging procedures B1 and B2 at 250 °C for (a) AA6060 and (b) AA6061

5.3.3 Co-cluster dissolution natural aging

The reversion of the hardness is a good indicator for the dissolution of co-clusters formed during long-term natural aging, which can be analyzed by a simple model already used for this purpose in [3]. Its basic assumptions have to be considered and should be briefly recapitulated. The hardness is supposed to be proportional to the contribution of co-clusters, treated as shearable obstacles [32-34], to the yield strength. Furthermore, the slightly increasing solution strengthening is neglected. Accepting this, a relationship between the relative volume fraction of co-clusters ($f_r^{n.a.}$) and the hardness during early stages of the reversion, where the

contribution of aging is negligible, can be express by equation (5.1). The hardness after long-term natural aging ($H_{n.a.}$) was set to 39.2 HWB 2.5/31.25 for AA6060 and to 73 HBW 2.5/62.5 for AA6061. For AA6060 the as-quenched hardness ($H_{a.q.}$) was found to be 29 HBW 2.5/31.25 and for AA6061 a value of 43 HBW 2.5/62.5 was measured.

$$\sqrt{f_r^{n.a.}} \propto \frac{H - H_{a.q.}}{H_{n.a.} - H_{a.q.}} \quad (5.1)$$

The time-dependence of $f_r^{n.a.}$ during reversion can be described by equation (5.2), which basically results of a mathematical model for a diffusion-controlled solution of a second phase in an infinite matrix [34]. B is a factor with an Arrhenius temperature dependence (equation (5.3)), characterized by the activation energy for the dissolution of co-clusters ($Q_{diss.}$) and the pre-exponential factor B_0 . The activation energy for the dissolution of co-clusters includes the enthalpy of solution of co-clusters (Q_s) and the activation energy for diffusion (Q_d) (equation (5.4)).

$$f_r^{n.a.} = (1 - B \cdot t^{0.5})^3 \quad (5.2)$$

$$B = B_0 \cdot \exp\left(\frac{-Q_{diss.}}{k \cdot T}\right) \quad (5.3)$$

$$Q_{diss} = Q_s + \frac{Q_d}{2} \quad (5.4)$$

In figure 5.5 the relative volume fraction of co-clusters during the early stage of artificial aging according to procedure B2 obtained from hardness measurements is shown for different aging temperatures for AA6060 (figure 5.5a) and AA6061 (figure 5.5b).

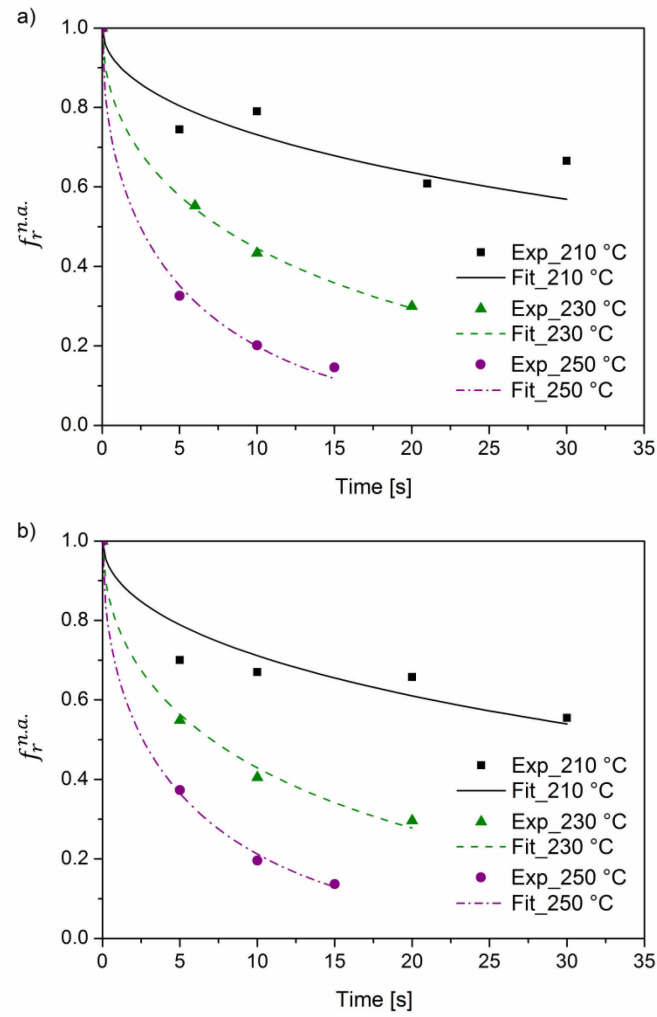


Figure 5.5: Relative volume fraction of co-clusters during reversion at different temperatures for (a) AA6060 and (b) AA6061

Furthermore, the results of fitting the experimental data by a least squares algorithm according to equation (5.2) are shown. Values of B obtained by fitting are listed in table 5.2.

Table 5.2: B-values of alloy AA6060 and AA6061

T [°C]	B [s ^{-0.5}]	
	AA6060	AA6061
190	1.42E-2	1.24E-2
200	1.81E-2	2.54E-2
210	3.13E-2	3.39E-2
220	4.41E-2	5.07E-2
230	7.47E-2	7.77E-2
240	9.84E-2	1.01E-1
250	1.31E-1	1.28E-1

The activation energy for the dissolution of co-clusters and the pre-exponential factor B_0 can be determined by an Arrhenius plot of equation (5.3) (figure 5.6). For AA6060 the value for $Q_{diss.}$ was found to be 79 kJmol^{-1} and B_0 revealed a value of $9.8 \cdot 10^{-6} \text{ s}^{-0.5}$. The alloy AA6061 showed insignificantly lower values for the activation energy (77 kJmol^{-1}) and B_0 ($6.6 \cdot 10^{-6} \text{ s}^{-0.5}$).

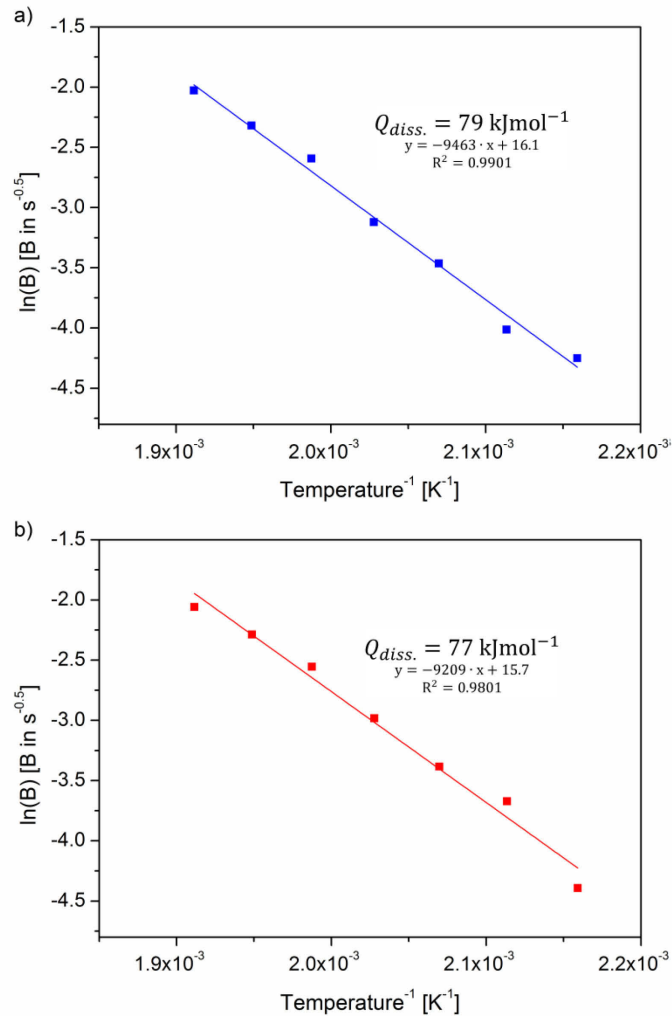


Figure 5.6: Arrhenius plot of equation (5.3) for (a) AA6060 and (b) AA6061

5.4 Discussion

The present study reveals a totally different influence of the co-cluster formation during long-term natural aging on subsequent artificial aging at common (e.g. $170 \text{ }^\circ\text{C}$) and high temperatures (e.g. $250 \text{ }^\circ\text{C}$) for the alloys AA6060 and AA6061. A significant increase of the hardening response, but no influence on kinetics was observed for AA6060 at $170 \text{ }^\circ\text{C}$ (figure 5.3a). At $250 \text{ }^\circ\text{C}$ the long-term natural aging showed a rather small influence, excepting the

dissolution of co-clusters at the very beginning of artificial aging (figure 5.4a). For AA6061 kinetics and age hardening response of artificial aging at 170 °C are strongly lowered by the presence of co-clusters, while both are significantly enhanced at 250 °C (figure 5.3b, figure 5.4b). Interestingly, the analysis of the dissolution of co-clusters during artificial aging revealed a similar behavior for both alloys (figure 5.5, figure 5.6).

Note that the values found for Q_{diss} are comparable to the value given in [34]. This findings contrast the idea of Chang *et al.* [9], who speculated that a different nature of co-clusters exists in lean alloys, dissolving very slowly and serving as nuclei. Instead, we believe that the rather complex effects of long-term natural aging of different Al-Mg-Si alloys can be explained on the basis of quenched-in vacancies, which has been shown to be necessary for the nucleation of β'' [35] in Al-Mg-Si alloys. Therefore two principal assumptions concerning vacancy-solute interactions have to be made:

- i) Co-clusters can contain and release quenched-in vacancies.
- ii) The mobility of quenched-in vacancies depends on their interaction with solute atoms.

Assumption (i) has been previously described in [3] as the so-called “vacancy-prison mechanism” and explains the influence of long-term natural pre-aging on artificial aging of AA6061 via the concentration of mobile vacancies, which is determined by a temperature-dependent dissolution of co-clusters associated with the release of imprisoned quenched-in vacancies. Assumption (ii) is somehow comparable to the ‘temporarily stabilization’ of vacancies used in [3] explaining a retarded annihilation. For the current discussion this concept is used in a more general way.

Although the exact binding energy of Mg and Si with vacancies is still under discussion [36] an association tendency of vacancies with Mg atoms during natural aging has been shown by positron annihilation lifetime spectroscopy (PALS) [19,37,38]. Furthermore, it has been found that the annihilation of quenched-in vacancies is prevented by Mg in aluminum at room temperature and delayed at temperatures above 100 °C [39,40]. In general lattice sites next to attractive solute atoms are energetically preferential for quenched-in vacancies whereby the formation of vacancy-solute pairs or complexes is promoted [41]. Note that also in the equilibrium state solute-vacancy complexes, at least as pairs, exist if attractive interactions to solute atoms are present [42]. Banhart *et al.* [1,2] reported that an association tendency of vacancies and solute within the first few minutes of natural aging or even during quenching is very likely in Al-Mg-Si alloys. In such constellation, solute atoms can either change their lattice sites with the vacancy, or matrix atoms jump into the vacancy around the solute atom, which leads to a preferential movement of the vacancy around the solute atom. Compared to pure metals, jumps are therefore not longer random. From this non-random walk it is evident that

the statistical length which a quenched-in vacancy can move to an annihilation sink is reduced, and annihilation is retarded. Consequently, annihilation depends on the chemical composition, assuming a similar number density of annihilation sites such as free surface, grain boundaries and dislocations [43].

5.4.1 AA6060

Intermediate long-term natural aging (B2) shifted the hardness curve, obtained by artificial aging at 170 °C, to higher values (figure 5.3a). This can be explained by the contribution of co-clusters, slowly dissolving at this temperature. Note that the difference in the hardness is constant over a long period and reduces just in late stages of aging. Due to slow but similar kinetics found for B1 and B2 (figure 5.3a), the precipitation process during artificial aging is assumed to be controlled by the same mechanisms. For artificial aging at 250 °C a rapid reversion took place for B2. Thereafter, both heat treatment procedures exhibited similar kinetics and just small differences in the hardness (figure 5.4a). The fact that the precipitation process including nucleation (simplified here as the initial period until the hardness starts to increase) and growth is accelerated with rising temperature can be easily explained by thermally activated diffusion (increasing equilibrium concentration of vacancies) in a super-saturated solid solution with large undercooling [44]. In contrast to AA6061 [3] it is believed that co-clusters in AA6060 contain no vacancies which can be released during B2. Furthermore, a rapid annihilation of quenched-in vacancies during quenching and initial stages of artificial aging according to B1 is supposed. Both can be explained by a low concentration of solute in lean alloys, which provide a low number density of preferential sites for vacancies next to attractive solute atoms (assumption (ii)). Quenched-in vacancies might anneal out during natural aging for B2 or before the critical size for the nucleation of β'' is reached in the case of B1. Conclusively, the precipitation process in AA6060 is governed by the same concentration of vacancies near the equilibrium for B1 and B2, which is in good accordance with thermally activated diffusion controlling the precipitation reaction.

5.4.2 AA6061

The influence of natural aging on artificial aging of AA6061 has been already explained in [3] by the temperature-dependent release of imprisoned quenched-in vacancies from co-clusters. Anyhow, it is necessary to make some remarks to get a complete picture of Al-Mg-Si alloys including lean alloy. For heat treatment procedure B2, co-clusters act as ‘prisons’ for quenched-in vacancies at 170 °C artificial aging temperature and therefore strongly retard the precipitation process. Note that kinetics is just slightly faster as for B1 and B2 of AA6060 (figure 5.3). At 250 °C imprisoned quenched-in vacancies are released from dissolving co-

clusters and precipitation kinetics is enhanced. Note that for B2, kinetics (especially the nucleation time) is much stronger accelerated than for the alloy AA6060 by rising the temperature. The fast kinetics found at 170 °C for AA6061 according to B1 has been attributed to a high concentration of quenched-in vacancies [3]. Because they are essential for the nucleation of β'' [35], the critical size of nuclei must be reached before most quenched-in vacancies have been annealed out. This can be easily understood applying assumption (ii) to rich alloys with a high number density of preferential lattice sites for vacancies. A further indication of the importance of quenched-in vacancies during initial stages at 170 °C for B1 is that the nucleation time does not significantly differ for B1 at 170 °C and 250 °C and is in the same range as for AA6060 at 250 °C. A decreasing time to peak hardness with rising temperature for B1 can be explained by the fact that thermally activated diffusion is getting dominant after annihilation has finished.

5.5 Conclusions

The objective of this study was to shed more light on the influence of co-clusters formed during long-term natural aging on artificial aging at common and high temperatures for the two principal types of Al-Mg-Si alloys.

- In lean alloys, artificial aging is controlled by thermally activated diffusion, independently of the thermal history. After natural pre-aging, slowly dissolving vacancy free co-clusters contribute to the hardness at common artificial aging temperatures which has been previously called the ‘positive’ influence.
- In the case of rich alloys and natural pre-aging, artificial aging is controlled by a temperature dependent dissolution of co-clusters and a concurrent release of imprisoned vacancies [3]. The enhanced kinetics at common artificial aging temperatures for direct aging can be explained by quenched-in vacancies, which contribute to the nucleation before they anneal out.

Acknowledgment

The authors gratefully thank the people at AMAG Rolling for the fruitful discussion and providing the alloys. Furthermore we want to thank the Austrian Research Promotion Agency (FFG) and AMAG Rolling for the financial support of this work.

References

- [1] Banhart J, Lay MDH, Chang CST, Hill AJ. *Phys Rev B* 2011;83:art. no. 014101.
- [2] Banhart J, Chang CST, Liang ZQ, Wanderka N, Lay MDH, Hill AJ. *Advanced Engineering Materials* 2010;12:559.
- [3] Pogatscher S, Antrekowitsch H, Leitner H, Ebner T, Uggowitzer PJ. *Acta Mater* 2011;59:3352.
- [4] Ostermann F. *Anwendungstechnologie Aluminium*. Berlin Heidelberg New York: Springer-Verlag; 2007.
- [5] Brenner P, Kostron H. *Z Metall* 1939;4:89.
- [6] Borchers H, Kainz M. *Metall* 1963;17:400.
- [7] Kovacs I, Nagy E, Lendvai J. *Acta Metall* 1972;20:975.
- [8] Ried A, Schwellinger P, Bichsel H. *Aluminium* 1977;53:595.
- [9] Chang CST, Wieler I, Wanderka N, Banhart J. *Ultramicroscopy* 2009;109:585.
- [10] Zhuang L, Janse JE, De Smet P, Chen JH, Zandbergen HW. In: Das SK, Kaufman JG, Lienert TJ, editors. *Aluminum 2001*. Warrendale (PA): TMS; 2001. p. 77.
- [11] Roset J, Stene T, Saeter JA, Reiso O. *Mater Sci Forum* 2006;519-521:239.
- [12] Bryant JD. *Metall Mater Trans A* 1999;30:1999.
- [13] Saga M, Sasaki Y, Kikuchi M, Yan Z, Matsuo M. *Aluminium Alloys: Their Physical and Mechanical Properties* 1996;217:821.
- [14] Slámová M, Janecek M, Cieslar M, Šíma V. *Mater Sci Forum* 2007;567-568:333.
- [15] Ou BL, Shen CH. *Scand J Metall* 2005;34:318.
- [16] Edwards GA, Stiller K, Dunlop GL, Couper MJ. *Acta Mater* 1998;46:3893.
- [17] De Geuser F, Lefebvre W, Blavette D. *Phil Mag Lett* 2006;86:227.
- [18] Murayama M, Hono K, Saga M, Kikuchi M. *Mater Sci Eng A* 1998;250:127.
- [19] Seyedrezai H, Grebennikov D, Mascher P, Zurob HS. *Mater Sci Eng A* 2009;525:186.
- [20] van Huis MA, Chen JH, Sluiter MHF, Zandbergen HW. *Acta Mater* 2007;55:2183.
- [21] van Huis MA, Chen JH, Zandbergen HW, Sluiter MHF. *Acta Mater* 2006;54:2945.

-
- [22] Buha J, Lumley RN, Crosky AG, Hono K. *Acta Mater* 2007;55:3015.
- [23] Murayama M, Hono K. *Acta Mater* 1999;47:1537.
- [24] Esmaeili S, Vaumousse D, Zandbergen MW, Poole WJ, Cerezo A, Lloyd DJ. *Phil Mag* 2007;87:3797.
- [25] Anderson SJ, Zandbergen HW, Jansen JE, Taeholt C, Tundal U, Reiso O. *Acta Mater* 1998;46:3283.
- [26] Zandbergen HW, Andersen SJ, Jansen J. *Science* 1997;277:1221.
- [27] Vissers R, van Huis MA, Jansen J, Zandbergen HW, Marioara CD, Andersen SJ. *Acta Mater* 2007;55:3815.
- [28] Massardier V, Epicier T, Merle P. *Acta Mater* 2000;48:2911.
- [29] Dumolt SD, Laughlin DE, Williams JC. *Scripta Metallurgica* 1984;18:1347.
- [30] Ravi C, Wolverson C. *Acta Mater* 2004;52:4213.
- [31] Huppert-Schemme G. *AlMgSi-Bleche für den Fahrzeugbau – Metallkunde und Fertigungstechnik*. Düsseldorf: Aluminium-Verlag; 1997.
- [32] Esmaeili S, Lloyd DJ, Poole WJ. *Acta Mater* 2003;51:2243.
- [33] Shercliff HR, Ashby MF. *Acta Metall Mater* 1990;38:1789.
- [34] Esmaeili S, Lloyd DJ, Poole WJ. *Acta Mater* 2003;51:3467.
- [35] Pogatscher S, Antrekowitsch H, Leitner H, Pöschmann D, Zhang Z, Uggowitzer PJ. Influence of Interrupted Quenching on Artificial Aging of Al-Mg-Si Alloys. to be published.
- [36] Wolverson C. *Acta Mater* 2007;55:5867.
- [37] Dupasquier A, Kögel G, Somoza A. *Acta Mater* 2004;52:4707.
- [38] Buha J, Muramatsu T, Lumley RN, Crosky AG, Hillel AJ. *Mater Forum* 2004;28:1028.
- [39] Panseri C, Federighi T, Ceresara S. *Trans Metall Soc AIME* 1963;227:1122.
- [40] Panseri C, Gatto FG, Federighi T. *Acta Metall* 1958;6:198.
- [41] Zurob HS, Seyedrezai H. *Scr Mater* 2009;61:141.
- [42] Takamura J, Koike M, Furukawa K. *J Nucl Mater* 1978;69-70:738.
- [43] Fischer FD, Svoboda J, Appel F, Kozeschnik E. *Acta Mater* 2011;59:3463.
- [44] Liu F, Sommer F, Bos C, Mittemeijer EJ. *International Materials Reviews* 2007;52:193.

6 COMPOSITION II

The previous chapter addressed the two extreme cases such as AA6061, exhibiting the negative effect of natural pre-aging, and AA6060, showing the positive effect of natural pre-aging. In chapter 6 a more detailed look is made to the interdependence of the solute super-saturation and the effects of natural pre-aging on artificial aging for the alloy AA6061, for which natural pre-aging is much more important from an industrial point of view. The effect of a compositional variation of a variety of alloying elements is studied by thermodynamic calculations and an analysis of yield strength data of several model alloys.

Interdependent Effect of Chemical Composition and Thermal History on Artificial Aging of AA6061*

In this study the interdependent effect of chemical composition and thermal history on artificial aging was investigated for the aluminum alloy AA6061. Based on thermodynamic calculations, including Al, Fe, Cr, Zn, Ti, Mg, Si and Cu, model alloys exhibiting a maximum variation of the reachable solute super-saturation of elements relevant for precipitation hardening within the compositional limits of AA6061 were produced. The artificial aging behavior of these alloys at 175 °C was studied by tensile testing for two thermal histories, including very short and long-term room temperature storage after quenching. Precipitation during artificial aging was investigated by an analysis of yield strength data. As generally expected, precipitation kinetics was found to depend strongly on the solute super-saturation in the case of very short room temperature storage. For artificial aging after long-term room temperature storage the kinetics showed almost no dependence on the chemical composition. This seems to be an exception from simple precipitation kinetics and can be explained based on the complex role of quenched-in vacancies in artificial aging of AA6061.

6.1 Introduction

The aluminum alloy AA6061 is a well-known member of the Al-Mg-Si alloy family [1]. It is widely used in the building, transportation, industrial and aerospace markets, and is produced as sheets, plates, forgings and extrusions [2]. Due to its high ratio of strength to density, good corrosion resistance, excellent surface properties and weldability, together with its relatively low price [3], AA6061 is very attractive commercially and has become a workhorse among age hardenable aluminum alloys. For most applications, Al-Mg-Si alloys undergo an artificial aging procedure. Although aging of Al-Mg-Si alloys has been studied for the past 85 years [4], some questions, however, remain unresolved. In addition to questions regarding clustering during early stages of aging, the ambiguous influence of room temperature storage after quenching on artificial aging is, in particular, not fully understood today. For AA6061, a strong adverse influence of a longer period of room temperature storage on subsequent artificial aging at common temperatures has been reported [5-9]. This is of considerable importance not only from an academic point of view, but also for industry, because this negative effect strongly influences the production of numerous heat-treated products via a logistically unavoidable intermediate room temperature storage which results in reduced energy efficiency, production

*Pogatscher S, Antrekowitsch H, Uggowitzer PJ. Acta Mater 2012; Submitted

capacity, profitability, and achievable strength. For a well-grounded discussion of the interdependence of the chemical composition of AA6061 and the thermal history for artificial aging, the general precipitation sequence should first be mentioned briefly [10]:

SSSS \rightarrow Cluster formation \rightarrow Mg,Si co-clusters \rightarrow GP-I zones \rightarrow $\beta'' \rightarrow$ B' and $\beta' \rightarrow \beta$.

The early stage of aging (e.g., natural aging during room temperature storage), called 'cluster formation' here, proceeds in several individual stages which are not yet fully resolved [11]. The term 'Mg,Si co-clusters' [10,12-16] has often been used for clusters formed after long-term natural aging, although the denotation is not consistent in the literature. Subsequently formed GP-I zones [17-19] are thermally more stable, contain more solute atoms, and have been observed to form during aging only above room temperature (e.g., in underaged conditions or after pre-aging treatments). The needle-like β'' precipitates are typical for T6-conditions [20,21]. For overaged conditions or high temperature exposure, the rod-shaped phases β' [22] and B' [23] and the platelet-like equilibrium phase β (Mg_2Si) [24,25] have been reported.

We recently showed that the effect of intermediate room temperature storage seems to be linked to a temperature-dependent dissolution of Mg,Si co-clusters, associated with a release of imprisoned quenched-in vacancies. Due to a very slow dissolution of these Mg,Si co-clusters at common artificial aging temperatures [9] and the required availability of quenched-in vacancies for the nucleation of β'' or its directly transformable precursors (GP-I zones) [26], the precipitation process is strongly retarded. A systematic study of the interdependence of the chemical composition and thermal history on artificial aging in the light of the above-mentioned novel "vacancy-prison mechanism" [9] is pending. The present study was performed to clarify the situation for the technologically important alloy AA6061, which can be strongly varied in its composition within the standard (ASTM B-209), and where thermal history is known to be of crucial importance for artificial aging [9]. The nominal composition of AA6061 can be misleading as regards precipitation reactions during artificial aging, because the solute super-saturation of those elements relevant for precipitation hardening is not only influenced by their separate concentration. For example, Fe-containing phases have been shown to consume a significant amount of Si [27,28]. A comprehensive evaluation of the compositional influence (Fe, Cr, Zn, Ti, Mg, Si and Cu) on the maximum reachable solute super-saturation of Mg, Si and Cu in AA6061 is therefore necessary for an appropriate study of the interdependent effects of variations in chemical composition and thermal history on artificial aging of AA6061.

6.2 Experimental methods

Thermodynamic calculations were performed using FactSage™ 6.1 software [29] together with the FACT FTLite light alloy database (2009). The maximum reachable thermodynamic solute super-saturation of Mg, Si and Cu in the FCC-Al matrix was calculated by subtracting the equilibrium concentrations at 570 °C (solution treatment temperature) minus the equilibrium concentrations at 175 °C (artificial aging temperature), and is termed as $MSSS_{570-175}$. Such calculations were performed for all necessary combinations within the limits of the standard for the chemical composition of AA6061 (Mg 0.8-1.2, Si 0.4-0.8, Cu 0.15-0.4, Fe 0-0.7, Cr 0.04-0.35, Zn 0-0.25 and Ti 0-0.15, all in wt%). For optimal design of the compositional combinations (up to 342) and visualization of the effects of individual elements, MODDE™ 7.0 software was used to create regression models for the $MSSS_{570-175}$ of Mg, Si and Cu.

Model alloys were prepared with Al (99.98 wt%) and binary Al–X master alloys (X=Mn, Fe, Cr, and Ti) and pure Cu, Si, Mg and Zn, respectively, as starting materials using an inductive melting furnace from ITG Induktionsanlagen GmbH. Argon gas purging was applied to reduce the hydrogen content before the alloys were cast to slabs. After cutting and homogenization, hot rolling from 25 to 4.2 mm thickness was conducted. For tensile testing, flat bar tension specimens ($a=3$ mm, $b=6$ mm and $l_0=25$ mm) were finally prepared from the plate in the LT direction. To check the chemical composition, optical emission spectrometry (SPECTROMAXx from SPECTRO) was applied during the alloying procedure and to the final plates.

The scheme of the heat treatment procedure, carried out in a circulating air furnace (Nabertherm N60/85 SHA), is shown in figure 6.1. A two-step homogenization process was conducted for 12 h at 500 °C and 12 h at 570 °C. Hot rolling was performed at 550 °C, and solution heat treatment of the flat bar tension specimen was conducted at 570 °C for 20 min. Subsequent quenching was carried out in water at RT, followed by short-term room temperature storage of two minutes (termed ‘B1’) or long-term room temperature storage of two weeks (termed ‘B2’). Artificial aging was then carried out in an oil bath (LAUDA Proline P 26) at 175 °C from 15 s up to 64 h.

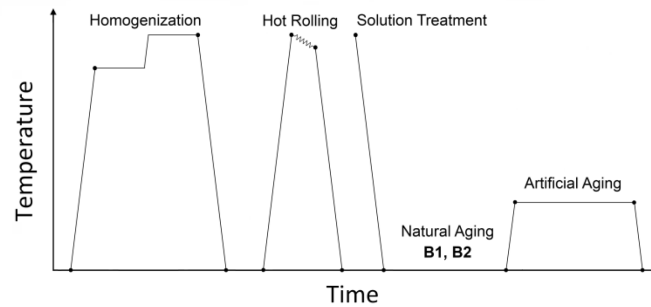


Figure 6.1: Heat treatment scheme

Tensile testing was performed in a Zwick/Roell 100 kN unit in accordance with DIN 50125:2004-01. Three specimens were tested for each condition. A maximum standard deviation of 4.8 MPa was achieved for the yield strength.

6.3 Results

6.3.1 Computational evaluation of the chemical composition

A visualization of the effects of various alloying elements on the maximum reachable thermodynamic solute super-saturations of elements relevant for precipitation hardening was done by a multi-linear regression. Figure 6.2 shows the coefficients of regression models of $MSSS_{570-175}$ for Cu, Mg, Si, and the sum of Mg and Si, obtained by a partial least squares algorithm. To make the coefficients comparable, they were scaled and centered according to the compositional limits of AA6061, such that the variation of every alloying element is between -1 and +1. The size of the coefficients represents the change in the $MSSS_{570-175}$ when the concentration of an alloying element varies from 0 to 1, while the others are kept at their average. The effects of the individual alloying elements and interactions can then be easily deduced from such plots. Evaluated statistical parameters such as R^2 (percentage of the variation of the response explained by the model, explaining how well the model fits the data) and Q^2 (percentage of the variation of the response predicted by the model according to cross-validation, explaining how well the model predicts new data) were also found to be excellent (figure 6.2).

Figure 6.2a shows the influence of the composition on the $MSSS_{570-175}$ of Cu and a 95 % confidence interval of the model. The coefficient of Cu (0.125 wt.%) represents the change in the $MSSS_{570-175}$ of Cu when the scaled and centered concentration of Cu varies from 0 (0.275 wt.%) to 1 (0.4 wt.%). Zn, Mg and Fe fairly increase the $MSSS_{570-175}$ of Cu, while Si causes a

small reduction. A simultaneous adjustment of Mg and Si and Mg and Zn causes an antagonistic influence on the $MSSS_{570-175}$ of Cu, while the interactions of Si and Zn and Fe and Cu produce a synergistic effect. Most of these small influences arise from a slight shift of the calculated solubility limit of Cu at 175 °C, depending on the total composition. An exception to this is Fe, which consumes Al from the matrix by the formation of intermetallic phases and therefore apparently increases the relative amount of the $MSSS_{570-175}$ of Cu. It should be noted that all effects shown are significant, but rather small compared to the obvious influence of the copper content.

From figure 6.2b it can be seen that the $MSSS_{570-175}$ of Mg is strongly influenced by alloying elements. Si shows a huge influence on the maximum solute super-saturation of Mg and a significant interaction with Mg, which is mainly dedicated to the formation of Mg_2Si . In addition, Si and Mg show negative quadratic coefficients, which means a declining influence at rising concentrations. For a low Mg content and appropriate levels of the Si content it is even possible to find a maximum for the $MSSS_{570-175}$ of Mg in between the compositional range of AA6061. The effects of Fe, Cu, Ti and some interaction coefficients are significant but rather small compared to the influence of Mg and Si.

The main effects on the $MSSS_{570-175}$ of Si are shown in figure 6.2c. Fe and Ti exhibit strong, negative effects, which can be easily explained by the formation of intermetallic phases consuming Si. Mg and Mn show significant but rather small negative influences. Numerous interactions are also present, mainly including Fe. Due to the fact that in AA6061 all precipitates consist of Mg and Si, the influences on their added quantity are shown in figure 6.2d, which is then a weighted sum of the individual contributions of Mg and Si (termed Mg+Si in the following sections).

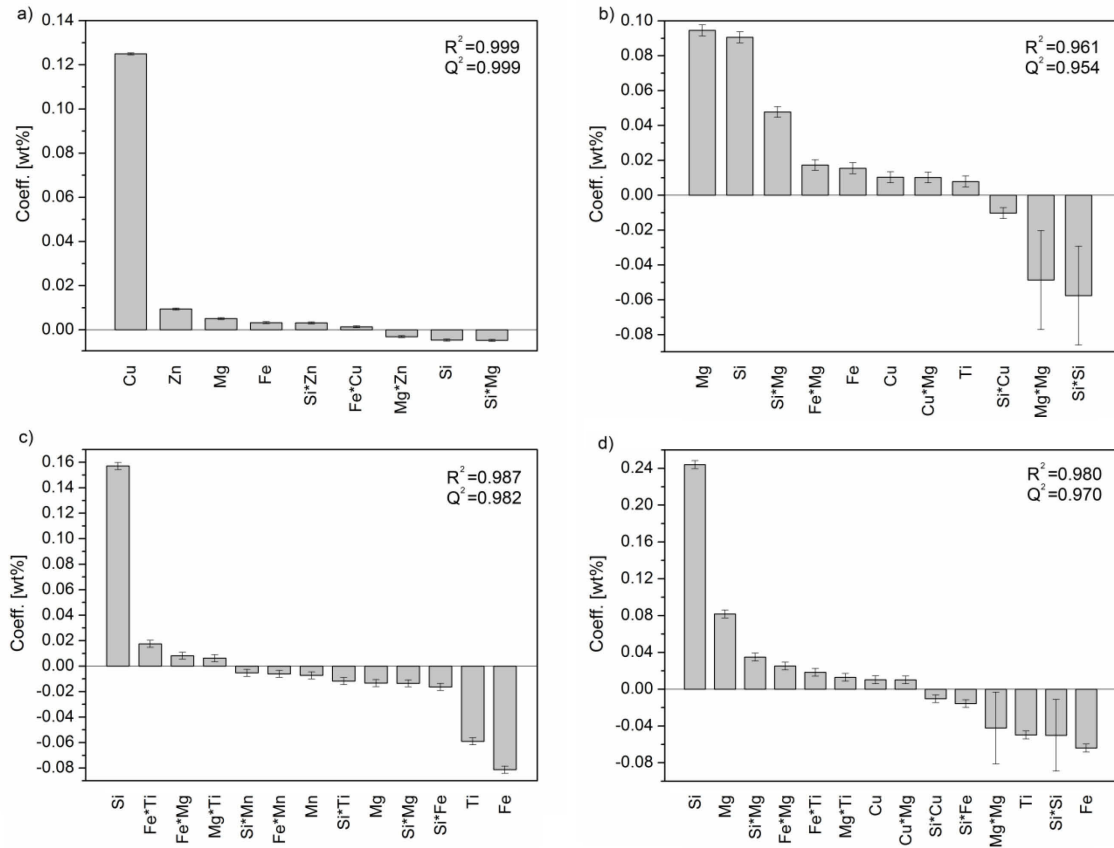


Figure 6.2: Scaled and centered coefficients of the regression models of the MSSS₅₇₀₋₁₇₅ of (a) Cu; (b) Mg; (c) Si; (d) Mg+Si

Besides the Mg and Si content, Ti and Fe were identified to be of significant importance for the MSSS₅₇₀₋₁₇₅ of Mg+Si in the range of 570 °C to 175 °C: see figure 6.2. Figure 6.3 gives quantitative information on their influence. All elements not plotted are fixed in the center of the standardized range of composition of AA6061. It can be seen that the MSSS₅₇₀₋₁₇₅ of Mg+Si can vary from 1.47 to 1.23 wt % without changing the Si or Mg content of AA6061, only by changing the Fe and Ti content within the allowed composition of AA6061.

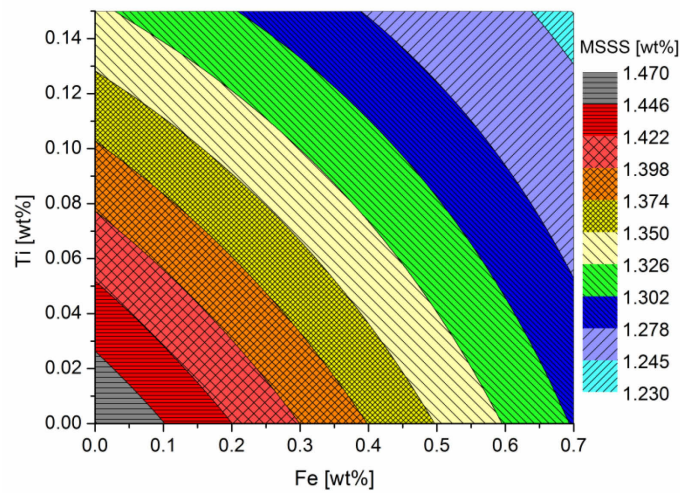


Figure 6.3: Contour plot for the influence of Ti and Fe on the MSSS₅₇₀₋₁₇₅ of Mg+Si

Using figures 6.2 and 6.3, an appropriate selection of the composition of model alloys for a study of the interdependent effect between a variation of the chemical composition and the thermal history for artificial aging of AA6061 was carried out. Table 6.1 shows the measured composition of the model alloys produced and the calculated MSSS₅₇₀₋₁₇₅ of Mg+Si and Cu. The alloy ‘Mean’ was produced as a reference where all elements were fixed in the center of the standardized range of composition of AA6061. ‘Low_{Mg+Si}’ and ‘High_{Mg+Si}’ mark the minimal and maximal values for the MSSS₅₇₀₋₁₇₅ of Mg+Si in the standardized range of composition for AA6061. Cu, also directly involved in aging, was kept at a constant value. The alloys ‘Mean_{High Fe Ti}’ and ‘Mean_{Low Fe Ti}’ were produced to show the influence of Fe and Ti as expected from figure 6.3. The effect of Cu was taken into account by the two alloys ‘Mean_{Low Cu}’ and ‘Mean_{High Cu}’, which are similar to the alloy ‘Mean’ except for a variation in the Cu content.

Table 6.1: Measured composition of the model alloys and calculated vales of the MSSS₅₇₀₋₁₇₅ of Mg+Si and Cu

Alloy	Elements [wt.%]									MSSS ₅₇₀₋₁₇₅ [wt%]	
	Al	Si	Fe	Cu	Mn	Mg	Cr	Zn	Ti	Mg+Si	Cu
Low _{MgSi}	Bal.	0.41	0.73	0.28	0.08	0.78	0.20	0.13	0.17	0.89	0.24
Mean	Bal.	0.58	0.35	0.27	0.07	0.95	0.20	0.12	0.10	1.24	0.22
High _{MgSi}	Bal.	0.78	0.05	0.28	0.08	1.17	0.21	0.13	0.00	1.63	0.23
Mean _{High Fe Ti}	Bal.	0.59	0.78	0.28	0.08	0.91	0.21	0.13	0.17	1.05	0.24
Mean _{Low Fe Ti}	Bal.	0.56	0.08	0.26	0.08	0.95	0.20	0.12	0.00	1.41	0.21
Mean _{Low Cu}	Bal.	0.58	0.37	0.14	0.08	0.95	0.21	0.13	0.09	1.24	0.10
Mean _{High Cu}	Bal.	0.58	0.35	0.38	0.07	0.95	0.24	0.12	0.11	1.23	0.32

6.3.2 Artificial aging

The evolution of the yield strength of the model alloys during artificial aging at 175 °C after intermediate storage at room temperature of two minutes (B1) is shown in figure 6.4. A remarkable influence of a variation in the chemical composition within the standardized range of AA6061 according to the model alloys of table 6.1 can be observed for B1. Figure 6.4a reveals that the kinetics of artificial aging and the yield strength in T6-condition are strongly dependent on the $MSSS_{570-175}$ of Mg+Si ($Low_{Mg+Si} < Mean_{High\ Fe\ Ti} < Mean < Mean_{Low\ Fe\ Ti} < High_{Mg+Si}$). A variation of the $MSSS_{570-175}$ of Cu within the limits of AA6061 was found to show a significant but smaller influence in figure 6.4b ($Mean_{Low\ Cu} < Mean < Mean_{High\ Cu}$).

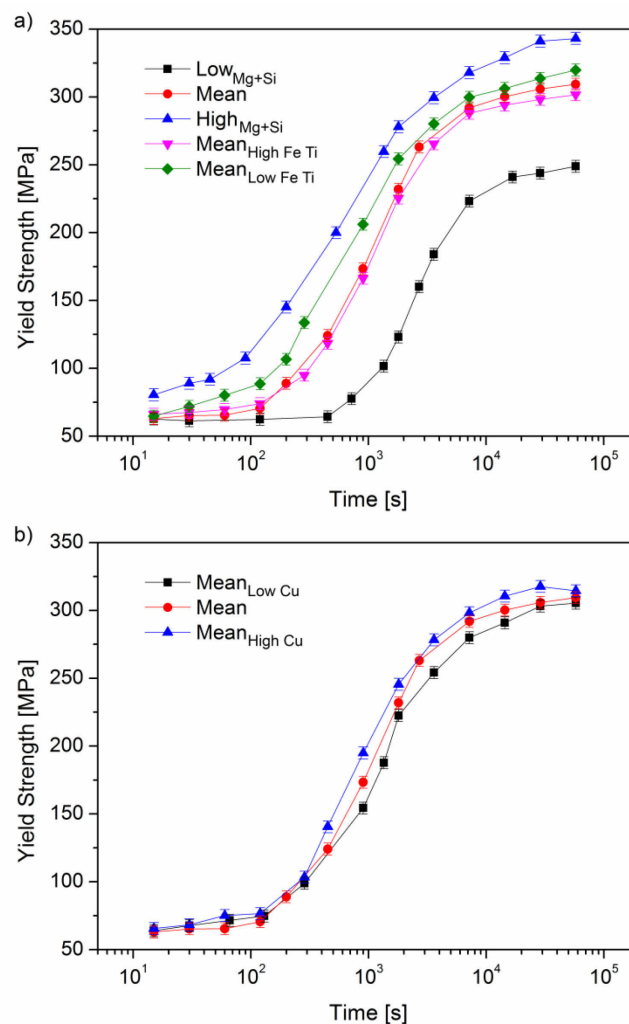


Figure 6.4: Evolution of the yield strength during artificial aging at 175 °C according to heat treatment procedure B1 for a variation in the $MSSS_{570-175}$ of (a) Mg+Si and (b) Cu

Figure 6.5 shows the evolution of the yield strength of the model alloys during artificial aging at 175 °C after intermediate storage at room temperature for two weeks (B2). The influence of

varying the chemical composition within the standardized range for AA6061 was found to be different for B2 compared to B1. From figure 6.5a it can be seen that the yield strength in T6-condition shows a similar but smaller variation for the model alloys. Interestingly, the kinetics of artificial aging seems not to be significantly influenced by varying the MSSS₅₇₀₋₁₇₅ of Mg+Si. Varying the MSSS₅₇₀₋₁₇₅ of Cu within the limits of AA6061 also caused a similar behavior (figure 6.5b).

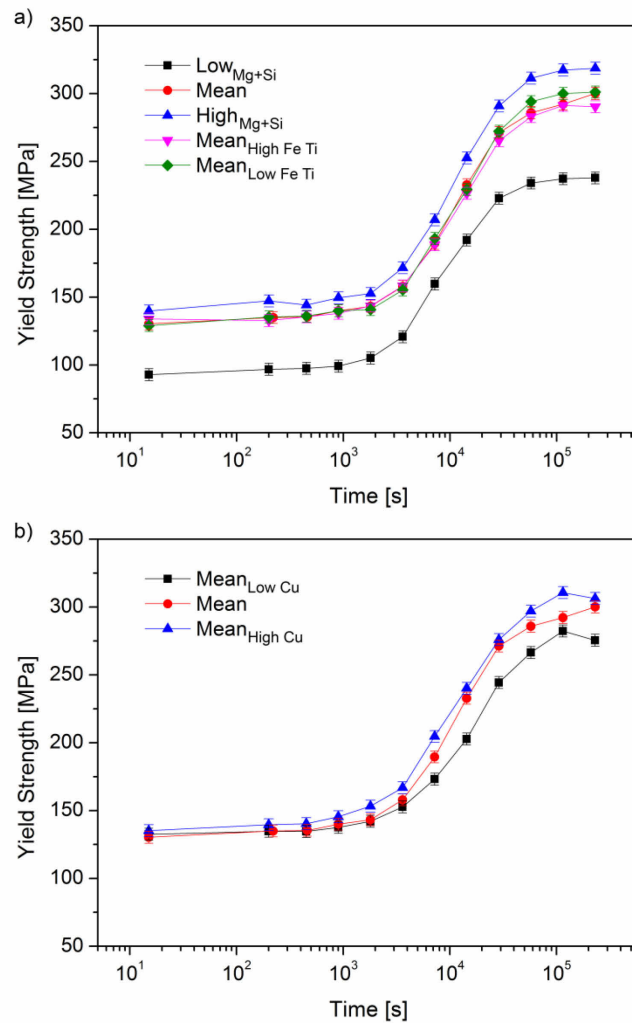


Figure 6.5: Evolution of the yield strength during artificial aging at 175 °C according to heat treatment procedure B2 for a variation in the MSSS₅₇₀₋₁₇₅ of (a) Mg+Si and (b) Cu

6.4 Yield strength analysis

A simple analysis of yield strength data was performed to examine in more detail the dependence of precipitation kinetics during artificial aging of the model alloys for both thermal

histories. The yield strength of precipitation-hardened aluminum alloys can be described according to equation (6.1) by a sum of the intrinsic strength of aluminum (σ_i), the contribution of the solid solution (σ_{ss}) and precipitation hardening (σ_{ppt}) [30,31].

$$\sigma = \sigma_i + \sigma_{ss} + \sigma_{ppt} \quad (6.1)$$

For artificial aging according to B1, the evolution of the individual contributions of the yield strength can be described as follows. The contribution of the solid solution σ_{ss}^{aa} is given by equation (6.2), where σ_{aq} is the as quenched yield strength and f_r^{aa} describes the relative volume fraction of precipitates formed during artificial aging ($f_r^{aa} = 1$ in T6-condition). α_{aa} is the fraction of the initial solute concentration depleted from the matrix when peak-aged conditions are reached [32] and was set to 0.5, which accords well with the quantity measured by atom probe tomography by our group [26].

$$\sigma_{ss}^{aa} = (\sigma_{aq} - \sigma_i) \cdot (1 - \alpha_{aa} \cdot f_r^{aa})^{\frac{2}{3}} \quad (6.2)$$

All precipitates are assumed to be shearable. Thus, the contribution of precipitates formed during artificial aging to the yield strength (σ_{aa}) can be expressed as a function of f_r^{aa} by equation (6.3) [30-32]. The constant C_{aa} can be derived from the yield strength in T6-condition by subtracting σ_i and σ_{ss}^{aa} in T6-condition.

$$\sigma_{aa} = C_{aa} \cdot (f_r^{aa})^{\frac{1}{2}} \quad (6.3)$$

For a description of the evolution of the individual contributions of the yield strength for artificial aging according to B2, an additional contribution of Mg,Si co-clusters formed during natural aging has to be considered. According to [31] the coexistence of the contributions σ_{aa} and σ_{na} can be most accurately described by a Pythagorean superposition (equation (6.4)).

$$\sigma_{aa+na} = (\sigma_{aa}^2 + \sigma_{na}^2)^{\frac{1}{2}} \quad (6.4)$$

The contribution of Mg,Si co-clusters, formed during natural aging and dissolved during artificial aging, to the yield strength (σ_{na}) can be expressed as a function of their relative volume fraction f_r^{na} by equation (6.5) [31].

$$\sigma_{na} = C_{na} \cdot (f_r^{na})^{\frac{1}{2}} \quad (6.5)$$

For B2, the contribution of the solid solution σ_{ss}^{na} during artificial aging has to take into account the dissolution of Mg,Si co-clusters (which increases the solid solution) and precipitation during artificial aging (which decreases the solid solution). This can be achieved by equation (6.6), where α_{na} is the fraction of the initial solute concentration which is depleted from the matrix after long-term natural aging. α_{na} was estimated to be 0.1, which is in good accordance with the quantity measured by atom probe tomography for early stages of aging of AA6061 [26]. The constant C_{na} of equation (6.5) can then be found by subtracting σ_i and σ_{ss}^{na} after long-term natural aging (T4) from the total yield strength at T4.

$$\sigma_{ss}^{na} = \left[(\sigma_{aq} - \sigma_i) \cdot (1 - \alpha_{na} \cdot f_r^{na})^{\frac{2}{3}} \right] \cdot (1 - \alpha_{aa} \cdot f_r^{aa})^{\frac{2}{3}} \quad (6.6)$$

The evolution of f_r^{na} during the dissolution of Mg,Si co-clusters through artificial aging can be expressed using equation (6.7). It comprises the results of a mathematical model for a diffusion-controlled solution of a second phase in an infinite matrix and some approximations and is just valid for $t < B^{-2}$ [31]. B is a temperature-dependent factor which has been shown to not be influenced by the composition of Al-Mg-Si alloys [33] and is estimated to be $3 \cdot 10^3 \text{ s}^{-0.5}$ [31,33].

$$f_r^{na} = \left(1 - B \cdot t^{\frac{1}{2}} \right)^3 \quad (6.7)$$

For a simple description of the kinetics of the precipitation process during artificial aging, a Johnson-Mehl-Avrami-Kolmogorov-like equation (equation (6.8)) was used [31]. n was fixed at a value of 1.35, which was found to be optimal for describing the artificial aging curves studied. Note that this is purely a mathematical model and n does not cover the physically-based background here [31].

$$f_r^{aa} = 1 - \exp(-k \cdot t^n) \quad (6.8)$$

Figure 6.6 shows the results of a fitting procedure of the yield strength curves of figures 6.4 and 5 to equation (6.1), using a least squares algorithm. The fitted curves are compared to experimental values. The simple model, using only the rate constant k as the sole variable

parameter determining the kinetics, facilitates quite acceptable results, such that all fitted curves exhibit an R^2 value greater than 0.98.

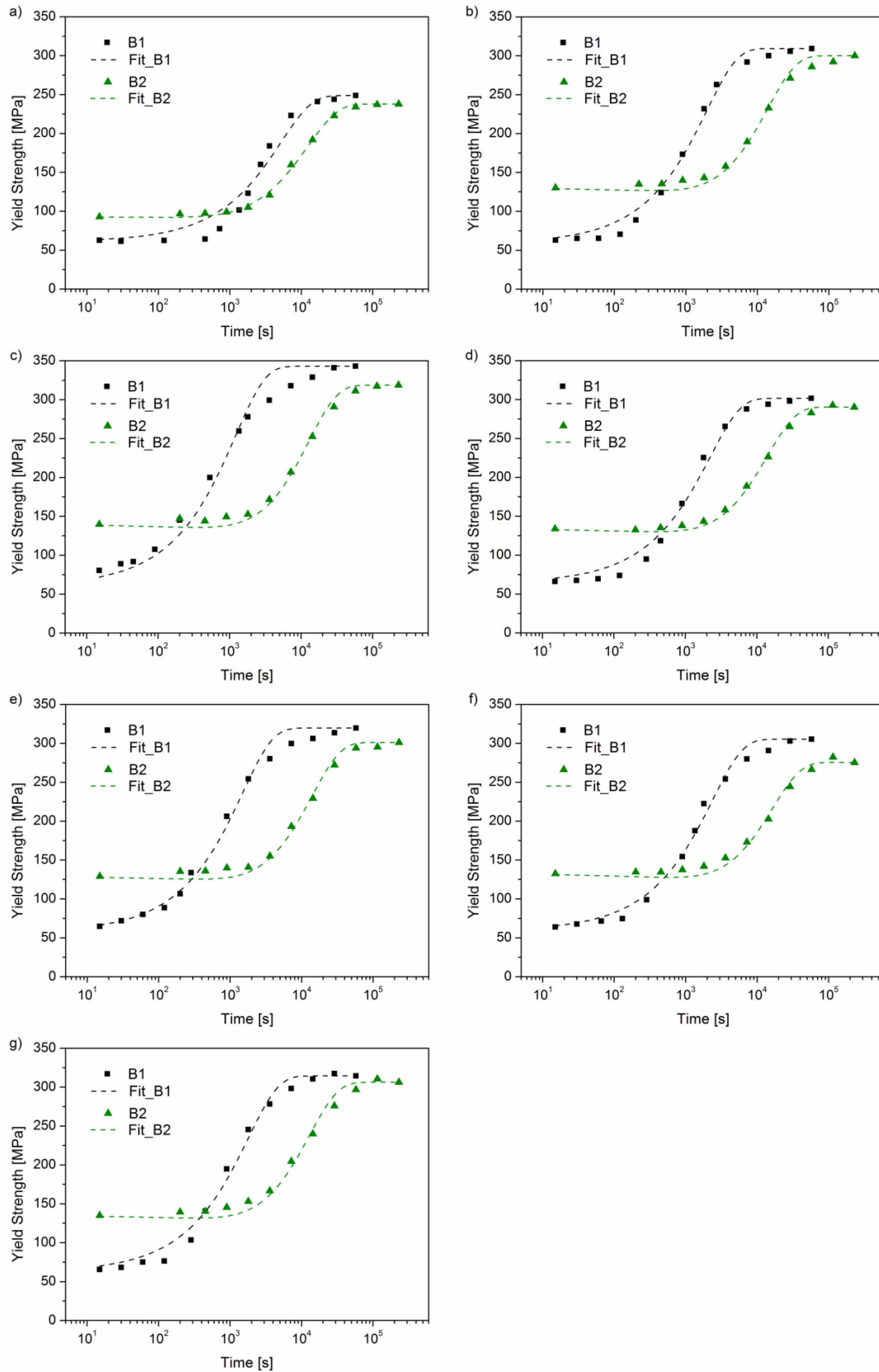


Figure 6.6: Results of the fitting procedure of the yield strength evolution during artificial aging according to B1 and B2 for the alloys (a) $\text{Low}_{\text{Mg+Si}}$; (b) Mean; (c) $\text{High}_{\text{Mg+Si}}$; (d) $\text{Mean}_{\text{High Fe Ti}}$; (e) $\text{Mean}_{\text{Low Fe Ti}}$; (f) $\text{Mean}_{\text{Low Cu}}$; and (g) $\text{Mean}_{\text{High Cu}}$

The dependence of the calculated rate constants k on the maximum solid super-saturation $MSSS_{570-175}$ of Mg+Si and Cu for B1 and B2 is shown in figure 6.7. For B1 k increases with $MSSS_{570-175}$ within the range of AA6061 by nearly one order of magnitude, while in the case of B2 k seems to be nearly insensitive to a variation of the $MSSS_{570-175}$ and is stable at a very low value (figure 6.7a). The influence of varying the Fe and Ti content within the allowed composition of AA6061 for a constant Mg and Si content on the kinetics is also shown in figure 6.7a. The effect of varying the $MSSS_{570-175}$ of Cu within the range of AA6061 on k is less than that of varying the $MSSS_{570-175}$ of Mg+Si within the limits of AA6061, but the principal behavior is very similar (figure 6.7b).

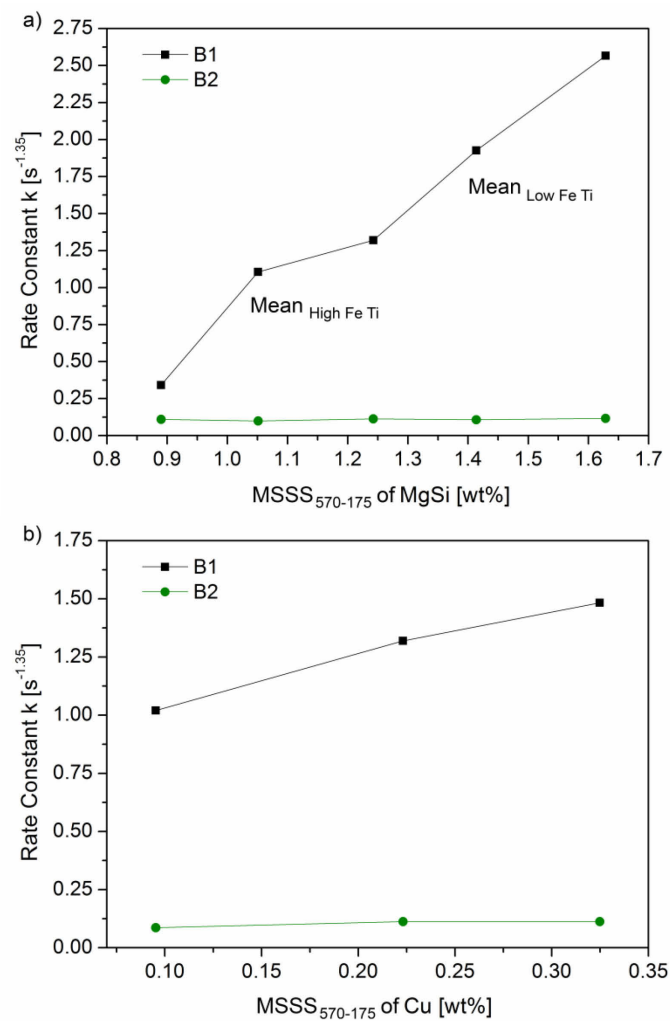


Figure 6.7: Dependence of the rate constant k on the (a) $MSSS_{570-175}$ of Mg+Si and (b) $MSSS_{570-175}$ of Cu for B1 and B2

6.5 Discussion

Variations in chemical composition in industrially produced alloys can always be present due to variations in production or unavoidable macro segregations which evolve during casting. Composition may also be altered in some cases by unidirectional alloy development strategies. In the past, little attention was paid to the impact of such small variations on the hardening kinetics of various semi-finished products artificially aged after a longer period of room temperature storage subsequent to quenching (e.g. plates). In recent years, tremendous efforts, mostly involving new heat treatment strategies [5-9], have been made to avoid the strong adverse influence of such room temperature storage on subsequent artificial aging for Al-Mg-Si alloys. In the present study, the interdependency of a variation in the chemical composition within the limits of AA6061 and the thermal history and their effect on artificial aging was investigated. Thermodynamic calculations showed that the maximum reachable solute super-saturation of elements relevant for precipitation hardening within the compositional limits of AA6061 depend not only on their own concentration but also on the overall chemical composition. Beside some small effects, Fe and Ti in particular were found to reduce the $MSSS_{570-175}$ of Si. The $MSSS_{570-175}$ of Cu barely depends on other alloying elements (figure 6.2). Model alloys exhibiting a maximum variation in the $MSSS_{570-175}$ of elements relevant for precipitation hardening within the limit of AA6061, and such showing the influence of Fe and Ti (table 6.1), were investigated via an analysis of the yield strength evolution during artificial aging (figure 6.4-6.7). As expected from the thermodynamic calculations, the alloys $Mean_{Low\ Fe\ Ti}$, $Mean$ and $Mean_{High\ Fe\ Ti}$, all exhibiting the same Mg, Si and Cu concentration, showed significant differences in the artificial aging behavior which are linked to the effect of Fe and Ti. In general, the T6 yield strength increased on the raising of the amount of solute super-saturated elements relevant for precipitation hardening. This is not unexpected and can be explained by the larger absolute volume fraction of precipitates formed [30]. The smaller T6 yield strength for B2 is attributed to a coarser distribution of precipitates for artificial aging after intermediate long-term natural aging [9,34]. As one would first assume, precipitation kinetics was found to depend strongly on the solute super-saturation in the case of B1 (figure 6.7a and b). For artificial aging according to B2, kinetics showed nearly no dependence on the chemical composition (figure 6.7a and b). In the light of these findings it is understandable why small variations in chemical composition attracted little attention in the past in industrial processing, which often incorporates intermediate long-term room temperature storage (B2). For increasingly used variants of direct aging (e.g. B1) the chemical composition was found to be of much more importance for artificial aging of AA6061. Although the effect of natural aging has been studied extensively, the totally different dependence of artificial aging kinetics

on the $MSSS_{570-175}$ for diverse thermal histories has not been reported previously and seems to be an exception from simple diffusion-controlled precipitation kinetics driven by the solute super-saturation. In the following section, the interdependence effect of the chemical composition and thermal history is explained, taking into account classic approaches for nucleation and growth of precipitates [35,36] and the complex role of quenched-in vacancies during artificial aging of AA6061 [9,26].

The nucleation rate of diffusional transformations in solids (e.g. precipitation) is governed by atomic mobility and a critical energy barrier, which shows an inverse quadratic relationship to the driving force directly related to the solute super-saturation [35]. A high solute super-saturation therefore generates a low energy barrier for nucleation. For diffusion-controlled growth, the growth rate also depends on the atomic mobility and the driving force linked to the solute super-saturation [35]. From this point of view, overall precipitating kinetics should therefore increase with an increasing solute super-saturation, as was found for B1 (figure 6.7). According to this classic approach atomic mobility is normally considered to be constant [35], which is an incorrect assumption in the case of artificial aging of Al-Mg-Si alloys, because annihilation of quenched-in vacancies during the initial period of artificial aging according to B1 drastically alters the atomic mobility. Note that the annihilation time is expected to be in the range of a few minutes if we apply the annihilation model of Fischer *et al.* [37]. Considering our recent results [26], which showed that quenched-in vacancies are essential for the nucleation of β'' , the interplay of the lifetime of quenched-in vacancies and nucleation in alloys exhibiting different solute super-saturations also has to be taken into account. In alloys containing a low concentration of super-saturated solute atoms fewer nuclei of β'' are able to form than in rich alloys before most quenched-in vacancies have been annealed out. The lifetime of quenched-in vacancies is also expected to rise with an increasing content of solute atoms, which are correlated to quenched-in vacancies in Al-Mg-Si alloys [9,33], although this effect currently lacks quantification. However, the interplay of the solute super-saturation and the behavior of quenched-in vacancies seems to be crucially important for the nucleation during artificial aging according to B1, and also leads to the dependence of precipitation kinetics, as was found from the analysis of the yield strength data (figure 6.7).

For artificial aging according to B2, the astonishing insensitivity of precipitation kinetics to the solute super-saturation (figure 6.7) can be explained if we take into account the findings in [9,33]. Thereafter the effect of intermediate long-term room temperature storage of AA6061 is linked to a temperature-dependent dissolution of Mg,Si co-clusters formed during natural aging, associated with a release of imprisoned quenched-in vacancies. Due to the very slow dissolution of these Mg,Si co-clusters at common artificial aging temperatures [9] and the required availability of quenched-in vacancies for the nucleation of β'' [26] the precipitation

process is strongly retarded; this is called the “vacancy-prison mechanism” [9]. Such extremely slow kinetics was found for B2 in the present work (figure 6.7). The dissolution behavior of Mg,Si co-clusters has been shown to be similar for lean and rich Al-Mg-Si alloys and is not significantly influenced by the composition [33]. This then explains the insensitivity of the slow precipitation kinetics to the solute super-saturation for B2: the associated release behavior of quenched-in vacancies, which has been shown to control the precipitation kinetics of AA6061 [9], is also similar for different solute super-saturations.

6.6 Conclusions

The objective of this study was to investigate the interdependent effects of variations in chemical composition and thermal history for artificial aging of AA6061.

- Precipitation kinetics is almost independent of chemical composition when artificial aging is applied after long-term room temperature storage, while in the case of very short room temperature storage the kinetics is strongly dependent on the solute super-saturation.
- Small variations in the total chemical composition including elements not directly related to precipitation hardening (Fe and Ti) therefore cause significant differences in artificial aging kinetics when novel direct aging methods are applied.
- Overall, the unexpected interdependent effect of the chemical composition and thermal history on precipitation kinetics of AA6061 can be explained well by the complex role of quenched-in vacancies during artificial aging.

Acknowledgments

The authors gratefully thank the people at AMAG Rolling, especially Thomas Ebner, for the fruitful discussion. We are also grateful to the Austrian Research Promotion Agency (FFG) and AMAG Rolling for financial support of this work.

References

- [1] Ostermann F. Anwendungstechnologie aluminium. Berlin: Springer-Verlag; 2007.
- [2] Dorward RC, Bouvier C. Mater Sci Eng A 1998;254:33.
- [3] Marioara CD, Andersen SJ, Jansen JE, Zandbergen HW. Acta Mater 2003;51:789.
- [4] Archer RS, Jeffries Z. Trans AIME 1925;71:828.
- [5] Brenner P, Kostron H. Z Metall 1939;4:89.
- [6] Borchers H, Kainz M. Metall 1963;17:400.
- [7] Kovacs I, Nagy E, Lendvai J. Acta Metall 1972;20:975.
- [8] Ried A, Schwellinger P, Bichsel H. Aluminium 1977;53:595.
- [9] Pogatscher S, Antrekowitsch H, Leitner H, Ebner T, Uggowitzer PJ. Acta Mater 2011;59:3352.
- [10] Edwards GA, Stiller K, Dunlop GL, Couper MJ. Acta Mater 1998;46:3893.
- [11] Banhart J, Lay MDH, Chang CST, Hill AJ. Phys Rev B 2011;83:art. no. 014101--.
- [12] Banhart J, Chang CST, Liang ZQ, Wanderka N, Lay MDH, Hill AJ. Adv Eng Mater 2010;12:559.
- [13] Chang CST, Wieler I, Wanderka N, Banhart J. Ultramicroscopy 2009;109:585.
- [14] De Geuser F, Lefebvre W, Blavette D. Phil Mag Lett 2006;86:227.
- [15] Murayama M, Hono K, Saga M, Kikuchi M. Mater Sci Eng A 1998;250:127.
- [16] Seyedrezai H, Grebennikov D, Mascher P, Zurob HS. Mater Sci Eng A 2009;525:186.
- [17] Buha J, Lumley RN, Crosky AG, Hono K. Acta Mater 2007;55:3015.
- [18] Murayama M, Hono K. Acta Mater 1999;47:1537.
- [19] Esmaili S, Vaumousse D, Zandbergen MW, Poole WJ, Cerezo A, Lloyd DJ. Phil Mag 2007;87:3797.
- [20] Andersen SJ, Zandbergen HW, Jansen JE, Taeholt C, Tundal U, Reiso O. Acta Mater 1998;46:3283.
- [21] Zandbergen HW, Andersen SJ, Jansen J. Science 1997;277:1221.
- [22] Vissers R, van Huis MA, Jansen J, Zandbergen HW, Marioara CD, Andersen SJ. Acta Mater 2007;55:3815.
- [23] Dumolt SD, Laughlin DE, Williams JC. Scr Metall Mater 1984;18:1347.
- [24] van Huis MA, Chen JH, Zandbergen HW, Sluiter MHF. Acta Mater 2006;54:2945.
- [25] Ravi C, Wolverton C. Acta Mater 2004;52:4213.
- [26] Pogatscher S, Antrekowitsch H, Leitner H, Pöschmann D, Zhang Z, Uggowitzer PJ. Acta Mater 2012; Accepted, doi: 10.1016/j.actamat.2012.04.026
- [27] Ji YL, Zhong H, Hu P, Guo FA. Materials & Design 2011;32:2974.
- [28] Røset J, Tundal U, Reiso O. Mater Forum 2004;28:300.

- [29] Bale CW, Chartrand P, Degterov SA, Eriksson G, Hack K, Ben Mahfoud R *et al.* Calphad 2002;26:189.
- [30] Shercliff HR, Ashby MF. Acta Metall Mater 1990;38:1789.
- [31] Esmaeili S, Lloyd DJ, Poole WJ. Acta Mater 2003;51:3467.
- [32] Esmaeili S, Lloyd DJ, Poole WJ. Acta Mater 2003;51:2243.
- [33] Pogatscher S, Antrekowitsch H, Ebner T, Uggowitzer PJ. In Suarez EC, editor. TMS Light Metals. Orlando. TMS; 2012. p. 415.
- [34] Pogatscher S, Antrekowitsch H, Leitner H, Sologubenko AS, Uggowitzer PJ. Scr Mater 2012; To be published
- [35] Porter DA, Easterling KE. Phase Transformations in Metals and Alloys. London Weinheim New York Tokyo Melbourne Madras: Chapman & Hall; 1992.
- [36] Christian JW. The Theory of Transformations in Metals and Alloys. Oxford: Pergamon; 2002.
- [37] Fischer FD, Svoboda J, Appel F, Kozeschnik E. Acta Mater 2011;59:3463.

7 SUMMARY & OUTLOOK

7.1 Summary

Al-Mg-Si alloys are the most frequently used group of age hardenable aluminum alloys. The effect of natural pre-aging on the artificial aging, a problem of significant academic as well as industrial interest, has not been fully resolved since it was discovered in 1939. In this thesis a new concept for understanding this effect was developed.

Microstructural observations using atom probe tomography and electrical resistivity measurements combined with an analysis of the temperature dependence of precipitation kinetics and dissolution processes revealed an unexpected influence of the artificial aging temperature on the effect of natural pre-aging. A change from a negative to a positive influence of natural pre-aging on subsequent artificial aging depending on the aging temperature was observed in rich Al-Mg-Si alloys. This was a key result of the work and strongly pushed the further research. It was interpreted taking into account the effect of vacancy mobility on precipitation reactions. By introducing the “vacancy-prison mechanism” which addresses Mg,Si co-cluster vacancy interactions during artificial aging, it was possible to explain the found unexpected dependence on temperature for the first time. Moreover, the above mentioned mechanism provided the basis for the new concept for understanding the effect of natural pre-aging developed in this thesis. The model assumes that vacancies are trapped in Mg,Si-co-clusters during natural pre-aging due to solute-vacancy interactions. Accordingly, the mobility of these imprisoned quenched-in vacancies highly depends on the behavior of Mg,Si co-clusters during artificial aging. Due to their slow dissolution kinetics, Mg,Si co-clusters are able to act as relatively stable vacancy prisons at common artificial aging temperatures. A rise in temperature produces faster dissolution, associated with a release of vacancies, which was observed to significantly influence precipitation reactions. In short, vacancy-rich Mg,Si co-clusters serve as vacancy prisons during artificial aging. The clusters exhibit a temperature dependent release behavior, which results in slow precipitation kinetics at industrial common temperatures but enhanced kinetics at high temperatures.

In order to clarify the applicability of the vacancy-prison concept, the T6 microstructure of AA6061, the alloy most intensively studied in the scope of this work, was examined in detail. A comparative approach of atom probe tomography and transmission electron microscopy was applied to gain detailed insight into its chemical composition and uncover structural issues. It was found that the β'' phase in AA6061, formed by direct artificial aging and artificial aging after natural pre-aging, contains a significant amount of Al and shows a Mg/Si ratio higher than expected from the famous Mg_5Si_6 stoichiometry. However, the size distribution of the β'' phase was observed to be totally different for both thermal histories and its genesis could be successfully explained by the “vacancy-prison mechanism.”

To shed more light on the complex role of vacancies during artificial aging, the relationship between quenched-in vacancies and the nucleation of the β'' phase was studied via a multi-method approach including atom probe tomography, transmission electron microscopy, electrical resistivity and hardness measurements, and differential scanning calorimetry. Quenched-in vacancies were shown to be of particular importance for the nucleation of the β'' phase and its directly transformable precursors. In the case of direct artificial aging, they were found to strongly assist their nucleation. For artificial aging after natural pre-aging the nucleation of β'' was observed to be hindered. This was explained by a low concentration of quenched-in vacancies derived from the “vacancy-prison mechanism.” In addition, it was shown that interrupted quenching is an appropriate heat treatment strategy to activate the nucleation of β'' . It allows the formation of a dense distribution of stable nuclei of β'' prior to natural pre-aging. The developed procedure is able to reduce the negative effect of natural pre-aging on the artificial aging in rich Al-Mg-Si to zero without requiring an additional pre-aging treatment.

Furthermore, the fundamental differences in the effect of natural pre-aging on the artificial aging in rich and lean Al-Mg-Si alloys were addressed. Dissolution kinetics of Mg₂Si co-clusters during artificial aging was studied in a wide temperature range for both types of alloys. By means of theoretical considerations concerning the annihilation kinetics of quenched-in vacancies during artificial aging, it was possible to extend the vacancy-prison model to the lean alloy AA6060. A comparison of the temperature dependency of artificial aging with and without natural pre-aging for both alloys, rich AA6061 and lean AA6060, showed that quenched-in vacancies in lean Al-Mg-Si alloys are far less important for the nucleation of β'' during artificial aging than in rich Al-Mg-Si alloys, because they are supposed to anneal out before the critical size of β'' nuclei can be reached.

The fact that from an industrial point of view natural pre-aging is much more significant for AA6061 was accounted for by an interdependence study of the solute super-saturation and the effects of natural pre-aging on the artificial aging within the compositional limits of this alloy. The influence of a compositional variation of a range of alloying elements including Al, Fe, Cr, Zn, Ti, Mg, Si and Cu was studied using thermodynamic calculations and an analysis of yield strength data for several model alloys. As generally expected, precipitation kinetics was found to strongly depend on the solute super-saturation in the case of direct artificial aging. Small variations in the total chemical composition, including elements not directly related to precipitation hardening such as Fe and Ti, were shown to cause noticeable differences in artificial aging kinetics when novel direct aging methods are applied. For artificial aging after natural pre-aging the kinetics showed almost no dependence on the solute super-saturation. This was found to be an exception from simple precipitation kinetics and could be satisfactorily

explained based on the “vacancy-prison mechanism” also considering annihilation kinetics of quenched-in vacancies during artificial aging.

In general, the presented concepts for understanding the effect of natural pre-aging on the artificial aging of Al-Mg-Si alloys describe the observed phenomenon well in a wide temperature and compositional range. It is believed that this will significantly contribute to solving many industrial issues concerning the effect of natural pre-aging on the artificial aging in Al-Mg-Si alloys.

7.2 Outlook

The new concepts for understanding the effect of natural pre-aging on the artificial aging of Al-Mg-Si alloys will enable AMAG rolling to take process-related measures, such as optimum design of new heat treatment strategies and alloy-related measures to control the effect of natural pre-aging in a significantly more systematic and specific manner than before. Apart from that, the desired depth of understanding concerning the role of quenched-in vacancies during artificial aging of Al-Mg-Si alloys is essential for successful computer-aided modeling of precipitation processes predicting the precipitation microstructure and the resulting materials properties in the future.

In the following section, two innovations already accomplished in the scope of the thesis in parts and which will hopefully be of great advantage for AMAG rolling in the near future are outlined. Due to a nondisclosure agreement, the following remarks are only schematic but give a good description of what can be an applicable benefit from the fundamental investigations performed within this thesis.

The first example is based on the new heat treatment strategies presented in chapter 4. Interrupted quenching as an isothermal process step was shown to be able to avoid the negative effect of natural pre-aging on the artificial aging in rich Al-Mg-Si alloys without requiring an additional pre-aging treatment. As an isothermal interruption of the quenching procedure cannot be performed in the industrial production of Al-Mg-Si plates, a continuous version of interrupted quenching was developed for the alloys AA6061 and AA6082. To determine the processing parameters of such a heat treatment strategy, a study of industrial processing conditions was performed in the laboratory. For optimal design of experiments and detection of major process parameters determining the tensile properties, the MODDE™ 7.0 software was used. A multi-linear regression obtained by a partial least squares algorithm was applied to search for the optimal processing parameters. As an example of this approach, figure 7.1 schematically shows contour plots of the yield strength for the alloys AA6082 and AA6061

in T651 condition. The dependence of the yield strength on the starting temperature of continuous interrupted quenching and the thickness of the quenched Al-Mg-Si plates is depicted.

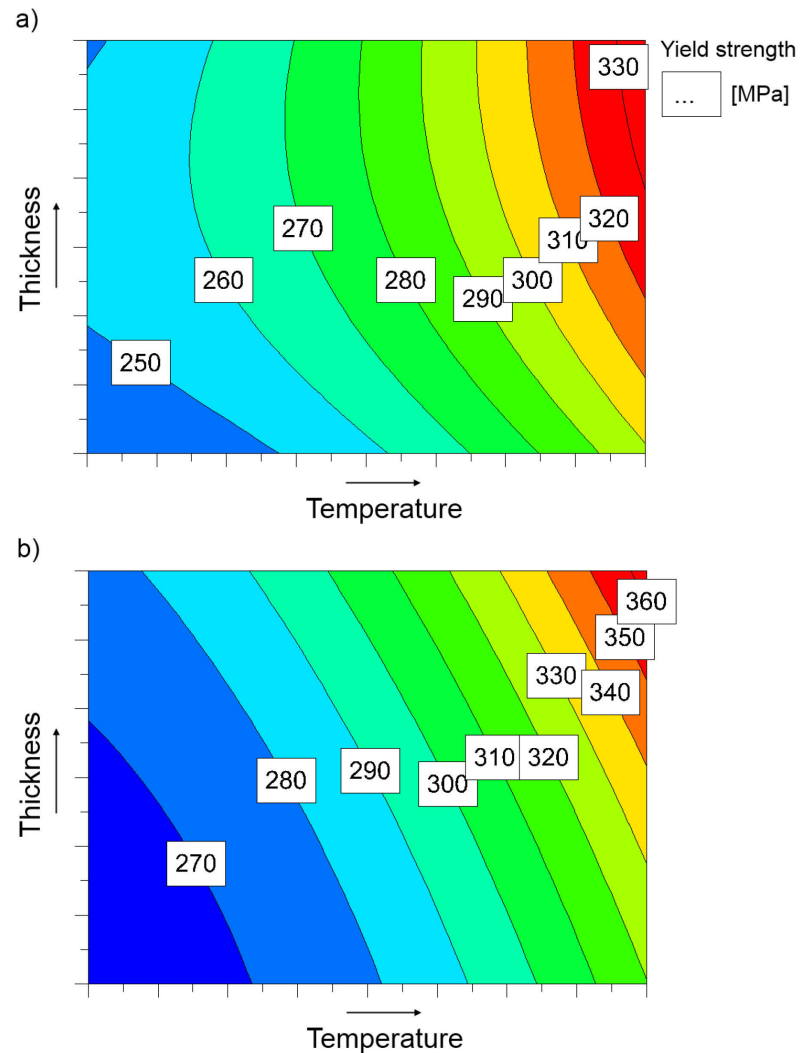


Figure 7.1: Influence of the starting temperature of continuous interrupted quenching and thickness of the quenched Al-Mg-Si plates on the yield strength in T651 condition for the alloys (a) AA6061 and (b) AA6082 (schematically)

A huge potential for innovation was found by simply adjusting the industrial quenching procedure. A reduction of the duration of artificial aging of more than 50 % can be easily reached in a large parameter space for both types of Al-Mg-Si alloys. Besides this, the new heat treatment strategy allows an increase in the yield strength of Al-Mg-Si alloys in T651 condition up to 40 %. The procedure was already allocated to industrial scale in a first trial series. However, an industrial production incorporating continuous interrupted quenching requires a deep knowledge of the technology of quenching. Hence, an intensive experimental study of the heat transfer in water spraying based quenching systems was additionally performed within this

project and will hopefully facilitate the integration of interrupted quenching in the production of Al-Mg-Si alloys soon.

The second example is based on a consequence of the “vacancy-prison mechanism.” Interactions of trace elements and quenched-in vacancies are believed to influence the effect of natural pre-aging in Al-Mg-Si alloys. It is supposed that trace elements exhibiting a strong attractive interaction and a sufficient solubility in Al-Mg-Si alloys are able to prohibit the formation of Mg₂Si co-clusters during natural pre-aging, which act as vacancy prisons during artificial aging. Instead, aggregates of these additive element and vacancies (e.g. solute-vacancy pairs) highly immobile at room temperature are expected to form during natural pre-aging. If such configuration can be provided to be thermally instable enough at artificial aging temperature, a quenched-in assisted nucleation of the β'' phase can be reached. As this was shown to be the key to fast artificial aging kinetics, a “vacancy active” trace element could possibly solve the problem of natural pre-aging. Based on literature data, several trace elements were chosen for experimental studies in laboratory scale. The effect of trace additions of Li, Ca, Sr, Ba, Ag, Cd, In, Ge, Sn, Pb, Sb, and Bi on the aging behavior of the Al-Mg-Si alloy AA6061 was already extensively investigated in a diploma thesis supervised within the scope of this work. Three of these elements were found to obey the previously mentioned criteria. As an example of the effect, figure 7.2 shows the influence of the addition of a “vacancy active” trace element on natural aging and artificial aging in the alloy AA6061. A suppression of natural aging can clearly be seen in figure 7.2a. The expected improvement of artificial aging at common artificial aging temperatures is shown in figure 7.2b. Interestingly, artificial aging can also be performed at unconventionally high temperatures without losing much in hardness, but accounting on extremely accelerating kinetics (figure 7.2c). This effect is believed to be linked to the influence of trace elements on annihilation kinetics of quenched-in vacancies. However, a clarification of the fundamentals behind the effects of “vacancy active” trace elements needs detailed experimental as well as theoretical work in the future.

The discovered influence of trace elements is of significant interest for application. Due to a suppression of natural aging after quenching, forming operations can be performed much easier in between quenching and artificial aging. As the artificial aging behavior is also strongly improved, it is a promising strategy to take great advantage in processing Al-Mg-Si sheets for automotive outer panel applications. A significantly reduced duration of artificial aging might also be a strong advantage in the production of other semi-finished products such as Al-Mg-Si plates.

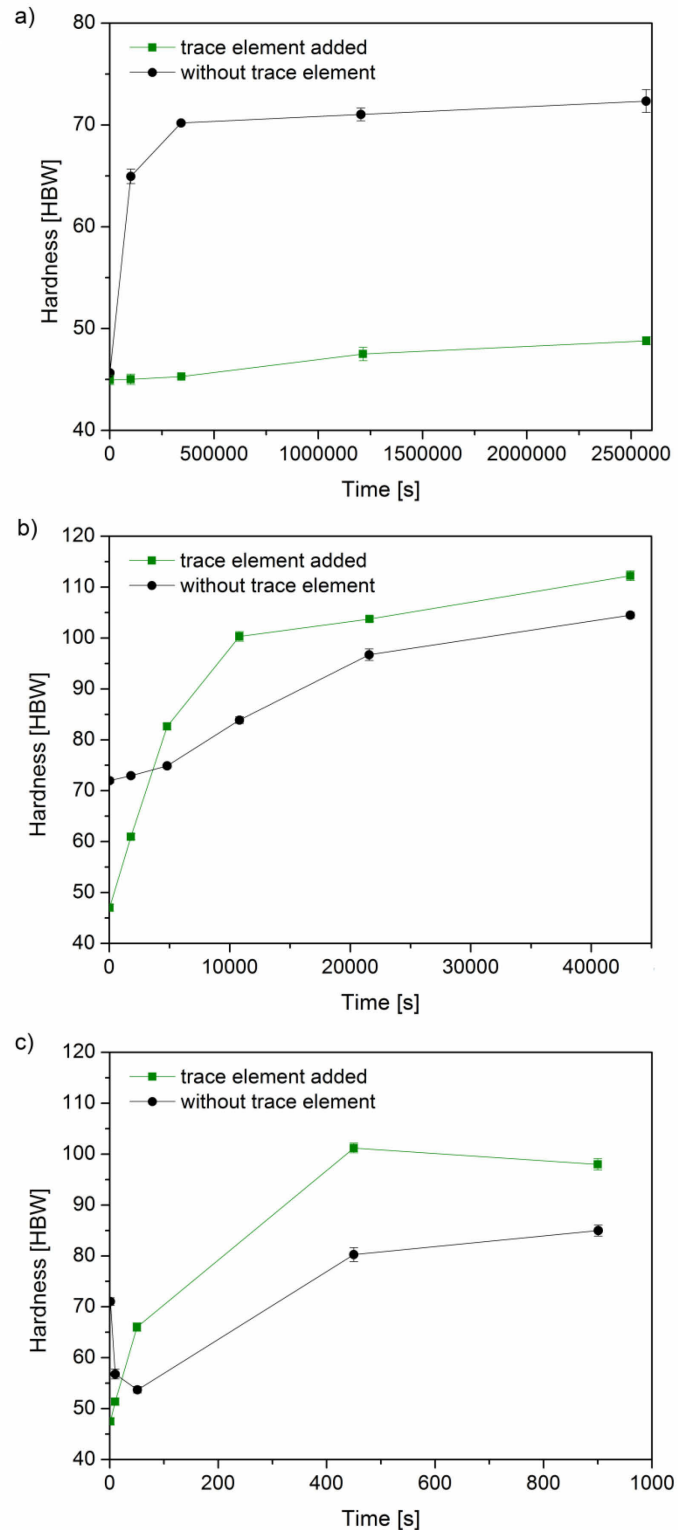


Figure 7.2: Hardness evolution during (a) natural and artificial aging ((b) 170 °, (c) 250 °C) of the alloy AA6061 with and without the addition of a “vacancy-active” trace element

To capitalize on these great advantages, AMAG rolling GmbH has already filed a patent (*Aushärtbare Aluminiumlegierung sowie Verfahren zur Verbesserung der Warmaushärtungsfähigkeit*; EP 121 566 23.6) at the European Patent Office which applies the above-described principles.

APPENDIX

CURRICULUM VITAE

Stefan Pogatscher

Unterkurzheim 20, 8793 Gai, Austria

Telephone: 00436644256275 / E-mail: stefan.pogatscher@unileoben.ac.at

Professional Career

Since 2008 Junior researcher position at the Chair of Nonferrous Metallurgy, Montanuniversitaet Leoben, Austria

Education

Since 2009 PhD student at the Chair of Nonferrous Metallurgy, Montanuniversitaet Leoben; Several research stays at the Laboratory of Metal Physics and Technology, ETH Zurich, Switzerland

2007 – 2008 Graduate program: Metallurgy at the Montanuniversitaet Leoben focused on Nonferrous Metallurgy, Ferrous and steel metallurgy and Foundry technology (MSc)

2003 – 2007 Undergraduate program: Metallurgy at the Montanuniversitaet Leoben (BSc)

2002 – 2003 Military service

1997 – 2002 Higher Technical College for Metallurgy in Leoben

Awards and Honors

2009 ASMET-Award for the Best Diploma Thesis in Metallurgy 2008, Austrian Society for Metallurgy and Materials, Austria

2008 Rektor-Platzer-Ring, Montanuniversitaet Leoben, Austria

2008 Graduation with honors: Graduate program Metallurgy at the Montanuniversitaet Leoben

2007 Graduation with honors: Undergraduate program: Metallurgy at the Montanuniversitaet Leoben

2002 Graduation with honors: School leaving examination at the Higher Technical College for Metallurgy in Leoben

Supervision of students

Hädicke P.: Influence of ultrasonic on the precipitation characteristics of AlMgSi(Cu)-alloys. Bachelor thesis (2010).

Hädicke P.: Effect of various alloying elements on the precipitation behavior of AlMgSi-alloys. Bachelor thesis (2010).

Körbler N., Sagadin C.: Precision measurements of the specific electrical resistivity of aluminum alloys at low temperatures. Bachelor thesis (2012).

Reinhart P.M.: Solder alloys and process limitations for tin coating of copper flat wires. Master thesis (2010).

Werinos M.: Influence of microalloying elements on the precipitation behavior of Al-Mg-Si alloys. Master thesis (2010).

Publication List

Peer Reviewed Papers

Pogatscher S., H. Antrekowitsch, H. Leitner, T. Ebner and P.J. Uggowitzer: Mechanisms controlling the artificial aging of Al-Mg-Si Alloys. *Acta Materialia* 59 (2011), 3352-3363.

Pogatscher S., H. Antrekowitsch, H. Leitner, D. Pöschmann, Z. Zhang and P.J. Uggowitzer: Influence of interrupted quenching on artificial aging of Al-Mg-Si alloys. doi: 10.1016/j.actamat.2012.04.026 (2012).

Pogatscher S., H. Antrekowitsch and P.J. Uggowitzer: Interdependent Effect of chemical composition and thermal history on artificial aging of AA6061. Submitted to *Acta Materialia* (2012).

Pogatscher S., H. Antrekowitsch, H. Leitner, A.S. Sologubenko, and P.J. Uggowitzer: The two basic T6-microstructures of AA6061. Submitted to *Acta Materialia* (2012).

Other Papers

Antrekowitsch H., S. Koch, H. Paulitsch, S. Pogatscher, P. Pucher, F. Stadler and C. Wagner: Recycling und Werkstoffentwicklung von Aluminium. *BHM* 156 7 (2011), 287-294.

Proceedings

Pogatscher, S., H. Antrekowitsch, T. Ebner, and P.J. Uggowitzer: The role of co-clusters in the artificial aging of AA6061 and AA6060, TMS Light Metals (2012), Orlando, USA, 415-420.

Pogatscher S., S. Koch and H. Antrekowitsch: Development of a coating process for copper strips with appropriate lead-free solders. Proc. of EMC 1 (2011), Düsseldorf, Germany, 123-136.

Messner T., S. Pogatscher, H. Antrekowitsch and J. Pesl: Thermodynamic modelling of the behaviour of accompanying elements in secondary copper production. Proc. of EMC 4 (2007), Düsseldorf, Germany, 1819-1836.

Talks

Pogatscher S.: Einfluss einer unterbrochenen Abschreckung auf die Warmauslagerung von Al-Mg-Si Legierungen. Forum für Metallurgie und Werkstofftechnik, Leoben, Austria (2012).

Pogatscher, S., H. Antrekowitsch, T. Ebner, and P.J. Uggowitzer: The role of co-clusters in the artificial aging of AA6061 and AA6060. TMS. Orlando, USA (2012).

Pogatscher S.: Einfluss einer unterbrochenen Abschreckung auf die Warmauslagerung von Al-Mg-Si Legierungen. ASMET Fachausschuss für Leichtmetalle, Ranshofen, Austria (2011).

Pogatscher S.: Influence of direct pre-aging on artificial aging of Al-Mg-Si alloys. European Conference on Aluminium Alloys (ECAA). Bremen, Germany (2011).

Pogatscher S.: Influence of interrupted quenching on artificial aging of Al-Mg-Si alloys. Aluminum Modeling Group Workshop, Wien, Austria (2011).

Pogatscher S.: Development of a coating process for copper strips with appropriate lead-free solders. EMC, Düsseldorf, Germany (2011).

Pogatscher S.: Mechanisms controlling the artificial aging of Al-Mg-Si alloys. 17th International Symposium on Metastable, Amorphous and Nanostructured Materials – ISMANAM2010, Zürich, Swiss (2010).

Posters

Pogatscher S. and H. Antrekowitsch: Unterbrochenes Abschrecken (I.Q.) von Al-Mg-Si-Legierungen. Forum für Metallurgie und Werkstofftechnik, Leoben, Austria (2012).

Pogatscher S. and H. Antrekowitsch: Aushärtung in 6xxx-Legierungen. WerWasWo.Forschung@MUL, Leoben, Austria (2012).

Pogatscher S. and H. Antrekowitsch: Einfluss der Kaltauslagerung auf die Warmauslagerung von AlMgSi-Legierungen. Forum für Metallurgie und Werkstofftechnik, Leoben, Austria (2011).

Pogatscher S. and H. Antrekowitsch: Effect of prior natural aging on artificial aging of Al-Mg-Si-alloys. EMC, Düsseldorf, Germany (2011).

Pogatscher S. and H. Antrekowitsch: Untersuchung des Aushärtungsverhaltens von AlMgSi-Legierungen. Forum für Metallurgie und Werkstofftechnik, Leoben, Austria (2010).

Pogatscher S. and S. Koch: Surface coating of copper strips with lead free solder alloys. EMC, Innsbruck, Austria (2009).

Pogatscher S.: Oberflächenbeschichtung von Kupfer-Flachdrähten mit bleifreien Lotlegierungen. Forum für Metallurgie und Werkstofftechnik, Leoben, Austria (2009).

Pogatscher S. and H. Antrekowitsch: Oberflächenbeschichtung von Cu-Flachdrähten mit bleifreien Loten. WerWasWo.Forschung@MUL, Leoben, Austria (2009).

Pogatscher S. and H. Antrekowitsch: Alternative Wärmebehandlungen von 6xxx-Aluminiumlegierungen. WerWasWo.Forschung@MUL, Leoben, Austria (2009).

Patents

AMAG Austria Metall AG: Aushärtbare Aluminiumlegierung sowie Verfahren zur Verbesserung der Warmaushärtungsfähigkeit, EP 121 566 23.6, filed to the European Patent Office (2012).